The Nature of Jets in Powerful Radio Galaxies

Author:

Emmanuel Bempong-Manful

Supervised by:

Prof. Martin Hardcastle

Centre for Astrophysics Research

School of Physics, Astronomy and Mathematics

University of Hertfordshire

Submitted to the University of Hertfordshire in partial fulfilment of the requirements of the degree of Master of Science by Research.

October, 2017

Abstract

Relativistic plasma ejected from SMBHs at the centres of galaxies is known to play a key role in the AGN feedback cycle, and consequently the formation and evolution of structure in the universe. However, the physics driving the observed jet structure in these cosmic outflows remains an open question. As part of a project that aims to resolve some of these key questions in extragalactic jet physics, this thesis presents high resolution and sensitivity studies on the nature of jets in two known powerful FR I radio galaxies (3C465 & 3C83.1B), using the first ever *deep transverse resolved radio observations* of these objects from e-MERLIN, and with complementary observations from the EVLA.

Our radio images represent the highest resolution and sensitivity maps of 3C465 to date, and compared with previous observations, our highest resolution (e-MERLIN only) map shows that there exist multiple bright knotty structures at the base of the NW jet in 3C465. A detailed description of the overall radio structure is presented.

We measure sidedness ratio of 14.85, and consequently derive lower and upper limit values of 0.5*c* and 61^{o} respectively for the jet velocity, β_j and angle to the line of sight, θ in 3C465. We also use matched-resolution images across two frequencies (~1.5 and ~8.5 GHz) to construct accurate, spatially resolved spectral index image of the radio source and consequently derive the characteristic spectra across the entire radio galaxy (jet, hotspots and plumes). Our results shows that the jet spectra are fairly constant ($<\alpha_{jet}>$ = -0.7), and the observed spectral flattening within the first 4.42 kpc radius from the core coincides with the region hosting the bright knots, and is consistent with the site of X-ray particle acceleration observed at the base of the radio jet in previous studies.

There is very little dispersion ($<\Delta\alpha>$ = -0.04) between the spectra of the two hotspot components, plausibly indicating that electron populations of the same ages are injected at

these sites. Our spectral profiles suggest that the NW and SE plumes in 3C465 are approximately homologous structures, in spite of the striking asymmetry in their physical size and shape. We attribute this asymmetry in morphology to 2-D projection effects, while variations in mass injection and propagation in external pressure and density gradients in the two regions account for the comparatively steeper spectrum in the NW plume, $<\alpha_{NWp}> = -1.43$ compared with the SE plume, $<\alpha_{SEp}> = -1.38$.

Overall, our results show that first-order Fermi process at mildly relativistic shocks is the most likely acceleration mechanism at play in the radio source 3C465; and consistent with previous works, we conclude that two plausible acceleration mechanisms; (a) when bulk flow speeds, $\beta_j \geq 0.5$, and (b) when flow speeds, β_j are less than ≈ 0.5 exist in our radio sample. Whereas the first case can accelerate electrons to high Lorentz factors, the second scenario dominates at slower speeds and larger distances.

As extension of this work, we aim to undertake a detailed study of the radio source 3C83.1B and statistically compare the synchrotron spectra in the two samples, in order to check for any discrepancy. We also note for further study, the so called *deviations from power law spectra* which are indicators of synchrotron ageing and plausible diagnostics of the acceleration mechanism in order to place greater constraints on the nature of jet-particle acceleration in these sources; and in addition, polarization studies to investigate the orientation and degree of ordering of magnetic field in driving the evolution of the radio jets in these powerful FR I sources.

Declaration

I declare that no part of this work is being submitted concurrently for another award of the University or any other awarding body or institution. This thesis contains a substantial body of work that has not previously been submitted successfully for an award of the University or any other awarding body or institution.

Except where indicated otherwise in the submission, the submission is my own work and has not previously been submitted successfully for any award. The research was carried out under the supervision of Prof. Martin Hardcastle at the Centre for Astrophysics Research, University of Hertfordshire.

Acknowledgements

This research was undertaken with a studentship through the Development in Africa with Radio Astronomy (DARA) project funded by the UK's Newton Fund.

First, many thanks to my supervisor, Prof. Martin Hardcastle without whose valuable input this research would not have reached a conclusion. It has been a wonderful experience working under your supervision, and I have enjoyed our regular discussions on the research over the past year. Thank you for assisting me with this inspiring work.

My sincere thank you also to Dr. Javier Moldon (e-MERLIN Project Scientist) for taking time to guide me through VLBI (e-MERLIN) data reduction with AIPS at the Jodrell Bank Centre for Astrophysics, University of Manchester.

I have also benefited from the great working environment at the Centre for Astrophysics Research, University of Hertfordshire and I want to say thank you to all the staff and postgraduate students working there. Most importantly, I want to thank Dr. Wendy Williams, Vijay Mahatma, Jonathan Westcott and Garreth Martin for their assistance whenever I have had to call on them. Thanks once again to Jonathan and his house mates (Chris, Julie, and Emma) for hosting me at their residence during the last few weeks of this research – this was invaluable in completing this thesis and I'm very grateful.

Finally, I thank my family for their love and support during my studies.

Table of Contents

Contents

List of Figures

List of Tables

CHAPTER 1

Introduction

1.1 Background

The study of celestial objects at radio wavelengths dates back to the early decades of the 20th century, notably with the discovery of some radio signals from very distant objects by Karl Jansky – the results of which was published in his famous 1930s paper *"Electrical Disturbances Apparently of Extraterrestrial Origin"* (Jansky, 1933). Subsequently, radio observations have evolved into an unrivalled means of probing the frontiers of both the local and distant universe and today, serve as an exceptional tool in resolving many of the mysteries of the cosmos, from the physics of star births to the formation and evolution of massive galaxies and large scale structures over cosmic time.

Since the first observation of astrophysical jets by Curtis (1918), countless jets of high-energy particles have been observed and studied across a broad spectrum of cosmological scales with radio synthesis maps of hundreds of AGNs in the last few decades revealing jets, in the ranges of sub-parsec to mega-parsec scales (e.g., Ghisellini et al. 1993). In addition to energy, momentum and mass transport from the host galaxy, these cosmic outflows serve as diagnostic parameters for probing the role of highly energetic processes in the formation and evolution of large scale structure in the universe.

The jets in powerful radio galaxies are thought to be highly relativistic outflows consisting mostly of electron-positron plasma (e.g., Wardle et al. 1998; Kundt, 2014). However, our in-depth understanding of these jets, including what we are actually seeing in radio emission – whether or not this comes from the whole jet or just a small region, the nature of jet particle acceleration, and the role of magnetic fields among others – is very incomplete. Against this backdrop, our aim in the present study will involve construction of the highest resolution and

sensitivity (total intensity, polarization and spectra index) maps to date, for two known powerful jet sources, and thus attempt to resolve the physics driving the observed jet structure.

1.1.1 Outline of the Thesis

This research dissertation will comprise five chapters.

Chapter 1: This is the current chapter, and here I provide a background and introduction to the present study. Key highlights of the chapter will include; AGNs (with focus on radio AGNs) and how their nuclear activity drives feedback, structure formation and black hole growth. I also provide an overview of astrophysical jets with emphasis on extragalactic relativistic jets and discuss the FR I and FR II jet dichotomy. The philosophy of radio interferometry and synthesis imaging with a brief overview of the interferometry elements employed in the present study is also presented. Finally, I discuss the scientific rationale for undertaking the current study and offer an insight into the value of e-MERLIN observations in resolving the physics of extragalactic jets on sub-kpc scales.

Chapter 2: In chapter two, I present the radio observations and data from the two interferometry elements employed in the present study. I also provide a comprehensive description of the methodology – data calibration and imaging techniques implemented in the current research, with a key emphasis on array combination of the two interferometry elements, and how this allowed us to reconstruct our science targets at the highest resolution and sensitivity to date.

Chapter 3 & 4: Chapters three and four are *"science chapters"* and highlights the key results from our analysis in the present study. First, we present total intensity maps of our science targets obtained from the calibration and imaging process and provide physical interpretations of these maps. Through combination and/or comparison of our results with previous works – i.e., from radio through to X-rays, we resolve to a high degree of precision the physics of where and how particles are accelerated in the jets, hotspots and plumes of these powerful radio

sources. We also estimate the jet velocities, mass fluxes, and entrainment rates for our science targets and as well discuss how these low-luminosity jets decelerate from relativistic to sub-relativistic speeds on kpc scales. Most of this is done for 3C465 only in the present work.

Chapter 5: Finally, in chapter five I bring it altogether by drawing relevant conclusions from the main results obtained in the present study in relation to our research objectives. Also, I present prospects for future studies which due to time and/or other constraints were not covered in the present study.

1.2 The Active Galactic Nuclei (AGNs)

Active Galactic Nuclei (AGNs) are bright compact regions at the centres of a relatively small minority (~ 10% - 15%) of galaxies (e.g. Ho, Filippenko & Sargent, 1997), driven by the accretion of infalling material onto the galactic-centre supermassive black hole (central engine). Originally discovered by Carl Seyfert in the 1940s, the physics and environments of these peculiar class of galaxies have progressively become a subject of interest in the field of astrophysical research and are among the most studied entities of the cosmos today. The distinctive characteristic of this group of galaxies as observed by Seyfert in the optical band was their characteristic bright, semi-stellar nucleus and broad emission lines with speeds up to 8500 km/s (Seyfert, 1943). Compelling as the discovery was, the rather poor angular resolution of telescopes at the time made characterization of these objects a daunting task. However, thanks to advances in astronomical instrumentation in the years leading up to the present decade, composite observational evidence particularly at radio frequencies has considerably opened up the hidden universe and allowed for a more comprehensive mapping of these celestial objects at extreme spatial resolutions (e.g., Grupe, 2004). This has greatly broadened our understanding of these extraordinary cosmic species – from the then moderate conclusion drawn that, radio-loud quasars for example were simply strong radio emitting galactic stars (e.g., Schmidt 1963) to rather more complex conclusions today which suggest that these AGNs

are powered by the conversion of gravitational energy (of accreted material) into mechanical and electromagnetic energy inside their central engine (e.g., Silk & Rees, 1998; Krolik, 1999). Today, it is a well-known fact that all massive galaxies contain massive BHs at their centre – the activities of which account for the observational characteristics of the host galaxy. These unusual activities within their nuclei coupled with the intense conditions characterizing their environment, earmark them as key laboratories for exploring the frontiers of high energy astrophysical processes in the universe. Figure 1 below shows the basic building blocks of AGNs; although for many radio AGNs (e.g., 3C465 and 3C83.1B), these features are not immediately obvious.

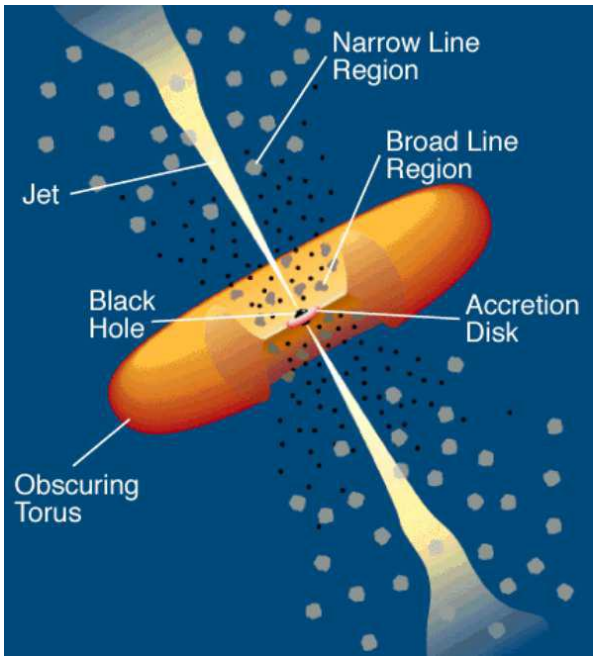

Figure 1: A schematic diagram showing the main constituents of the current most favoured model of an AGN (Adapted from Urry & Padovani, 1995).

The gravitational potential energy of the supermassive black hole at the centre is the ultimate source of the AGN luminosity and it is surrounded by an accretion disk which occupies the centre of a geometrically thin and optically thick dusty torus. Revolving clouds of gas at different distances from the nucleus, produce two distinct emission-line regions: (a) the broad-line region (BLR) which predominantly resides under the black hole's gravitational influence

and (b) the narrow-line regions (NLR) which spreads over much larger scales. These emission lines according to Popovic (2002) are both produced under a broad range of physical and kinematical conditions and serve as powerful diagnostic parameters for emitting gas in the different emitting regions of AGNs. Finally, twin radio jets of relativistic particles (which are the objects of interest in the present study) can also be seen launched from close to the accretion disk in opposite directions. It is worthwhile to mention here that several efforts have been made in the recent past on both the observational (e.g., Perez et al. 2000; Marquez et al. 2004) and theoretical (e.g., Gutcke et al. 2015) front to elucidate our understanding of these unusual activities associated with the central engine – which serves as fuelling mechanism that powers the AGN in order to constrain the morphology and large scale kinematics of these group of galaxies.

Table 1: Statistical comparison of the components of a standard AGN model

	Black Hole	*Accretion Disk*	*Emission Lines*		*Torus*
			BLR	*NLR*	
r (pc)	10^{-6} - 10^{-5}	~10^{-3}	~0.01 - 0.1	~100 - 1000	~1 - 100
n_e *(cm^{-3})*	–	~10^{15}	~10^{10}	~10^{3} - 10^{6}	~10^{3} - 10^{6}
v (kms^{-1})	~*c*	~0.3*c*	~few ×10^{3}	~few ×100	~50 - 100

Notes: Demographics of the main constituents of an active galactic nuclei showing their respective sizes, *r*; number density, n_e; and gas velocity of FWHM, *v* (Adapted from; Bianchi, Maiolino & Risaliti, 2012 and references therein).

1.2.1 Towards a Unification Theory: The AGN paradigm

As illustrated in Figure 1 above, the whole AGN paradigm consists of a central supermassive black hole (e.g., Peterson, 2014), whose gravitational potential energy is the ultimate source of the AGN luminosity; a circumnuclear accretion disk (e.g., Narayan & Yi, 1994), that provides the means for converting gravitational potential energy into radiation; optically-thick emission line clouds (e.g., Cackett & Horne, 2006) ; an obscuring torus (e.g., Tadhunter 2008), that obstructs the continuum and broad-line emission in some directions; and in some cases bipolar

outflows of relativistic plasma which powers massive radio sources. However, an intriguing challenge resulting from this paradigm is the fact that different AGN types arises depending on the viewing angle of an observer – i.e. strongly orientation dependent. This prompted researchers to hypothesize that perhaps some different physical conditions might be at play and ultimately led to the concept of constructing a standard model to describe the structure of these cosmic species. Notwithstanding the complexity of host galaxy morphology, environments, and cosmic evolution among others (see; Urry & Padovani, 1995), several attempts have been made in the past to unify AGNs (e.g., Antonucci 1993; Urry & Padovani, 1995; Falcke, Kording & Markoff, 2004). For in-depth discussions and review on the subject, the reader is referred to the seminal work of Urry & Padovani (1995) whose effort to unify AGNs about two decades ago has to date proven to be robust and most favoured unified scheme – except that it does not work for most radio galaxies.

Characterisation of AGNs are commonly based on their optical spectra and radio-loudness into; Type 1 – those with bright continua and broad emission lines; and Type 2 – those with weak continua and narrow emission lines. However, the evidence of two forms of strongly anisotropic radiation patterns from radio-loud AGN – (1) obscuration by optically thick matter and (2) relativistic beaming of radio emission primarily stimulates the different classes of AGN unification schemes (Urry, Padovani & Stickel, 1991). Substantial evidence which has motivated unification schemes have predominantly originated from:

i. **Apparent Hidden Emission Lines** – in which some Seyfert 2s have been observed to show broad emission lines in polarized light due to scattering of photons by hot electrons near the central engine and thereby appearing as Seyfert 1s (e.g., Capetti et al. 1995). Conversely, some narrow line radio galaxies (NLRG) have been observed to have hidden broad lines (e.g., Goodrich, 2001).

ii. **Statistical Tests** – where all Seyfert galaxies have been shown to have narrow line regions with very similar properties (e.g., Cohen 1993). Indeed Lawrence (1987) found the continuum of Seyfert 1s to be stronger compared to their Seyfert 2 counterparts, however, it was not until a decade later that HST observations revealed that the size of Seyfert 1 continuum emitting regions was smaller than those of Seyfert 2s (e.g., Nelson et al. 1996).

Additional evidence for unified schemes has also come from host galaxy properties, environment, and number counts (e.g., Lin et al. 2010).

The explanation by Miller & Antonucci (1983) of the observed weak polarized broad emission lines which was unexpectedly hidden by strong narrow lines in the Seyfert 2 nucleus of NGC 1068 set the foundations for current unified models. Although at present an inexact construction of AGN unified schemes exist, a great deal of the underlying physics driving these schemes is still work in progress due to the observed strongly anisotropic radiation patterns. With the exception of the presence or absence of a jet, the current most favoured AGN unified models lean towards classification schemes which are largely dependent on the orientation of the dusty torus and the luminosity of the nucleus and can be grouped as:

• **Type 1** – Nucleus can be seen face on. Broad and narrow emission lines originating in a high density medium ($n_e \geq 10^9$ cm^{-3}) and low density medium ($n_e \approx 10^3$ - 10^6 cm^{-3}) respectively. Strong continuum emission spectra.

• **Type 2** – Nucleus can be seen edge-on. Narrow emission lines due to obscuration of broad lines by dusty torus. Medium is compton thick suppressing x-rays (e.g., Bassani et al. 1999)

• Intermediate – Observational properties lie between Type 1 and 2. Fractional obscuration of nucleus due to orientation of torus.

The luminosity of the galactic nuclei additionally divides radio AGN population into:

• Seyferts – Galaxies (usually a spiral) with a high surface brightness nucleus that reveals unusual emission-lines (e.g., Seyfert 1943, Kraemer & Crenshaw 2000).

• Quasi Stellar Objects (QSOs) – Extremely luminous, high redshift sources (e.g., Mortlock et al. 2011). Further classified into radio-loud and radio-quiet objects.

Despite notable progress in constructing these relatively simple classification schemes, a number of significant problems exist (see; Urry, Padovani & Stickel, 1991; Urry & Padovani, 1995). In particular, the complexity of AGN systems allow researchers to further speculate the potential existence of fundamentally different objects altogether. The work of Bianchi et al. (2012) in which some objects identified as Type 2 were found to miss broad line regions; and Panessa & Bassani (2002) who also found no clear evidence for the presence of a dusty disk in a number of low power sources, among others are basis for such speculations and may eventually turn out to be true with more sophisticated astronomical instrumentations on the horizon. Table 2 below shows the taxonomy of AGNs as posited by current most favoured models.

Table 2: The AGN Taxonomy

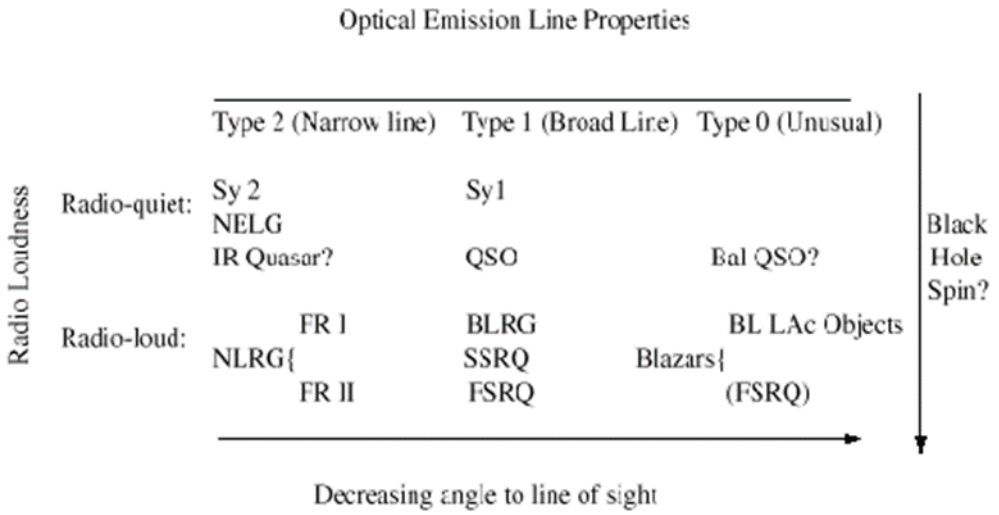

Notes: An empirical division of AGN according to their observed radio and optical/ultraviolet properties. All AGN-type are the same with the observed differences due to angle of line of sight of the observer. It is important to note here that this proposition dates back to, at least, Rowan-Robinson (1977), and became famous in the mid-80s with subsequent reviews by Lawrence (1987); Antonucci (1993); Urry & Padovani (1997); Goodrich (2001). (Adapted from Lawrence 1987, 1993).

1.2.2 Radio AGNs: A Morphological Review

The term 'Radio AGNs' primarily refers to bright radio sources whose strong synchrotron emission allows their detection even at high redshifts. Historically, they have been dichotomized into two – (1) the radio-loud (RL) and radio-quiet (RQ) galaxies with differences in radio luminosity (which results in the observed differences in host galaxy properties and environments) as the criterion (e.g., Lin et al. 2010). Radio-quiet AGNs have relatively low luminosity and make up approximately 90% of all active galaxies. They include; radio-quiet quasars, Seyfert galaxies and LINERs (e.g., Mushotzky 1982). The remaining 10% are radio-loud AGNs and these include; radio-loud quasars, BL Lac Objects, Optically Violent Variables (OVV) and the two morphologically distinct types: FR I (core dominated) and FR II (lobe dominated) radio galaxies (Fanaroff & Riley, 1974) which I discuss further in the next section.

In spite of the variances in host galaxy properties and environments, Sanders et al. (1989) reported similar spectral energy distribution at infrared wavelengths for both the radio-quiet and radio-loud AGNs. In a related study, Xu et al. (1999) essentially observed a significant overlap in their emission line luminosities despite separations in their radio luminosities with the work of Cirasiuolo et al. (2003) further confirming some continuity of properties among selected radio AGN samples. Additionally, more recent observations have even revealed compelling evidence that a radio-loud/radio-quiet double AGN system may co-exist (see; Tadhunter et al. 2012) pointing to a rather sharp contrast to earlier conclusions of Kellerman et al. (1989) and Miller et al. (1990) that there is a big gap in radio power between radio-loud and radio-quiet varieties of QSOs. Furthermore in contrast to previously held assertion that radio-quiet objects lie in disk-dominated hosts compared to bulge-dominated hosts for their radio-loud counterparts (e.g., Smith et al. 1986) evidence suggests that luminous radio-quiet quasars may also exist in bulge-dominated hosts (e.g., Taylor et al. 1996; Bahcall et al. 1997). Rather than resolving the complexity of radio AGN classification, these associations of host galaxy properties and environment among the different classes seemingly complicates our quest to classify these objects into unique groups as evident in the unified schemes. In the section to follow, I focus the discussions on a review of the Fanaroff and Riley class of radio galaxies which has indeed proven remarkably robust in our understanding of the morphology of radio loud AGNs over the last four decades.

1.2.3 The Fanaroff and Riley Class I and II Dichotomy

The Fanaroff and Riley types are predominantly a classification scheme based on the degree of correlation between the high and low surface brightness in the lobes of extragalactic radio sources with their radio luminosity. The classification is intrinsically linked to the degree of brightening near either the core (the central region of the galaxy) or at the extended regions

and can be quantitatively defined as a measure of the ratio of the distance between the two brightest spots and the overall size of the radio galaxy image (Fanaroff & Riley, 1974).

Fanaroff-Riley Type I (FR I): Their high brightness regions are associated with the central galaxy and are often observed with double-sided radio jets. Luminosities are typically below $10^{25} WHz^{-1}$ at 1.4 GHz and they show extended structures which interact with the external environment at large distances (~ kpc scales) from the galactic centre. Wide and narrow angle tail radio galaxies are within this class.

Fanaroff-Riley Type II (FR II): They are edge-brightened with often one-sided highly collimated radio jets which terminate in large radio lobes with visible hot spots. Luminosities are typically above $10^{25} WHz^{-1}$ at 1.4 GHz. They include classical doubles – "powerful" radio sources with huge lobed jets extending hundreds of kpc into the intergalactic medium.

Although Urry & Padovani (1995) argue that construction of a physical relation between FR Is and FR IIs is key to resolving AGN unification schemes; differences in the observed radio jets (e.g., Bicknell, 2001), luminosity differences (e.g., Heckman et al. 1994), and morphological differences (e.g., Parma et al. 1992) among others makes reconciliation of these two classes a nearly impossible task and Marscher (2005) notes that nothing short of a multi-waveband approach across the EM spectrum would be required to achieve this feat.

The observed variations in the radio jet properties of both classes are directly associated with the differences in host galaxy properties and environment, with typical FR Is found to lie at the centre of optically bright galaxy clusters whereas the FR II counterparts live in isolation or poor groups. Nonetheless, observational evidence have shown that at higher redshifts ($z \sim 0.5$), both classes do live in rich cluster environments (e.g., Hill & Lilly, 1991). Similarly, the luminosity ranges for both classes have been observed to overlap at higher radio frequencies by two orders of magnitude (e.g., Laing et al. 1983; Morganti et al. 1993). Except for these

fractional overlaps, the classification of radio loud sources into two distinct morphological groups (i.e., FR Is & FR IIs) by Fanaroff and Riley has proven remarkably robust and underpins many of the current studies of radio-loud AGNs. It is of interest to mention here that more recently attempts have been made by researchers to further classify a new group of Fanaroff and Riley class of radio galaxies – the so called FR 0s – which in spite of sharing typical FR I characteristics are more core dominated (by a factor of ~ 30) than FR Is and exhibit a clear deficit of extended radio emission (see; Baldi, Capetti & Giovannini, 2016 for review).

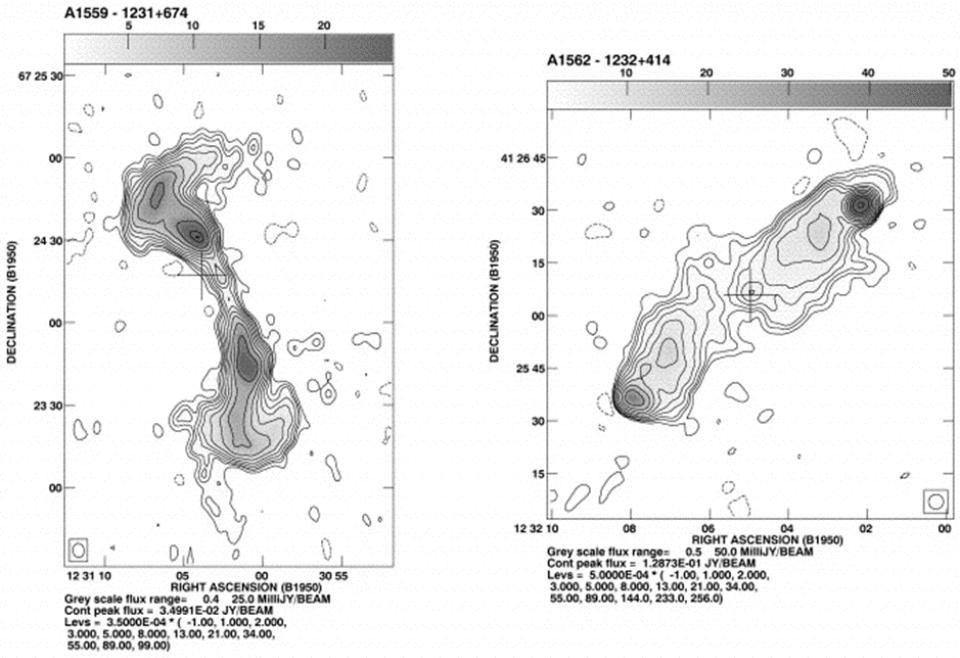

Figure 2: Radio maps of the two distinct Fanaroff and Riley class of radio galaxies. Left: a low luminosity (FR I) radio source with diffuse structures and symmetric jets originating from the core. Right: a classical double (FR II) radio source with huge radio lobes and bright hot spots, jets are often too faint to see. (Adapted from Owen & Ledlow, 1997).

1.2.4 Low and High Excitation Radio Galaxies

In addition to the spectroscopic classification of radio galaxies into NLRGs (including: Seyfert 2s, FR Is and FR IIs) and BLRGs (Seyfert 1s and FR IIs), these objects can broadly be divided into low-excitation radio galaxies (LERGs) and high-excitation radio galaxies (HERGs) (e.g.,

Hine & Longair, 1979), and as noted by Laing et al. (1994), the division is primarily based on the strength of excitation in their emission line (e.g., [OIII]) spectra. Low-excitation radio galaxies are almost entirely FR Is with a significant population of low-luminosity FR IIs, whiles HERGs are almost exclusively FR IIs and encompass all NLRGs and BLRGs. Compared with HERGs, LERGs have accretion of $\leq 1\%$ Eddington rate, are quiescent, associated with massive galaxies, richer environments, and have a broad range of integrated degrees of polarisation (e.g., Hardcastle, 2003; Smolcic, 2009; Best & Heckman 2012; O'Sullivan et al. 2015).

Early works on unified schemes of radio-loud AGNs (e.g., Scheuer 1987; Barthel, 1989) posited that physical properties of these objects including their clustering environments must be identical. However, these conclusions have been found in later studies to favour *only* high-z radio sources (e.g., singal, 1993). At low-z, there exist a fundamental problem in reconciling radio sources with the clustering environments in which they live, and as noted by Hardcastle (2003), the simple unified model of Barthel (1989) breaks down, for example due to the absence of low-z FR II quasars. In line with this observation, Laing et al. (1994) conclude that LERGs – which are predominant at low-z and low FR II luminosities must form a separate population of radio sources. In a related study, Hardcastle et al. (1998) provides a succinct conclusion on the subject by stating that, treating LERGs as a separate non-unified population and BLRGs as low-luminosity quasars could potentially solve the low-z problems for radio-loud unification models.

One of the fundamental requirements for the so called LERG/HERG dichotomy can be linked to the works of Laing et al. (1994); Jackson & Rawlings (1997); Hardcastle et al. (2006), in which they observed that many low-power radio sources with powerful ($\geq 10^{44}$ ergs^{-1}) jets do not have noticeable accretion disc, torus, BLR, or NLR; suggesting that their optical and X-ray nuclear emission originate entirely from the jet. Additional evidence for this sub-division have also come from systematic difference in their respective accretion mode, and Best & Heckman

(2012), highlights this argument by concluding that a simple scenario for the LERG/HERG dichotomy could potentially be linked with accretion rate in both classes. Hardcastle et al. (2006) and Smolcic (2009) have further shown that LERGs and HERGs exhibit differences in the way they accrete material onto their respective central SMBH; with LERGs having radiatively inefficient accretion compared with their HERGs counterparts (e.g., Evans et al. 2006; Best & Heckman 2012). Consequently, Croton et al. (2006) note that, these two distinct radio population may provide feedback in different ways. Indeed these observed differences between the isotropic properties of LERGs and HERGs, supports earlier conclusions by Hardcastle et al. (1998), that these two classes are physically different populations of radio sources. For a further reviews on the LERG/HERG dichotomy, the reader is referred to works of Hardcastle et al. (1998; 2006), Hardcastle (2003; 2013); Williams et al. (2016); and more recently Ching et al. (2017).

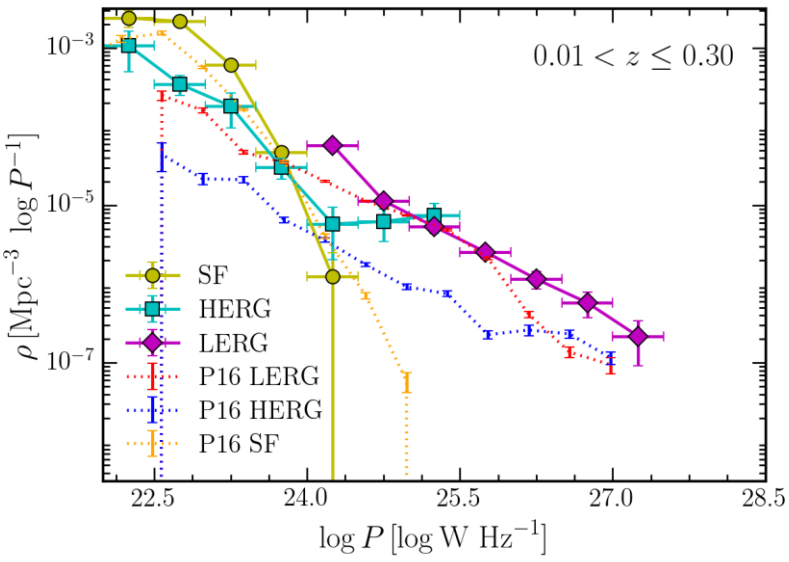

Figure 3: The radio luminosity functions for low redshift, 0.01 < z < 0.3, sample, separated into Star-Forming (SF), and AGN accretion modes – LERGs and HERGs. For comparison, the luminosity functions of Pracy et al. (2016), labelled P16, are included (scaled from 1:4 GHz and to the same units). Adapted from Williams et al. (2016).

1.2.5 The Radio AGN Duty Cycle

The birth, life, death and rebirth of radio galaxies is in many facets analogous to our own human existence and directly points to the universality of re-creation across all cosmic scales and time. In the 1950's the identification and emission mechanism in radio sources were the key questions among researchers (e.g., Baade & Minkowski, 1954), however, by the 90's focus had been shifted from these early questions to rather obtaining an understanding of the lifecycles and evolution of radio galaxies (e.g., Dunlop, 1999; Tadhunter, 2006; Sun et al. 2015). These duty cycles which are intrinsically powered by outflows of relativistic jets from the central SMBH have direct consequence on feedback, structure formation and black hole growth (see section 1.2.5) below. To resolve this however will require an answer to the question of *"what actually fuels radio AGNs in the first place?"*

One of the earliest attempt to resolve the fuelling issue can be traced back to the work of Shlosman, Frank & Begelman (1989); and later conclusions that starburst always accompanies the inception of AGN activity (see; Kaufman et al. 1999) have been found to be empirically consistent with the mathematical relation:

$$\dot{M}_t \simeq (1.4\times10^{11}\, g\,\mathrm{sec}^{-1})\left(\frac{M}{M_\otimes}\right)^2\left(\frac{\rho_\infty}{10^{-24}\, gcm^{-3}}\right)\left(\frac{C_s}{10 kms^{-1}}\right)^{-3} \qquad (1)$$

which suggests that SMBHs at the centres of active galaxies accrete material from the interstellar medium via the *Bondi accretion*. Note that equation (1) above is a numerically scaled solution of the Bondi accretion for AGNs (See; Bondi, 1952 for original derivation). $\dot{M}_t$ is the rate of accretion onto the galactic SMBH, ρ_∞ is the density of the interstellar medium and C_s the velocity of infalling material or *sound speed* in the surrounding medium if the infalling material has velocity lower than the sound speed. Note however that, the fuelling mechanism at play may not necessarily be same in all AGNs. For example, the conclusion that

FR Is have weaker accretion disks due to their faint nuclear X-ray and UV emission at a given radio power raises the question of whether or not there is a different accretion mode at work in these class of radio AGNs (e.g., Fabian & Rees, 1995). Best & Heckman (2012), further argue that high excitation radio galaxies (HERGs) are fuelled at high rates through radiative accretion disks by cold gas, while their low excitation counterparts are fuelled via radiatively inefficient flows at low accretion rates, often by gas associated with the hot X-ray haloes of their host galaxy/cluster. In spite of the absence of a simple AGN fuelling mechanism to date, there is overarching certainty that at later stages of their life cycle the accreted fuel is reduced significantly through a host of activities (see Sanders et al. 1988 for review).

Perhaps the single most important question in the radio AGN duty cycle paradigm rather would be what the active phase (lifetimes) of the central engine of these radio sources are. Schmidt (1966) offered a way for statistically estimating these lifetimes as:

$$t_{RG} \simeq \frac{N_{RG}}{N_E}(t_E) \approx 10^8\, yrs \qquad (2)$$

Where t_{RG} is the harmonic-mean lifetime of a radio galaxy (may include episodic activities), N_{RG} and N_E are number densities of radio galaxies and their parent population elliptical galaxies, respectively, and t_E is the lifetime of an elliptical galaxy. The physical interpretation of Equation (2) above is that the fractional representation of an AGN population gives its lifetime.

Recent observational evidence of longer (more frequent) duty cycles in massive galaxies suggest that these galaxies are capable of sustaining cooling flows which provide fuel to their central SMBHs. This long sustained feedback is known to correlate with the observed galaxy luminosity function in massive galaxies (see; Benson et al. 2003 and references therein) and a

direct consequence of the so called *episodic activity* which points to a "birth-death-rebirth" concept in radio AGNs (e.g., Baum et al. 1990; Schoenmakers et al. 2001; Saikia & Jamrozy 2009). These repetitive activities are characterised by diffuse remnants of a radio source fitted within the previous epoch of activity as observed by Schoenmakers et al. (2002). The plausible explanation for this occurrence is that the radio galaxy turned off at some point in its lifetime and turned back on. The concept of lifetime estimation has further prompted the use of both dynamical (e.g., Capetti et al. 1999) and spectral (e.g., Murgia et al. 2011) age estimates to constrain duty cycles, with low and high power radio sources currently thought to have ages of ($\sim 10^{7-8}$ years) and ($\sim 10^{6-7}$ years) respectively.

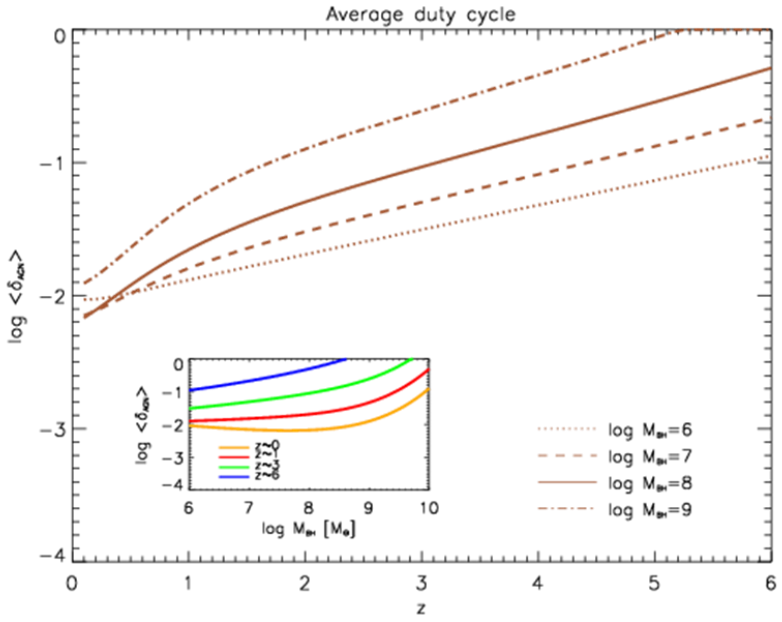

Figure 4: The average AGN duty cycle $\langle\delta_{AGN}\rangle$ as a function of redshift z, for different BH masses; $M_{BH} = 10^6$ (dotted), 10^7 (dashed), 10^8 (solid), and $10^9\ M_\odot$ (dot-dashed). The inset illustrates the AGN duty cycle as a function of BH mass at different redshifts; z=0 (orange), z=1 (red), z=3 (green), and z=6 (blue). (source; Aversa et al. 2015).

Obviously there remain more questions than answers at present regarding the perpetual duty cycles of radio AGNs, but what we do know is that activity is triggered once infalling material reaches the central accretion disk with the resultant activity dependent on the fuelling rate and

black hole mass and spin (e.g., O'Dea, 2001). The jets or collimated outflows of electron-positron plasma from the host galaxy central engine, which are emitted in the active phase form the foundations of the present study. In the section to follow, I discuss the context within which these radio AGN activities play a leading role.

1.2.6 Feedback, Structure Formation and Black Hole Growth

Understanding how galaxies and large scale structures form and evolve over cosmic time is one of the main challenges for present day astronomy and among the key drivers for many of the current and future large area surveys and instrumentation. To achieve this goal however will require studying the *relevant* comic species across all cosmic time and scale. In line with this, Urry & Padovani (1995) argue that understanding radio AGNs is essential to our understanding of the formation and evolution of the universe.

By virtue of their efficient coupling with both the ISM and IGM (e.g., Tadhunter, 2008), suitably-tuned feedback of energy and momentum (e.g., Birzan et al. 2008) from AGN activity is thought to be responsible for the properties of structures we see today in the observable universe, as well as the relationship between galaxy bulge and central SMBH masses (e.g., Ferrarese & Merritt, 2000). Tadhunter et al. (2012) shed further light on this argument by concluding that gaining insight into triggered radio-loud AGN activity is vital since relativistic outflows and lobes of such AGN provide one of the most important forms of AGN induced feedback. This notwithstanding, Morganti et al. (2010) also draw attention to the fact that such AGN feedback activity can have both constructive and destructive effects. More recently, in an attempt to develop a simple model for AGN feedback in nearby early-type galaxies, Kaviraj et al. (2011) observed that the coupling between AGN energy and the cold gas reservoir can be estimated by a 'feedback function' (f_t), which relates the observed bolometric luminosity, L_B of the AGN as:

$$f_t.L_B.\delta t = G.M.\delta M_g / R \qquad (3)$$

Where G is the gravitational constant, R and M are radius and mass of the galaxy respectively, δM_g is the cold gas mass removed from the reservoir, and δt is the size of the timestep being considered. Although not the main subject of this study, it is important to note that to date, two modes of AGN feedback have been proposed; (1) the kinetic or radio-mode feedback which primarily occurs in cool central galaxy clusters and groups where energy input from AGN jets resulting from activities in the central engine heat up the ICM and regulates accretion and star formation; and (2) the radiative or quasar-mode feedback which occurs in very luminous AGNs and characterized by slower winds of both ionized, neutral atomic, and molecular matter (e.g., Fabian, 2012; Voit & Donahue, 2015; Fiore et al. 2017).

In the case of structure formation, observational evidence suggest that starburst activity is closely linked with AGN activity (exception; radio-loud AGNs), with much of the observed emission line spectrum and the UV-optical spectral energy distribution being contributions from the starburst (e.g., Terlevich et al. 1992; Lawrence, 1999). In connection to this, Sanders et al. (1989) had previously posited a plausible sequence of galaxy interactions in which starbursts precede AGN activity. Furthermore, quantitative estimates of the power inferred from cavities also shows a correlation with cooling luminosity suggesting that the energy input from radio AGN feedback mechanism has the potential of resupplying cooling gas on large scales (e.g., Fabian, 2012); with jets driving shocks and outflows in the warm gas on scales of ~1 – 10kpc (e.g., Holt, Tadhunter & Morganti, 2008), influencing the star formation histories of the galaxy bulges.

In spite of the controversy that surrounded the correlation between the evolution of galaxies and their SMBHs in the recent past (e.g., Peng et al. 2006), current simulations and observational evidence seemingly allay this debate. There exists strong evidence of a tight

correlation between SMBH mass (M_{BH}) and host bulge mass (M_{Bul}) properties (e.g., Fabian, 2012; Kormendy & Ho, 2013) with winds and outflows from the central engine either heating or blowing cold gas out of the ISM of the host galaxy which results in either the formation or quenching of stars respectively (e.g., Schawinski et al. 2009). In relation to this, Hopkins et al. (2006) concludes that such coupled AGN feedback-induced activity of star formation could account for the observed $M_{BH} - M_{Bul}$ relation. Zubovas & King (2016) provide a succinct conclusion on the issue by recounting how AGN induced feedback has been included in current galaxy evolution models in order to – explain the drop-off in the galaxy mass function compared with the expected halo mass function above, $M_* \simeq 10^{11} M_\odot$; prevent the cooling catastrophe in galaxy clusters; and as well produce the scaling relations between galaxies and their central SMBH.

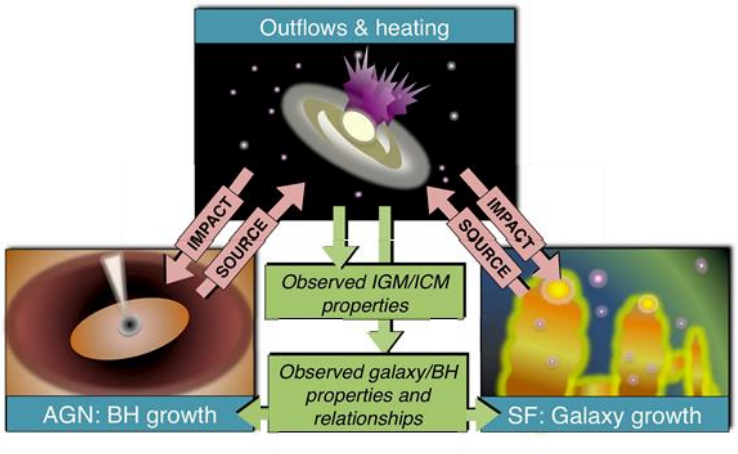

Figure 5: A schematic illustration of the possible connection between AGN induced feedback, structure formation and black hole growth. The enhancement or suppression of structure formation is heavily dependent on the total energy and momentum injected into the ISM/ICM through feedback induced activities and this consequently serves as fuel for the accreting SMBH growth. The ultimate result of all these feedback induced activities is evident in the observed variations in bulge properties of host galaxies. Image credit: Christopher M. Harrison (PhD Thesis, 2014.)

To this end, we can conclude that feedback, structure formation and black hole growth, which are a direct consequence of radio AGN activity and intrinsically powered by outflows of relativistic plasma from the host galaxy central engine have been invoked to elucidate our understanding of the formation and evolution of structure in the universe. The sections to follow will therefore be dedicated to the review of the dynamics and kinematics of these cosmic outflows.

1.3 Astrophysical Jets

Astrophysical jets are fast, collimated outflows of plasma from compact celestial objects. They are intrinsically bipolar with a jet-counterjet structure originating from the compact object and serve as conduits for mass, momentum, energy and magnetic flux transport (e.g., Das, 1999) to the surrounding medium. The ubiquity of this cosmic phenomenon is evident across a wide range of physical systems and scales – from less collimated outflows in Young Stellar Objects (YSOs) to highly collimated relativistic jets in AGNs hosting the most massive BHs at their centres (e.g., Blandford 2001), as well as intermediate scales between these two extremes. Indeed Shibata & Aoki (2003) observe that recent space observations of our sun reveals spectrum and time variability of emitted EM waves from the solar corona that are very much comparable to cosmic jets. Notwithstanding the vast range of physical systems from which they are produced, cosmic jets and outflows are thought to be driven by essentially similar physical mechanisms (e.g., Wiita, 2001). The first direct observations is credited to Curtis (1918) in relation to his detection of a streak of light from the nearby radio galaxy M87, however, the invention of the term *jet* as applied to these cosmic outflows was not until the 1950s when Baade & Minkowski (1954) in an observational study of the same galactic candidate (M87) likened the "protrusion" from the galactic core to a jet. Indeed by the late 80s, Clarke et al. (2008) note that extensive study of dozens of extragalactic radio jets had already been conducted.

In the case of radio AGNs – the objects of interest in the present study, the importance of these cosmic outflows stretches beyond their being primary channel of energy loss from accreting SMBHs to the major impact they have on their environment, with related particle acceleration producing the most energetic observable photons and hadrons in the universe. Although a great deal of progress has been made in the recent past to elucidate our understanding of these objects, their formation, collimation and acceleration still remain long standing questions in the field of astrophysical research (e.g., Urry & Padovani, 1995; Sikora et. al., 2005). In the sections to follow, I discuss the framework within which these outflows from AGNs have been studied to constrain their dynamics and kinematics across cosmological scales.

1.4 Extragalactic Relativistic Jets in Context

The jets in radio-loud AGNs otherwise known as extragalactic relativistic jets (ERJs) are thought to form by a combination of accretion, rotation and magnetic mechanisms (e.g. Pudritz et al., 2007). In addition to offering insight into the role of radio sources in the evolution of structure in the universe, ERJs are thought to be responsible for the production of the most energetic photons and hadrons in the observable universe (e.g., Sikora, 2004), with recent results from the Auger Observatory (Abraham et al. 2007) indicating cosmic rays with energies in excess of $6\times10^{19}eV$ originating in AGNs. The significance of these relativistic outflows as discussed in preceding sections is their distinctive role as cosmic vents for suitably-tuned feedback of energy and momentum from dense to diffuse phases of matter. Notwithstanding their cosmic significance, the quantitative study of these objects is rather extremely difficult, due primarily to their characteristic emission mechanisms – notably broad-band synchrotron (e.g., Hardcastle, 2006) and inverse Compton processes (e.g., Celotti, 2001). Major advancements in understanding the physics of these outflows on large scales have thus come from a multi-waveband approach (e.g., Worrall, 2004).

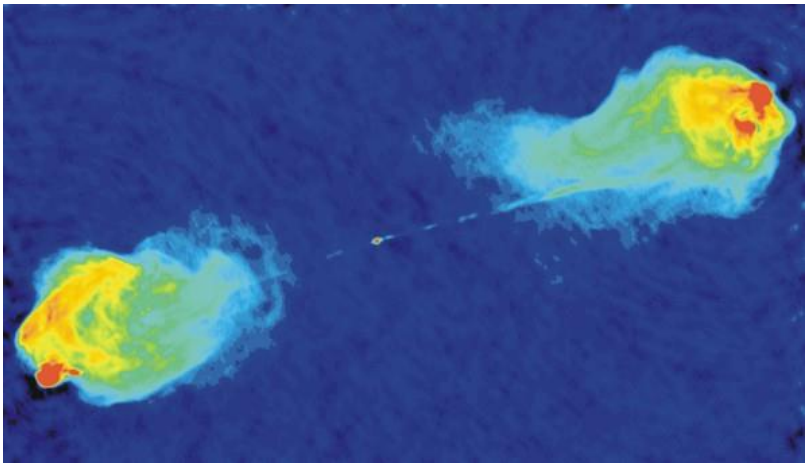

Figure 6: A false colour image of the powerful radio galaxy Cygnus A. The galactic core is indicated by the red spot at the centre of the map. The brightest radio emitting regions (lobes and hot spots) are indicated on either side of the core and connected by a collimated jet which can be seen as long narrow band from the central engine (Image credit: NRAO/AUI; Radio Observations by Perley, Carilli & Dreher, 1984).

1.4.1 Formation, Collimation and Acceleration

The formation of ERJs is known to primarily occur on approximately $\leq 100\,R_G$ scales by the so called magneto-hydrodynamic (MHD) processes (Blandford & Znajek, 1977) within the central engine of their host galaxies. Originally developed by Alfvén (1942), MHD is governed by equations of fluid dynamics and Maxwell's equations, and connects the plasma mass density, ρ; plasma velocity, V; the thermodynamic pressure, P; and the magnetic field, B. In spite of the complexity of plasma physics – not least in an astrophysical context, Blandford & Payne (1982) successfully demonstrated that relativistic jets can be launched magneto-centrifugally from the surface of an accretion disc, analogous to the outward spiral motion of a bead on a wire that is tilted enough and whirled about. In this scenario, some magnetic flux is assumed to be in open field lines at a certain angle of inclination with the disk's surface. These lines are fixed in the disk and rotate with it and as a result, ionised plasma is centrifugally accelerated along the field lines like the "bead" on the wire (e.g., Spruit, 1996). The ionised

material is in principle forced to follow the field lines since it cannot cross it resulting in collimation of the outflows (e.g., Clarke, 2008).

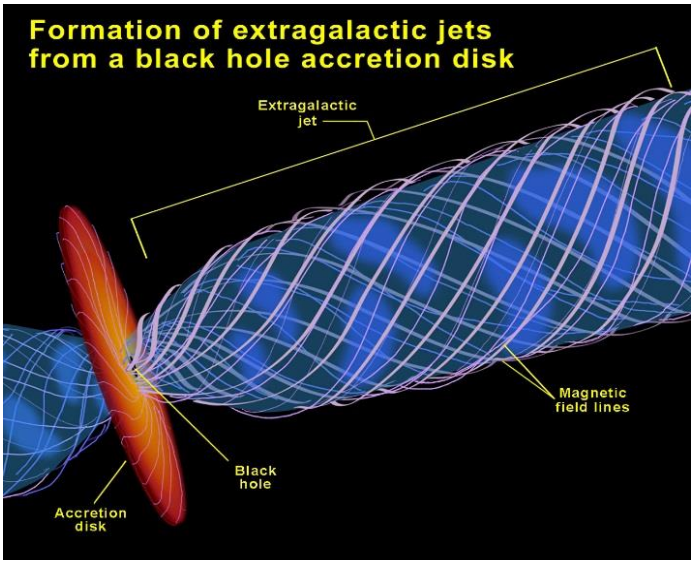

Figure 7: An artist impression of ERJ launching from a typical AGN as postulated by Blandford & Znajek. Magnetic field lines are threaded into helical patterns by the spinning BH and/or (rotating accretion disk – Blandford & Payne). These clearly defined field lines serve as funnels along which relativistic jets are launched and collimated from the surface of the disc. (Image credit: NASA/ESA & Ann Field, STScI).

Kadler et al. (2004) notes that only in radio-loud AGNs does the production, collimation, and acceleration of powerful relativistic jets take place; and these are thought to primarily consist of electron-positron plasma (e.g., Wardle et al. 1998; Kundt, 2014). Thus in a classical sense, MHD describes how gravity, magnetic field and pressure gradients influence plasma outflows from the compact core of radio-loud AGNs. Camenzind (2005) highlights this by drawing essentially similar conclusions, that ERJs are powered by conversion of rotational energy (of accretion disk or BH) into kinetic energy of outflows by a combination of strong electromagnetic field in the central engine and differential rotation mechanisms.

Although the work of Blandford & Znajek (1977) has stood the test of time, and remains the current most favoured model for the launching, collimation and acceleration of ERJs (e.g., Koide et al. 2002); it can be considered as the closest approximation rather than a true picture of the actual mechanism underlying relativistic jet formation due simply to the fact that MHD describes the large scale slow dynamics of plasma and thus valid for plasma speeds $\ll c$. Thus, the basic assumptions of MHD break when we consider relativistic speeds as in the case of ERJs. The concept of magnetic confinement (e.g., Eichler, 1993) once the jets are launched from the central engine, however makes the theory rather attractive. The inability to resolve this formation mechanism is largely due to insufficient resolution of previous and existing telescopes which has in practice placed limitations on the direct observations of the central engine.

1.4.2 The FR I versus FR II Jet Paradigm

It is widely established that both FR I and FR II radio galaxies to a certain extent, tend to have pairs of jets in the plane of the sky (e.g., Urry & Padovani, 1995); with the less collimated jets in FR Is terminating nearer to the galactic centre whereas the highly collimated FR II jets terminate at bright hotspots several distance away from the central region of the galaxy. However, in spite of the similar underlying physical mechanisms, the morphology, kinematics and dynamics of these jets is heavily subjected to variabilities in host galaxy properties and environment, and efforts to constrain the physics driving the observed jet structure (as in the present study) is of ongoing importance.

1.4.2.1 FR I Jets

These are relatively low power radio sources with twin jets that are initially relativistic on parsec scales, but decelerate from relativistic to sub-relativistic speeds on kpc scales. The jets exhibit considerable brightness asymmetry at their base (e.g., Parma et al. 1996), are subsonic

or transonic (i.e., no strong shocks are observed at their termination points) on kpc-scale velocities, and are both easily observed on large scales due to the absence of strong Doppler boosting effects (e.g., Worrall et al. 2007). Laing (1993) also notes that the orientation of the magnetic field configuration relative to the jets in these sources changes from longitudinal to transverse as the jet propagates. It is important here to draw the reader's attention to the fact that these characteristics may not be exact in some cases, particularly in the most powerful FR I sources. The rather turbulent environments within which these radio sources find themselves complicate the dynamics and kinematics of their emitted radio jets – with the so called observed tail-bending phenomenon as the jets propagate through the ISM/ICM (e.g., Blanton et al. 2000).

1.4.2.2 FR II Jets

FR IIs are the more powerful radio galaxies with jets that remain relativistic on all scales up to the hot spot. The jets are supersonic (i.e., strong shocks observed at their termination points) and often seen as one-sided jet (favouritism) or occasionally with no jets observed at all (Doppler de-boosting) usually on kpc scales (Bridle et al. 1994; Bicknell, 2001). The jets have shallow opening angles (< 4 deg) with knotty structures and magnetic fields that are predominantly parallel to the jet axis (e.g., Kembavi & Narlikar, 1999). The back-flow of the jets from the hot spots inflates, giving rise to over-pressured cocoons (huge radio lobes) observed as diffuse radio emission (e.g., Kuligowska, 2017).

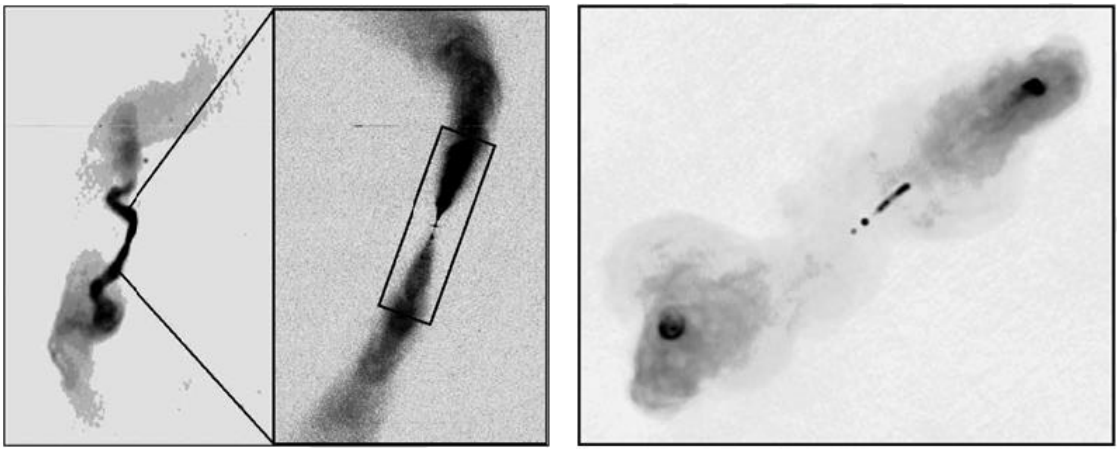

(a) (b)

Figure 8: (a) – VLA maps of the archetype FR I radio source 3C 31 (Laing et al. 2008) at 1.5 GHz (left-hand panel) and 8.4 GHz (right-hand panel) showing two-sided conical jet structures which terminates and flares into plumes, stretching to ~ 300 kpc from the galactic centre. (b) – VLA map of a classical double, FR II radio galaxy 3C 219 (Clarke et al., 1992) at 1.4 GHz and 1.6 GHz showing bright hotspots in the two diffuse radio lobes on either side of the core. Note the one-sidedness of the jet which points towards the north and at least one knotty structure observed on the southern side some distance from the core. (Image credit: NRAO/AUI).

1.4.2.3 Jets, knots, Hotspots, Lobes and Plumes

It is well established that the internal dynamics of a supersonic jet beam are rich enough to allow the formation of structures such as knots, filaments and wiggles simply through dynamical instabilities associated with the jet itself (e.g., Stone, 1997) and these have indeed been observationally confirmed and studied in detail (e.g., Hardcastle et al. 2002; Laing et al. 2006a). In spite of the complex morphologies exhibited by extragalactic radio sources, jets, knots, hotspots, lobes and plumes to a large extent appear to be inherent features in these objects – with propagation of the emitted radio jets through the non-uniform ICM thought to predominantly shape the morphology (e.g., Foster, 2010).

One of the most prominent features observed in classical AGN jets are the so called bright knots (e.g., Steenbrugge & Blundell, 2007; Goodger et al., 2010) which are often seen as blobs of bright features within the moving jet. In spite of the absence of a simple theory to account

for the formation of these bright structures, which arise largely due to differences in radio galaxy morphology and environments; Shklovskii (1980) proposed a model in which the knots are treated as blobs of magnetised plasma emitted from the central engine and which upon interaction with the ambient medium produce the bright features. Indeed the model has been used by researchers to account for this knotty structure in jets (e.g., Qian et al., 1991; Godfrey et al. 2012). Other models such as "shock model" (Bicknell & Begelman, 1996) have also been proposed to account for the formation of these structures in jets.

Hotspots are bright components which are neither a core nor part of the main jet structure with peak brightness greater than any nearby structure within the jet (e.g., Leahy et al. 1997). They are the main sites for dissipation of energy carried by the radio jet from the central engine to the termination point with associated shock processes giving rise to synchrotron radiation. Some FR II radio sources are known to show multiple hotspots (e.g., Laing, 1982) – which in principle points to a continued outflow of plasma even after the jet termination point. Beam-deflection (see; Lonsdale & Barthel, 1998 and references therein) and fluid-dynamical interactions (e.g., Hardcastle, 2008) are among the proposed models used to explain this observed structure in jets.

Radio lobes are the most common large scale structures observed in typical radio AGNs. They are extended regions of emission either side of the galactic nucleus with filamentary substructures (e.g., Leahy, 1993). These diffuse structures are sites for the formation of hotspots (jet termination) of the more powerful FR II radio sources and in effect serve as "cavities" where production of intense radiation occurs. In separate studies, Liu & Pooley (1991) and Pedelty et al. (1989), respectively observed that brighter lobes and lobe lengths correlates with a steeper spectral index of host galaxies – and this have indeed been confirmed in more recent studies (e.g., Dennett-Thorpe et al. 2008). The importance of these diffuse structures lies in the fact that they offer good diagnostics into the active phase of AGNs and

thus have been used by researchers to constrain the physics of radio AGN activity (e.g., Walker et al. 2000; Shulevski et al. 2015).

Plumes are associated with tailed sources of the rather low power FR Is and in many facets a direct consequence of the turbulent environment within which these radio jets propagate. The dynamics of these structures is analogous to steam column from factory chimneys and thus easily affected by turbulence in the surrounding medium. Hardcastle (1998) notes that formation of these structures is often characterised by broadening at bright flare points tens of kpc away from the central engine into the characteristic plumes and tails – giving its name the so called wide-angle tail (WAT) sources. In line with this, Jetha et al. (2005) further assert that the jet-plume transition of WATs is a consequence of the dense cluster environment, with the cluster properties determining the location of the base of the plume.

1.4.2.4 The Tail Bending Narrative

It has been well established that the ICM is a turbulent system with discrepancies in temperature gradients, and density distributions among others (e.g., Hayakawa et al. 2006; Bourdin & Mazzotta, 2008; McCourt, Quataert & Parrish, 2013). Thus, we can logically conclude that tail-bending of radio jets in FR Is which are known to predominantly live in rich clusters and groups is a direct consequence of turbulence in the ICM. In line with this, Jetha et al. (2005) observe that the large scale plumes in WATs for example can be shaped (i.e., bent backwards) by interactions with their environments due to the relative motion of the host galaxy through the ICM. Bird & Martini (2008) essentially draw similarly conclusions that FR I sources may be FR IIs that encountered high-density environments as they arose from turbulent disruption of their lobes and entrainment of ambient gas. Indeed, numerous theories have been postulated to account for this observed phenomenon. Electrodynamic effects (e.g., Bodo, et al. 1985); gravitational bending (e.g., Burns, Eilek & Owen, 1982); buoyancy effects

(e.g., Worrall et al. 1995); ram pressure (e.g., Venkatesan et al. 1994); to mention a few are among the proposed theories to account for the tail-bending of these radio jets. However, in spite of the progress made in resolving the origins of bending, WAT sources with their characteristic luminosities near the FR I/FR II break (e.g., Hardcastle & Sakelliou, 2004), varied bending angles (i.e., 30 – 115 degrees) (e.g., O'Donoghue et al. 1993) and collimated jets which often travel several kpc into the ICM before flaring into plumes, present an unusual challenge. In an attempt to resolve this peculiar case of WAT jets, Hardcastle & Sakelliou (2004) in a study of selected WAT samples in the Abell clusters of galaxies concluded that jets in WATs terminate in a variety of ways, further underscoring the complexity of the physical mechanism that initiates the bending in these class of radio sources. For a detailed review on the topic of bending the reader is referred to Pinkney et al. (1994) and O'Donoghue et al. (1993).

1.4.3 Particle Acceleration and the Physics of Deceleration

1.4.3.1 Particle Acceleration

In spite of the knowledge that radio jets are responsible for the acceleration of high-energy cosmic rays (e.g., Hillas, 1984), the underlying physics of where and how particles are accelerated in the hotspots and jet knots remains an open question. Indeed several models have been proposed in the literature with shock waves resulting from interaction of the jets with the ICM/IGM as the basis (e.g., Stawarz, 2004). These interactions are thought to produce supersonic shocks allowing the acceleration of the external medium particles and the jet material as they transit the shock regions giving rise to the observed inflated radio lobes or cocoon (e.g., Kuligowska, 2017). In a non-relativistic case (e.g., Blandford & Eichler, 1987), these strong shocks are expected to be sites of particle acceleration via the first-order Fermi process with typical power law spectral indices. In principle, the formation of these shocks could arise from intrinsic velocity asymmetries within the jet flow itself (e.g., Rees, 1978) or

within the knotty structures due to jet reconfinement by the ambient medium (e.g., Sanders, 1983), or large-scale instabilities within the jet flow (e.g., Bicknell & Begelman, 1996).

Other existing models involve magnetic reconnection processes (e.g., Birk & Lesch, 2000) with Bisnovatyi-Kogan (2005) suggesting a possible oscillation-induced strong EM waves as potential particle accelerators at large distances from the nucleus near the jet, as well as at larger radii. Although strong evidence for these shock-induced models of particle acceleration has come from the radio through optical spectra of hotspots (e.g., Meisenheimer et al. 1989), the rare evidence of multiple hotspots in a given lobe suggests that particle acceleration is not restricted to one location in at least some examples (e.g., Hardcastle et al. 2007). Indeed an earlier report by Hardcastle et al. (2004) had indicated that X-ray emission from many hotspots is most likely synchrotron in nature pointing to the concept of on-going particle acceleration in the form of a well-collimated energy input. Observed spectral problems (e.g., Kraft et al. 2007) and spatial offsets (e.g., Hardcastle et al. 2002, Erlund et al. 2007) are further complications that expose the limitations of these current standard models.

1.4.3.2 The Physics of Deceleration

The mechanism of deceleration from relativistic to sub-relativistic speeds over scales of 1–10 kpc of FR I jets with its attendant flaring and brightening (e.g., Laing et al. 2006) is still an open question in the field of extragalactic jet physics. As posited by Laing et al. (1999), the observed asymmetries on kpc scales in these jets are consistent with the hypothesis that the jet velocities from the base are mildly relativistic, and that they decelerate further out – with the extent of the deceleration region and residual velocity after the deceleration has taken place, dependent on the total power of the source.

Considerable efforts have been made in attempt to resolve this deceleration puzzle. Notable among them is the concept of entrainment of ambient material which results in changes in the

jet flow dynamics from an initially relativistic speed at the jet base to sub-relativistic speed (as they decelerate further out) (e.g., Bicknell, 1994) – a scenario in which the initial deceleration is thought to require an entrainment rate that is extraordinarily close to predictions of mass loss by stars within the jet volume (e.g., Laing & Bridle, 2002b). A second possibility which is linked to the inner jets can be explained in terms of an abrupt deceleration of the jet due to reconfinement shocks – followed by intense interaction with the external medium (e.g., Nalewajko & Sikora, 2008).

Unlike in FR Is, Hardcastle (2007) notes that the jets in FR IIs remain relativistic, often out to scales of hundreds of kpc or more, until they decelerate abruptly at shocks which involve the direct interaction of the jet with the relativistic plasma that fills the lobes in which the jets are typically embedded, giving rise to the observed hotspots. Hardcastle et al. (2007) also draw attention to the fact that particle acceleration is directly linked to the deceleration regions of both FR I and FR II sources – suggesting a rather unusual similarity between jets of these two distinct sources. Indeed this is well in agreement with earlier work by Worrall, Birkinshaw & Hardcastle (2001) in which they posited that the rather common X-ray jet detections in powerful FR I sources hints at the likelihood that particle acceleration is always associated with jet deceleration in FR I jets. However, it is noteworthy that based on a photon index analysis, Harwood & Hardcastle (2012) observed that for *bona fide* FR Is, acceleration to higher energies is more likely to be less efficient. In spite of the considerable efforts made, a comprehensive understanding of the ongoing physical processes in the jets of FR Is and the hotspots of FR IIs will be critical to resolving both the physics of particle acceleration and deceleration – and in the present study we will attempt to solve a piece of the puzzle by constraining the physics driving the observed jet structure in FR I radio sources.

1.5 Radio Interferometry and Synthesis Imaging

The single most important factor in the study of celestial bodies at radio frequencies is the ability to reproduce an accurate image of the observed source from a collection of radio signals. In times past however, this was a daunting task as radio astronomers were limited by several factors as far as reconstruction of this true sky brightness distribution of celestial objects was concerned. This consequentially resulted in a trade-off between sensitivity (where focus is solely on mapping out extended or large scale structure at the expense of fine details) or resolution (in which fine details of astronomical maps are prioritized at the expense of coarse structure). Today, thanks to radio interferometry, these limitations are increasingly becoming a thing of the past, allowing us to conduct observations at high spatial resolutions without compromising the large scale structures of such celestial sources. The underlying philosophy of radio interferometry and synthesis imaging resides in the fact that through combination of signals from different antennas, one can create a very large effective aperture of the observable sky which can be used as powerful diagnostic tool to reproduce the true properties of the extraterrestrial radio source. The first notable application of interferometric observations was performed on the sun dating as far back as the mid-20th century (McCready, Pawsey & Payne-Scott, 1947). Inspired by the rather low resolution of single-dish radio telescopes, interferometry has evolved into what is now known as Very Long Baseline Interferometry (VLBI) in which radio telescopes are connected in *real time* across different cities and countries (e.g., e-MERLIN, EVN, VLBA, Global VLBI, etc.) – a technique which has been influential in large area and deep cosmological surveys in the last few decades. The results of this are evident in the ability to resolve on milliarcsecond spatial scales, the high energetic particles from the nuclear regions of distant massive galaxies through to accurate definition of the Celestial Reference Frame among others (e.g., Trimble, 2014).

The key parameter measured in interferometry is the spatial coherence function (e.g., Clark, 1999) and the primary assumption here is that the rather incoherent spatial intensity distribution of EM waves emitted by a celestial object at a particular frequency, I_V can be reconstructed from the spatial coherence function measured at two points with the interferometer elements, $V_V(r_1, r_2)$ (e.g., Middleberg & Bach, 2008). Samples are collected in the so called Fourier Transform plane (u-v plane) of the astronomical image with each point in the u-v plane corresponding to a discrete position and physical separation (baseline) of the interferometer elements. As Trimble (2014) wrote, the development of radio astronomy "has not been free of competition and controversy, at least partly because it is just a little difficult to understand how earth-rotation, aperture-synthesis interferometry works." Figure 9 below shows a two-element interferometer.

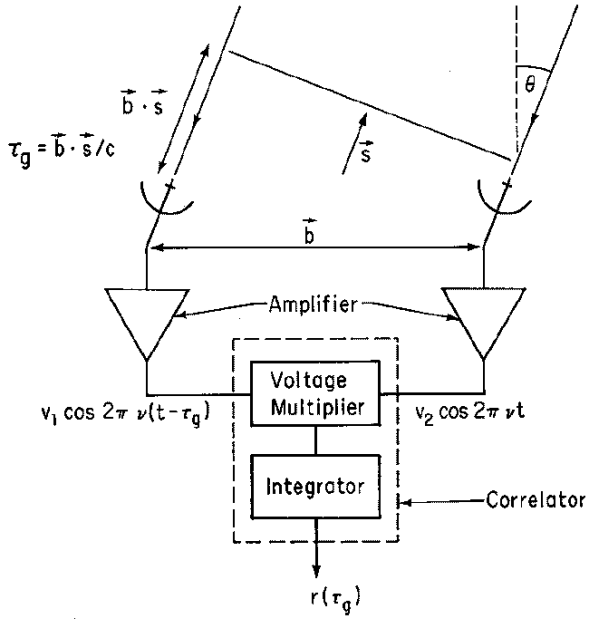

Figure 9: A simplified schematic diagram of a two-element interferometer. The projection of the station coordinates onto the (u, v) plane, which is perpendicular to the line-of-sight vector, ~s, yields the (u, v) coordinates of the antennas, measured in units of the observing wavelength. The correlator cross-correlates and Fourier transforms the signals from each pair of antennas to generate visibilities for reconstruction of the true brightness distribution of the sky. (Adapted from Taylor, Carilli & Perley, 1999).

The interferometer elements primarily produces two distinct quantities; signal in real channel (V_r),

$$V_r = \iint I_v(x,y)\cos\{2\pi(ux+vy)\}\,dxdy \qquad (5)$$

and signal in imaginary (V_i),

$$V_i = \iint I_v(x,y)\sin\{2\pi(ux+vy)\}\,dxdy \qquad (6)$$

Solution to equations (5) and (6) above yields the so called complex visibility function $V_V(u,v)$ which is simply a Fourier Transform of the spatial intensity distribution $I(x,y)$ of emitted EM radiation from the radio source evaluated at a given u-v distance from the projected baseline coordinates and is given by;

$$V_{(u,v)} = \iint I_v(x,y)\exp\{-2\pi i(ux+vy)\}\,dxdy \qquad (7)$$

Equation (7) above denotes the Van Cittert–Zernike theoreom (see; Zernike, 1938 for review). The coordinates (u,v) are vector components from the origin of the (u, v) plane to a point in the plane and measured in wavelengths; and (x,y) are direction cosines towards the radio emitting source. All interferometer elements measure the visibility function. However, to account for the sensitivity of individual elements in the interferometry (i.e., the antenna response), a factor, A_V, is often introduced. Equation (7) then becomes;

$$V_{(u,v)} = \iint A_v(x,y)\,I_v(x,y)\exp\{-2\pi i(ux+vy)\}\,dxdy \qquad (8)$$

After a typical interferometric observations, the goal then is to recover the true sky brightness distribution from the sampled visibilities which contains characteristic information on both amplitude and phase of the correlated radio signal observed. However, to achieve this one needs to first remove bad data and correct for amplitude and phase errors which commonly results from glitches in the receiver, and/or external factors. This procedure also known as data reduction in radio astronomy involves; (1) Flagging – inspecting the visibilities and removing all bad data; (2) Calibration – correcting the phase and amplitudes of the visibilities between the interferometry elements; (3) Deconvolution – recovering the true sky brightness distribution (real image) from the corrected visibilities (dirty image); (4) Self-calibration – using a model for the sky obtained in the deconvolution stage to further correct the phase and amplitudes of the visibilities in order to obtain an improved image.

The fact that radio interferometry samples astrophysical signals through incomplete Fourier measurements (e.g., Wiaux et al. 2009), has led to a great number of researchers developing several algorithms for optimum reconstruction of the true sky brightness distribution. These include: CLEAN (Hogbom, 1974); the Maximum Entropy Method (Ables, 1974); Compressed Sensing (Wiaux et al. 2009); WIPE (Lannes et al. 1994); Smear Fitting technique (Reid, 2006) among others. It is important here to bring to the attention of the reader that almost all of these deconvolution algorithms seek to either simplify and/or improve rather than invalidate an existing one. In the current study we have employed the classical radio astronomy deconvolution method – the "CLEAN" algorithm – a non-linear iterative process which eliminates artefacts from the sampled u-v plane by interpolating the visibilities to empty regions of the u-v plane. For a comprehensive review on interferometry and synthesis imaging in radio astronomy the reader is referred to the latest edition on the subject by Thompson, Moran & Swenson, (2017) and references therein.

In spite of the evolution of radio interferometry and advances in deconvolution algorithms, the technique still has its obstructions. The major trade-off in this field is interference from other objects (natural and manmade) also emitting at radio frequencies during observations – the so called Radio Frequency Interference (RFI). In particular our civilization revolves around radio frequencies – from mobile phone usage through to satellite technology; and the upshot of this is the characteristic mixing of these man-made radio waves with astronomical observations of the transient sky at radio wavelengths. With modern interferometers becoming increasingly more sensitive and powerful, and with the attendant huge volumes of data sets, Peck & Fenech (2013) concludes that creating a robust RFI mitigation technique has become indispensable. Indeed considerable efforts have been made in this regard at both the pre-correlation stage (e.g., Weber et al., 1997; Baan et al., 2004) and post-correlation stage (e.g., Briggs et al., 2000; Athreya, 2009) of the data calibration process, and it is worth mentioning here that efforts to automate these RFI mitigation techniques to ease the data cleaning process is already underway. Notable examples includes the Scripted E-MERLIN RFI mitigation PypelinE for iNTerferometry (SERPent) (Peck & Fenech, 2013) and the André Offringa (AO) Flagger (Offringa et al., 2010) – both of which have been employed in the present study. In the next section I introduce the two interferometric arrays employed for observations of our science targets.

1.6 The Interferometry Elements of the Present Study

1.6.1 The Jansky Very Large Array (JVLA)

The Very Large Array (VLA) is a relatively compact array of radio telescopes operated by the National Radio Astronomy Observatory (NRAO) in Socorro, New Mexico, United States. The array consist of twenty-seven antennas (each with a diameter of 25 metres) and a maximum baseline of 36 km. By means of rail pads, the antennas can be easily repositioned and this allows for flexibility in observations in four different configurations (i.e., A, B, C, and D) at

frequencies ranging from 1.0 to 50 GHz inclusive. Since commissioning in 1980, its first major upgrade (the Expanded Very Large Array – EVLA) was completed in 2012, and subsequently renamed as the Jansky Very Large Array (JVLA). Hereafter I simply refer to the instrument as the VLA. The telescope has in its nearly 40 years of existence demonstrated capabilities of a cutting edge ground base astronomical instrument and this is evident in the many discoveries made as well as the numerous citations it has enjoyed in astronomical refereed journals. There is currently ongoing discussions of a future facility: the next generation Very Large Array (ngVLA) with observing frequency up to ~100 GHz (twice the capability of the current VLA. For a detailed review of the upgrade and capabilities of the VLA see Perley et al. (2011) or visit the NRAO website at http://www.vla.nrao.edu/

Table 3: The VLA Band Characteristics

Band (GHz)	*Letter Code*	*Available Bandwidth[b] (GHz)*	*Antenna SEFD[c] (Jy)*	*Sensitivity[a] Continuum (μJy/beam)*	*Line (mJy/beam)*
1 – 2	L	0.7	400	5.5	2.2
2 – 4	S	1.75	350	3.9	1.7
4 – 8	C	3.5	300	2.4	1
8 – 12	X	3.8	250	1.8	0.65
12 – 18	Ku	5.5	280	1.7	0.61
18 - 26.5	K	8	450	2.3	0.77
26.5 - 40	Ka	8	620	3.2	0.90
40 – 50	Q	8	1100	5.6	1.4

Notes: (c): The System Equivalent Flux Density is a measure of the antenna sensitivity: SEFD = $2kT_{sys}/A_e$. It is the flux density of a source which doubles the system temperature. (b): An estimate of the effective bandwidth available, free of RFI. (a): The expected rms noise in a 1-hour integration at high elevation and under good weather conditions. For the Continuum case, the bandwidth utilized is that listed in column four. For the Line case, a bandwidth corresponding to 1 km/sec velocity resolution is assumed. (source; Perley et al. 2011).

1.6.2 The Expanded Multi-Element Radio-Linked Interferometer Network (e-MERLIN)

Like the EVLA, the expanded Multi-Element Radio-Linked Interferometer Network (e-MERLIN) is an upgrade to existing hardware and telescopes of the MERLIN array – a very long baseline interferometry (VLBI) consisting of seven radio telescopes (including: the Lovell Telescope, Mark II, Cambridge, Defford, Knockin, Darnhall and Pickmere) spread across the United Kingdom (UK) with an effective maximum baseline of over 217 kilometres. The array is the UK's national facility for radio astronomy and is operated by the University of Manchester from the Jodrell Bank Observatory (JBO) on behalf of the Science and Technology Facilities Council (STFC). Linked remotely, data from each telescope is sent via optical fibres to JBO where a correlator processes them into a single data set. The capabilities of e-MERLIN compare with leading ground and space based telescopes. At ~5 GHz frequency for example, e-MERLIN has a spatial resolution of 40 milliarcsec which is comparable to that of the Hubble Space Telescope at optical wavelengths (e.g., Kukula et al. 1996) and at ~1.4 GHz its angular resolution of ~200 milliarcsec is much higher than that obtained with the VLA at the same frequency (Biggs & Ivison, 2008). For an in-depth review of the array and capabilities of e-MERLIN the reader is referred to the e-MERLIN website (http://www.e-merlin.ac.uk). Table 4 below shows a summary of the capabilities of the e-MERLIN array.

Table 4: Technical Observing Capabilities of e-MERLIN

	1.5 GHz (L-band)	5 GHz (C-band)	22 GHz[8] (K-band)
Resolution[1] (mas)	150	40	12
Field of view[2] (arcmin)	30	7	2
Frequency range (GHz)	1.3 - 1.7	4 - 8	22 - 24
Bandwidth[3] (GHz)	0.4	2	2
Sensitivity[4] (μJy/bm)	5 - 6	1.8 - 2.3	~15
Surface brightness sensitivity[4] (K)	~190	~70	~530
Astrometric performance (mas)[5] (ICRF)	~2	~1	~2
Astrometric performance (mas)[6] (day-to-day)	~0.5	~0.2	~0.5
Amplitude calibration[7] (%)	2	1	10

Notes: 1: with uniform weighting, at the central frequency. 2: FWHM of 25-m dishes; reduced when the Lovell telescope is included. 3: Maximum bandwidth per polarization. 4: In a full imaging run with the Lovell telescope. 5: With respect to the ICRF (typical 3-deg target-calibrator separation using the VLBA Calibrator Survey). 6: Day-to-day repeatability using surveyed or in-beam sources, and assuming full imaging run. 7: Targets for day-to-day repeatability. 8: The Lovell telescope is not available at 22 GHz. The Lovell telescope may be included in the array at 1.5 and 5 GHz; this increases the sensitivity by a factor of between 2 and 3, but reduces the field of view (source: Argo, 2015).

(a) (b)

Figure 10: (a): Location map of the seven radio telescopes of e-MERLIN across the United Kingdom. Clockwise from top; Lovell, Mark II, Cambridge, Defford, Knockin, Darnhall and Pickmere. The longest baseline is 217 km, giving resolutions of 150, 40 and 12 mas at 1.3–1.8, 4–8 and 22–24 GHz respectively (source; Peck & Fenech, 2013). (b): Overall view of the VLA, looking south. The array can be reconfigured by moving the antennas to more distant pads via the rail lines visible in the photograph (Credit: Dave Finley, NRAO/AUI).

1.7 Scientific Rationale

The preceding sections have shed light on how radio AGN activity is powered by outflows from the host galaxy central engine and the relevance of these relativistic jets in placing cosmological constraints on feedback, structure formation and black hole growth. However, notwithstanding the progress made in previous years to elucidate our understanding of ERJs, an in-depth appreciation of the physics driving the observed jet structure from these radio-loud AGN populations is very much a work in progress and therefore serve as the primary motivation for carrying out the present study. To this end, we aim to measure the physical properties of extragalactic relativistic jets in two FR I radio sources in order to resolve the physics driving the observed jet structure.

1.7.1 Our Science Targets

In line with our science goals, we have carefully selected two FR I (3C83.1B and 3C465) radio sources from well-defined flux-limited samples at low frequencies (~178 MHz) from the LRL sample (Laing, Riley & Longair, 1983) whose surface-brightness allow us to image the jets in detail at L-band observations. Both science targets are representative of a range of morphological types of their kind; including large scale structures with plumes, the brightest example of narrow angle tail (NAT), and bent-double (wide angle tail - WAT) sources. The radio source 3C83.1B is associated with the elliptical galaxy NGC1265 in the Perseus cluster whiles the radio source 3C465 is associated with NGC7720, the dominating "diffuse" galaxy in the cluster Abell 2634. Indeed both sources have previously been studied (e.g., Bertola & Perola, 1973; Leahy, 1983; Sakelliou & Merrifield, 1999; Hardcastle & Sakelliou, 2004; Hardcastle, Sakelliou & Worrall, 2005) but the existing open questions in extragalactic jet physics – notably particle acceleration, the physics of deceleration, magnetic field configurations immediately surrounding jets, among others inspire our choice of these targets. In particular, while on large (~Mpc) scales the huge radio lobes observed in powerful radio

sources have been used to constrain the physics of radio-loud AGNs, the corresponding dynamics of these outflows on smaller (sub-kpc) scales are not well understood. Against this backdrop, we consider these two FR I jets with their characteristic faint but well-collimated inner regions as reliable candidates for constraining the physics of extragalactic relativistic jets on sub-kpc scales.

Table 5: Science Targets Demographics

Source	*Flux Density*			*Redshift*	*Spectral Index (α)*	*LAS*	*logP$_{178}$*	*Size*
	S$_{tot}$ (Jy)	*S$_{core}$ (mJy)*	*S$_{178}$ (Jy)*	*(z)*		*(arcsec)*	*(W/Hz/sr)*	*(kpc)*
3C83.1B	8.9	12	29.0	0.0255	0.6	1216	24.15	408.91
3C465	7.8	210	41.2	0.0293	0.75	603	24.79	346.54

Notes: The total and core flux densities quoted are in respect to the L-band (~1.5 GHz) observations deployed in the present study. Also stated are the flux density and logarithm (base 10) of the radio power at 178 MHz luminosity. The projected linear size (kpc) is estimated from the cluster redshift and largest angular size (LAS) – which is the angular distance between the most widely-separated regions in the radio source showing detectable emission (Adapted from; Leahy, Bridle & Strom – 3CRR Atlas).

1.7.2 The Complementarity of e-MERLIN in Resolving Jet Physics

Notwithstanding the vast spectrum of good existing radio and multi-wavelength data for the selected science targets, the complementarity to VLA observations by e-MERLIN (with its broad-bandwidth capabilities) in resolving jet physics on sub-kpc scales cannot be overemphasized. The formation of ERJs on $\leq 100\,R_G$ scales implies that direct study is possible only with VLBI techniques, supplemented by coordinated observations of time variability across the EM spectrum. However, detailed exploration of jet flows including; compositions, velocity fields, energetics, particle acceleration, magnetic fields and interactions with the environment can only be gained through deep, transverse-resolved radio observations and this until now has only been possible on $\geq 0.25\,\text{arcsec}$ scales with the VLA. We aim to extend these

techniques to smaller angular scales by measuring the physical properties of the jets in two powerful FR I radio sources obtained through the first ever deep, transverse-resolved radio observations using e-MERLIN, with complementary observations from the VLA in order to resolve the physics driving the observed jet structure.

With its combination of improved sensitivity, a resolution of $\approx 0.1\text{arcsec}$ and baselines that lie between those of VLA and VLBI, e-MERLIN serves as perfect candidate in complimenting either array for improved u-v coverage. Our aim therefore is to image L-band observations of the science targets from both the VLA (i.e., A and B configurations) and e-MERLIN and as a final step, combine these two observations to construct the highest resolution and sensitivity maps of the science targets to date in order to answer our key science questions including – the dynamics of radio jets in the vicinity of the AGN (jet velocities, magnetic field structures, powers, mass fluxes and entrainment rate), what initiates deceleration of low-luminosity jets on sub-kpc scales and the nature of jet particle acceleration. The addition of the VLA data will in principle provide the missing short spacings in the e-MERLIN data putting the compact structure in context and thus prevent image infidelity which may arise due to spatial frequency gaps. In the section to follow, we present the data and methods employed in the current study.

CHAPTER 2

Data and Methodology

2.1 Radio Observations

Our science targets were both observed at L-band (i.e., 1-2 GHz) using a bandwidth of 64 MHz. Observations of the targets at this frequency and in particular the two VLA configurations were undertaken in view of the scientific objectives of the present study – that is, the e-MERLIN array with its long baselines yielded higher angular resolution of the science targets, whereas the more diffuse large scale structure were contributed by the shorter baselines of the VLA to deliver the best possible instantaneous uv coverage, which is essential to constructing high fidelity images.

2.1.1 VLA Observations

Both 3C83.1B and 3C465 were observed in both the A-configuration and B-configuration. The data was taken with the new EVLA computer system controlling the array with observations conducted in full polarization mode – using the bright source 3C48 as flux calibrator with all 27 antennas in 64 MHz bandwidth centred at 1.5 GHz in 16 adjacent spectral windows. Each 64 MHz spectral window had 64 channels 1.0 MHz wide with 1 second and 3 seconds of integration time for A and B-configurations respectively. The total on source observations in each configuration for both targets was 1.23 and 1.22 hours respectively for 3C83.1B and 3C465.

2.1.2 e-MERLIN Observations

In the case of the e-MERLIN array, two separate observations were conducted for both science targets. Whereas all seven antennas were used in the two runs for 3C83.1B, the Lovell telescope was not included in the second run for 3C465. The observations were taken in full polarization – using the bright source 3C286 as flux calibrator with all available antennas in 64 MHz

bandwidth centred on 1.54 GHz, in 8 adjacent intermediate-frequencies (IF) and 2 seconds integration time. Each IF had 512 channels which was later averaged to 128 channels per IF. In the case of 3C83.1B, observations were conducted for 43.97 and 40.53 hours for the first and second runs respectively; whereas 3C465 had a total of 19.03 and 19.34 hours of on source observations for the first and second epochs respectively. The data were correlated with the e-MERLIN correlator at Jodrell Bank Observatory.

Table 6: Summary of radio observations

Source	VLA observations				e-MERLIN observations			
	A-configuration		B-configuration		Epoch-1		Epoch-2	
	Date	Time (h)	Date	Time (h)	Date	Time (h)	Date	Time (h)
3C83.1B	2012 Oct 31	1.2	2012 May 28	1.2	2016 Dec 21	44.0	2016 Dec 30	40.5
3C465	2012 Oct 31	1.2	2012 May 28	1.2	2015 Apr 12	19.0	2015 Apr 13	19.3

Notes: All observations were made at L-band (~1.5 GHz) with bandwidth of 64 MHz, and using 512 and 64 channels for the e-MERLIN and VLA respectively.

2.1.3 Post Correlation RFI Treatment

At L-band, observations of extra-terrestrial radio sources are considerably affected (usually, <20% - 25%) by radio emissions from GPS, satellites, etc. also emitting at similar frequencies and we need to adequately remove these interfering signals from the actual 'true' observations. This is essential for obtaining reasonable calibration solutions during the calibration process – which in turn has direct consequences for image fidelity in the deconvolution stage. Our mitigation strategy for post correlation RFI was executed through SERPent and AO Flagger for the e-MERLIN and VLA data sets respectively. Both are automated reduction and RFI-mitigation strategies employing the SumThreshold methodology – with SERPent typically run as a Parseltongue version of the AO Flagger algorithm which was originally developed for the LOFAR pipeline (see; Offringa et al., 2010 for a review). It is worth mentioning here that in the case of the e-MERLIN observations, mitigation of RFI with SERPent was performed on the 3C83.1B data set only. Although a daunting task and computationally expensive, we

manually inspected and flagged bad data from individual IFs, Channels, Baselines and Stokes Parameters (Polarizations) for the 3C465 data set from the e-MERLIN observations. This was aimed to acquire relevant expertise in manual inspection and editing of radio data and indeed the approach proved useful as we have successfully edited, calibrated and imaged the science target with reasonable rms noise level.

2.2 Radio Data Reduction

The main concept of the calibration procedure is to identify and discard any bad data within the sampled visibilities, and subsequently derive amplitude and phase corrections to obtain an accurate measure of the true sky brightness distribution of the science target. The Common Astronomy Software Application (CASA) package, version 4.6.0 and the Astronomical Image Processing System (AIPS) were employed for the calibration and imaging of the VLA and e-MERLIN data sets respectively. Visibility data are stored as Measurement Set (MS) in CASA whereas AIPS utilizes a FITS format for the u-v data set. The entire calibration was performed on the raw (un-averaged) data set for each observation. For practical reasons, only during the deconvolution stage did we average the respective data sets by channels (to reduce the data volume) and save computational time.

The CASA setup primarily functions underneath an iPython interface. This allows for flexibility with a user having options to either run the reduction process interactively through a set of tasks via the CASA interface or non-interactively as a Python script. In the present study, reduction of data was executed interactively and varied slightly in procedure between each data set, particularly in the extent of flagging, calibration and deconvolution parameters. Radio data reduction is not an arbitrary process but rather methodical in operation and guided by a distinct philosophy. Calibration of data in CASA and AIPS adopts essentially the same physical principles (albeit different tasks) to derive relevant calibration solutions. Against this

backdrop and for simplicity, we present here a more general description rather than data set specifics of the data reduction strategy employed in the present study as implemented in CASA. We draw the reader's attention to an important and distinct step in AIPS which at present is not implemented in CASA – the "Fringe fitting" technique. The technique is different from conventional delay calibration as implemented in CASA in that the data is kept in the time and frequency domain (as opposed to the time and delay domain). Corrections for residual delay and rate error can then be derived as phase corrections as a function of time and frequency. The data can then be averaged in time and/or frequency after the corrections are applied; see Cotton, (1995) and references therein for review. With e-MERLIN, delay offsets on individual telescopes can be up to a few hundreds of nanoseconds particularly on longer baselines. Unlike the VLA, these delays cannot be corrected on a single scan but rather must be corrected as a function of time. AIPS utilizes the task "FRING" which fits and corrects for both delays and rates on the entire data set. This "Fringe fitting" is a standard technique in all VLBI observations – and is necessary for e-MERLIN – so we needed to use AIPS for the e-MERLIN data reduction.

2.2.1 The Calibration Process as implemented in CASA

i. **Data Examination and Flagging** [tasks: listobs, plotants, plotms, plotcal, flagdata]: With task [listobs], we begin by first inspecting basic information on the observing run such as, listing of individual scans, integration time, the frequency setup, channels, source list, spectral windows, etc. Even after executing the automated RFI flagger on the visibilities, the initial stages of data reduction involves examining the data sets and removing any remaining bad data which could originate in a number of factors ranging from bad weather conditions to inaccurate determination of antenna baseline positions during the observation. These bad data were flagged and the visibilities re-examined

for exactness before calibration. Also, a suitable "reference antenna" is identified at this stage for calibration purposes. Note that the list of tasks specified here were used essentially throughout the calibration process for checking calibration solutions and where necessary removing remaining bad data from the visibilities.

ii. **A Prior Antenna Position Correction** [task: gencal]: Since the visibilities is a function of u-v distance, any incorrect baseline position will result in incorrect estimation of u and v, and consequently errors in the final image. Although in practice this step could be executed at a later stage by a baseline-based calibration, the observer log had information on antennas with no good baseline positions, and thus it was useful (with this prior information) to perform this step in order to incorporate any improved baseline positions prior to the actual calibration.

iii. **Initial Flux Density Scaling** [task: setjy]: Here a flux density value (model) which is estimated from an analytical formula for the spectrum of the source as a function of frequency is provided for the amplitude calibrator – and at later stages of the calibration process transferred to the secondary and polarization calibrators. The idea is to assume a known flux density for a primary calibrator source and, by comparison with the observed data for that calibrator, determine the amplitude antenna gains, g_i .

iv. **Initial Phase Calibration** [task: gaincal]: This step involves solving for phase variations as a function of time on the calibrator sources. In particular, considerable gain variations between different scans of the bandpass calibrator may arise when scans happen at much different elevations. Unlike amplitudes, variations in phase can result in de-correlation when vector averaging the data to compute the final bandpass solution during the bandpass calibration step and hence this step is necessary.

v. **Bandpass Calibration** [task: bandpass]:

- **Delay Calibration** [task: gaincal]: Before deriving the actual bandpass solution, we first solve for the so called antenna-based delays with respect to our chosen reference antenna. These delays introduce phase jumps against frequency channel in each spectral window and therefore must be corrected. Once the delay corrections are obtained, we can form the actual complex bandpass, B_i solution to account for any gain variations with frequency in the visibilities.

vi. **Gain Calibration** [task: gaincal]: Here we derive corrections for the complex antenna gains – i.e., both amplitude, g_i and phase, θ_i. The strategy here is to first derive appropriate complex gains for the flux density calibrator, and then obtain the complex gains for a position on the sky close to the target using the phase calibrator, and finally derive the complex gains for the polarization calibrator source as well.

vii. **Polarization Calibration** [task: polcal]: There are primarily two steps involved – (a) solving for the instrumental polarization (frequency-dependent leakage terms) using an unpolarised source and (b) deriving the polarization position angles relative to a source with known position angle. First we set a model for our polarization calibrator using task [setjy] and subsequently;

- **Solve for cross-hand delays** – which may arise due to residual delay variance between the R and L terms on the reference antenna.
- **Solve for leakage terms** – using the unpolarised calibrator source to solve for the instrumental polarization (leakage solutions), with Q and U stokes parameters in the model data set to zero.
- **Solve for R-L polarization angle** – using the unpolarised calibrator (whose position angle was set earlier in task [setjy]) to obtain an accurate polarization position angle for the R-L phase.

viii. Scaling the Amplitude Gains [task: fluxscale]: Here we obtain the true flux density of the secondary calibrator by deriving the system response to the primary (flux) calibrator and assume that the mean gain amplitudes for the primary calibrator is equal to that of the secondary calibrator.

ix. Applying the Calibration [task: applycal]: At this stage we have derived all relevant calibration solutions and our job here is to apply these solutions; firstly to each individual calibrator source using the gain solutions derived on that particular calibrator alone to compute the *Corrected Data Column*, and secondly to the actual science target – linearly interpolating the gain solutions from the secondary calibrator.

x. Imaging/Deconvolution [task: clean]: Here we split off the calibrated science target from the visibilities with suitable channel averaging (to save computational time) using task [split]. Recall from section 1.4 above that the sampled visibilities are simply a Fourier transform of the sky convolved with a sampling function $V(u,v)$, which has absolute value of zero where no measurement is made or unity if otherwise. The instrument's point-spread-function $B(x,y)$ is then the Fourier transform of the sampling function;

$$B(x,y) = V^*(u,v) \qquad (9)$$

Where $V^*(u,v)$ is a Fourier transform of the u-v coverage.

Since the visibilities do not completely sample Fourier space, $B(x,y)$ contains much structure which affects the appearance of the Fourier-transformed image. The task [clean] in CASA eliminates this structure and can be viewed as interpolating the visibilities to the blank regions of the u-v plane. In practice, the Clark (1980) CLEAN algorithm for example adopts two cycles (major and minor cycles) to find approximate positions and strengths of the components using only a small area of the dirty beam. The minor cycle involves;

i. Selecting a beam area that includes the highest exterior sidelobe of the beam.

ii. Selecting points from the dirty image if they have an intensity, as a fraction of the image peak, greater than the highest exterior sidelobe of the beam.

iii. Performing a list-based Hogbom CLEAN using the beam area and the selected points of the dirty image.

The major cycle involves transforming the point source model found in the minor cycle via an FFT, multiplied by the weighted sampling function that is the inverse transform of the beam, transformed back and subtracted from the dirty image. Errors introduced in a minor cycle due to beam area approximation are corrected in subsequent minor cycles. For a detailed review on synthesis imaging in radio astronomy, see Taylor et al. (1999).

In view of the science goals of the present study, we employed *Briggs weighting*, with reasonable adjustment of the Briggs robustness parameter $(-2 \leq robust \geq +2)$ to obtain the highest resolution possible without compromise on sensitivity to large scale structures. After obtaining sufficiently good image of our science target from the first round of deconvolution, we embarked on the so called Self-Calibration process which typically involves using the obtained model image of the target to solve for new and improved complex gain values of the visibilities. This new calibration solution is then re-applied to the science target and the deconvolution process repeated. In principle there is no limit on the number of self-calibration iterations – the goal is simply to correct the visibility phases and amplitudes as highly as possible to obtain the highest image quality. Thus, the stopping criterion for self-calibration is when the image noise no longer decreases significantly after each cycle.

For a comprehensive review of synthesis calibration and imaging using CASA or AIPS, the reader is referred to the respective cookbooks on both software applications by the NRAO.

2.3 Jet Structure Reconstruction

2.3.1 Filling the aperture via array combination

Array combination from different interferometric elements allows for the reconstruction of the true sky brightness distribution of astronomical sources with the combined data set encompassing the projected baseline spacings of the different arrays thereby providing simultaneous sensitivity and resolution. Although a common practice in radio astronomy, data combination from very different interferometry elements – as is the case in the present study, can be relatively problematic due to fundamental differences in the structure of the visibilities from the different arrays – including differing numbers of intermediate frequencies, frequency channels and channel bandwidths (e.g., Muxlow et al. 2005). In principle, the combination can be achieved via the sky-plane or the u-v plane; and in spite of Muxlow et al. (2005) demonstrating the equivalence of both techniques in reproducing essentially identical images, Biggs & Ivison (2008) observe that combination in the Fourier plane is better able to constrain deconvolution algorithms such as CLEAN due to the improved u-v coverage in the visibilities making it superior to the sky-plane approach. Against this backdrop, we adopted the Fourier plane combination method in the present work.

2.3.2 Data Combination and Mapping

To account for differences in primary beam response due to differences in baselines, we calibrated and imaged separately the A and B-configurations of the VLA data sets before combining the two configurations with task [concat] into a single MS. A similar approach was used for the two e-MERLIN observing epochs to account for baselines that included the Lovell telescope and the non-Lovell baseline. The resulting data sets from the two interferometry elements were then used to create a complete e-MERLIN/VLA data set, again using task [concat] but this time with appropriate weighting scales for the two array visibilities to account for differences in the weighting schemes for the two arrays. Finding the optimum weighting

factor requires some form of verification by visual inspection, and in the present study we varied the weights and formed the dirty beam using wsclean to try to find the point where the baselines of the combined dataset were not dominated by that of the VLA. We obtained comparable statistical weightings for the two arrays with approximate factor of;

$$\left(\frac{w_{VLA}}{w_{e-MLN}} \propto \frac{3\times10^{-7}}{1} \right) \qquad (10)$$

This factor was used to essentially down-weight the VLA data so that its contribution in the combined data set would be low. This allowed us to construct total intensity maps of the combined data set with a beam size approximately equal to the e-MERLIN – only beam (~ 150 mas) in line with the science objectives of our study. Deconvolution of the e-MERLIN/VLA data set was executed with the *Briggs weighting* scheme – with *Briggs* robustness parameter set to -1.5 to give further weighting to the longer baselines contributed by the e-MERLIN visibilities.

CHAPTER 3

The jets and plumes of 3C465

3.0 3C465

In this paper, we present new high-resolution and high-sensitivity maps obtained from multi-configuration, multi-frequency VLA and e-MERLIN observations of the WAT source 3C465. The X-Band (~8.5 GHz) VLA data used in the present analysis was obtained from Hardcastle & Sakelliou (2004) and was observed in all four configurations (A, B, C and D) of the VLA with bandwidths of 25 MHz (for the A-configuration observations) and 50 MHz (for the rest). Throughout this paper, we assume a concordance cosmology with a density parameter for matter, $\Omega_m = 0.27$, density parameter for energy, $\Omega_\Lambda = 0.73$, and a Hubble constant $H_0 = 75$ kms^{-1} Mpc^{-1}. At the current best known redshift of 3C465 (z = 0.029), one arcsec is equivalent to a projected length of 0.56 kpc. Spectral indices, α, are defined in the sense $S_\nu \propto V^\alpha$. J2000 co-ordinates are used throughout.

3.1 An overview of the radio source

3C465 is associated with NGC7720, the dominating "diffuse" galaxy in the cluster Abell 2634, and is among the best studied WAT sources in the northern sky due to its proximity and peculiar morphology within this class of radio sources. Detailed imaging studies in the optical (e.g., Colina & Pérez-Fournon, 1990; Capetti et al. 2005), radio (e.g., Leahy, 1984; Hardcastle & Sakelliou, 2004) and X-ray (e.g., Schindler & Prieto, 1997; Hardcastle et al. 2005) observations of the source have previously been made. Its jet and hotspots as shown in our total intensity maps (Fig. 14) have been extensively studied and large-scale properties of the plumes (Fig. 14) are also well known. The tails of WAT sources generally bend in a common direction, resulting in their overall characteristic U, V, or C shape. These sources are generally assumed to form by motion of the host galaxy relative to the cluster: the host galaxies are thought to be nearly

stationary at the bottom of cluster potential wells, moving with velocities ~200 km/s in an oscillatory motion of small amplitude (<0.3 of a core radius) (e.g., Burns et al. 1982).

3.2 Radio maps

We present here total intensity maps from deconvolution of the VLA, e-MERLIN and e-MERLIN/VLA data sets of our science targets. The rather elliptical shape of the recovered primary beam in the e-MERLIN maps is a direct consequence of the relatively sparse distribution of antennas in the e-MERLIN array. This is typical of small arrays with each baseline sampling an elliptical track (not focused on the origin) resulting in irregular u-v coverage.

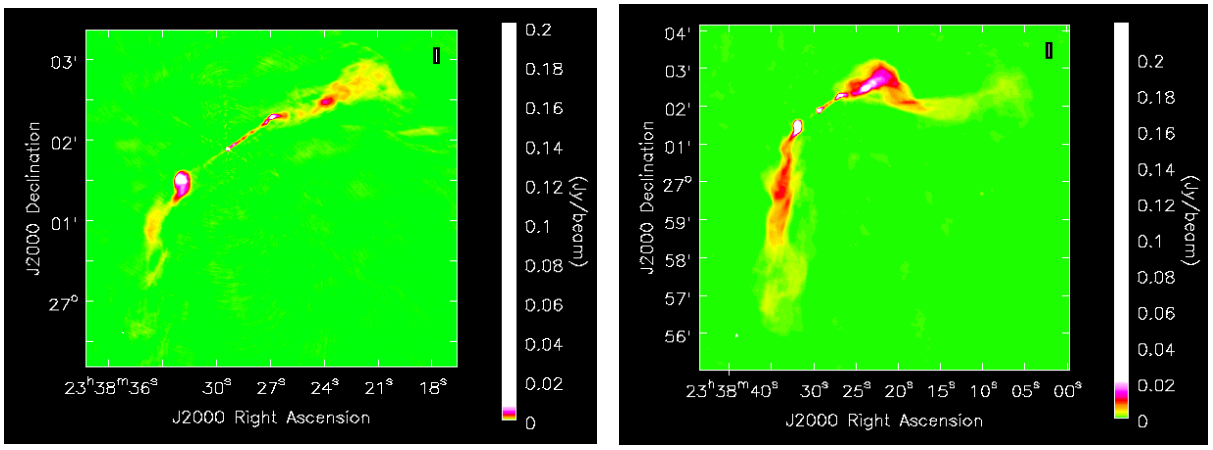

(a) (b)

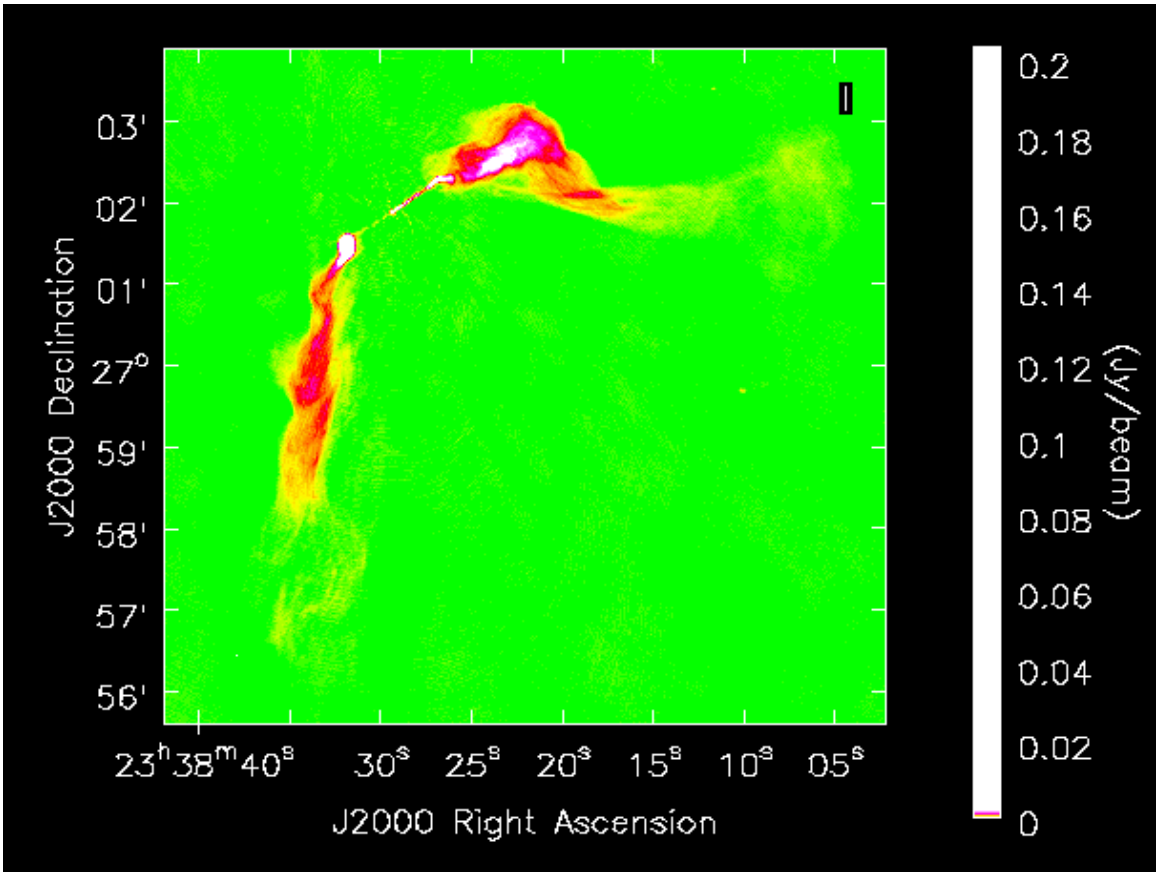

(c)

Figure 11: 1.5 GHz VLA maps of 3C465. (a) A-configuration at 1.4×1.1" resolution; (b) B-configuration at 4.1×3.8" resolution; (c) A+B-configuration at 1.4x1.1" resolution.

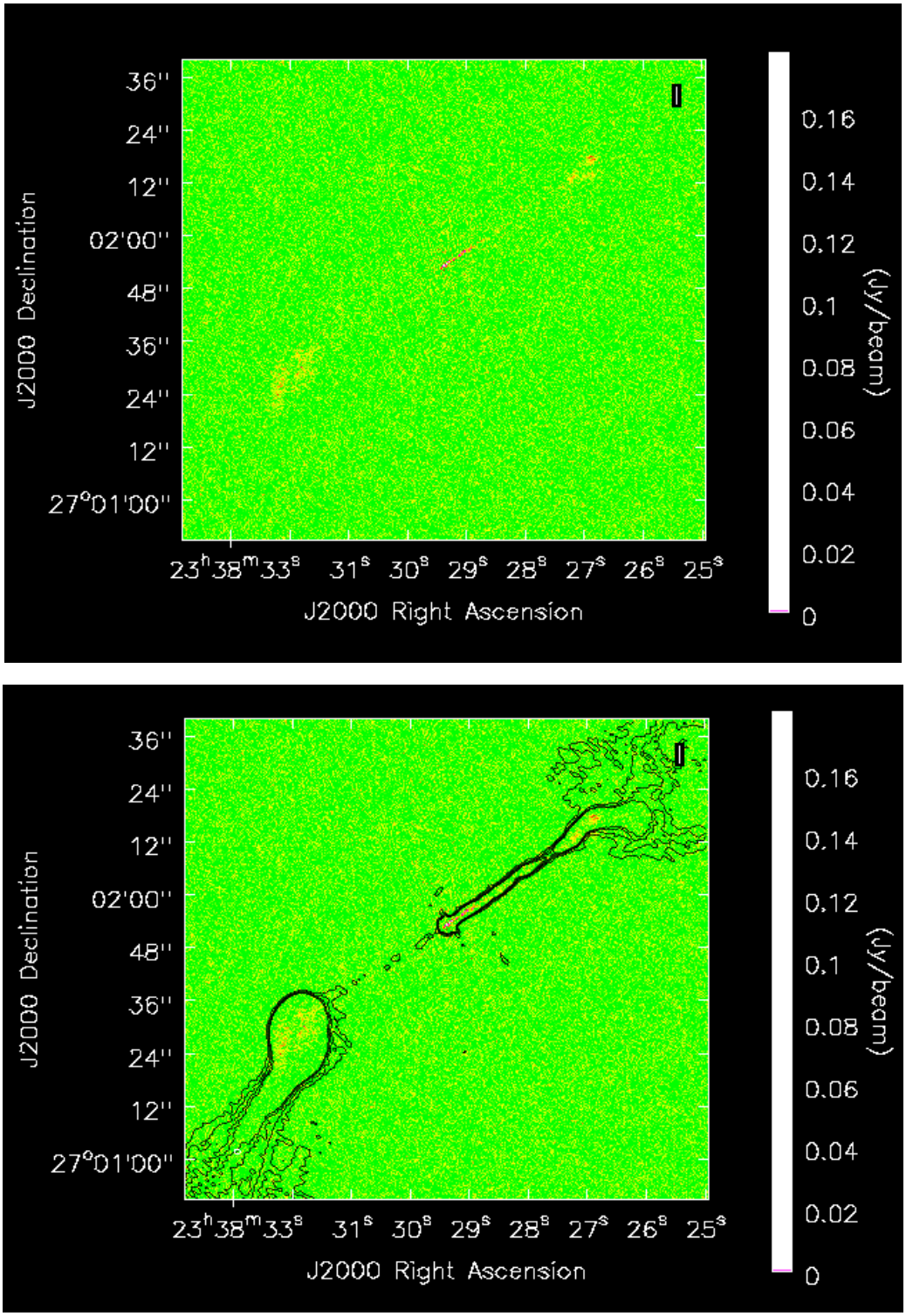

Figure 12: 1.5 GHz e-MERLIN maps of 3C465. Top: e-MERLIN only map at 0.27x0.15" resolution. Note the sidedness of the radio jet. Bottom: e-MERLIN map with superposed 1.5 GHz VLA contours (grey scale) showing the jet and hotspots, and parts of the extended structures (plumes).

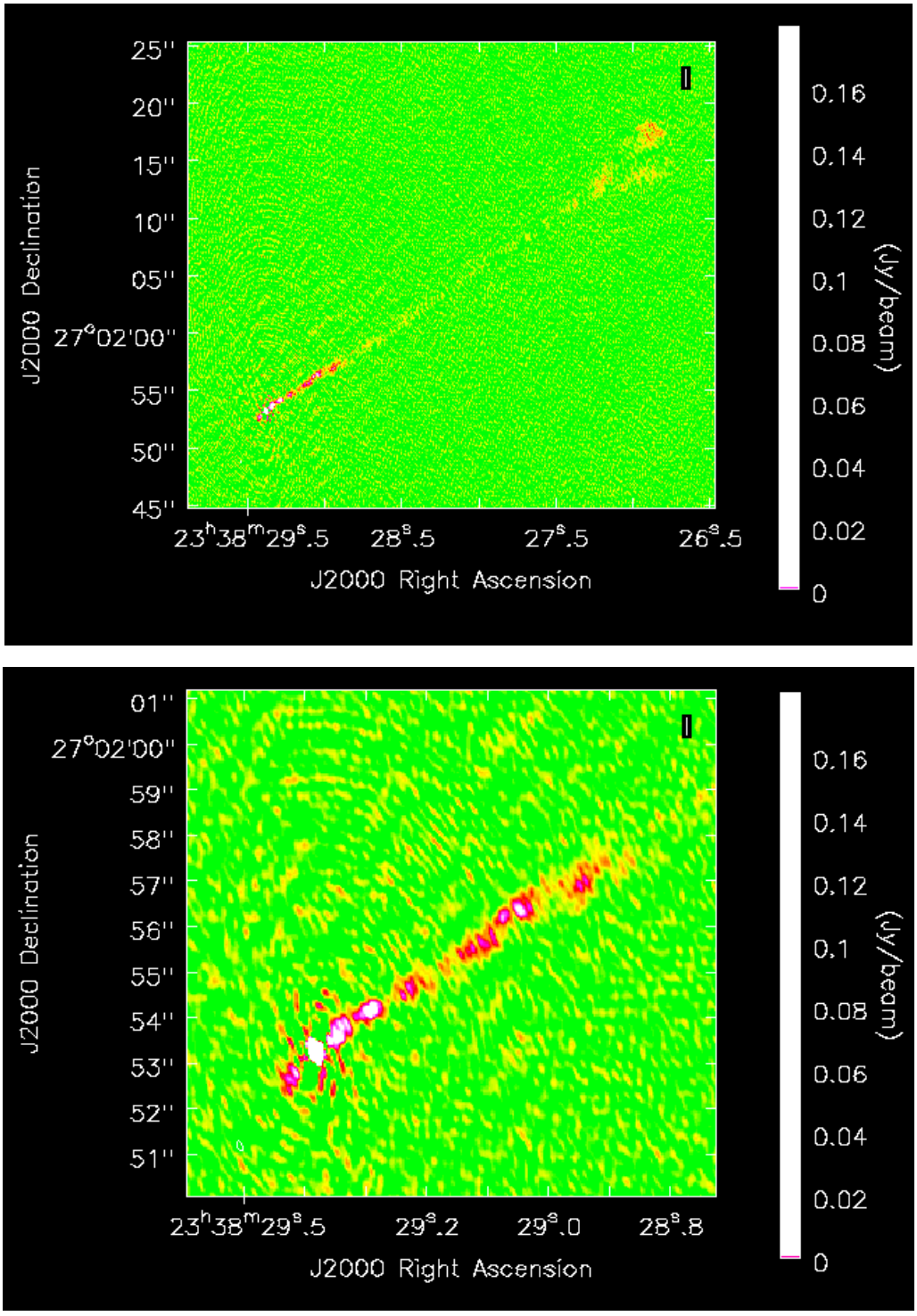

Figure 13: Top: 1.5 GHz e-MERLIN map of the jet region in 3C465 at 0.27x0.15" resolution. Bottom: Zoom in on the inner 5 kpc radius of the jet region showing the bright knotty structures at the jet base. Note the elliptical shape of the recovered primary beam.

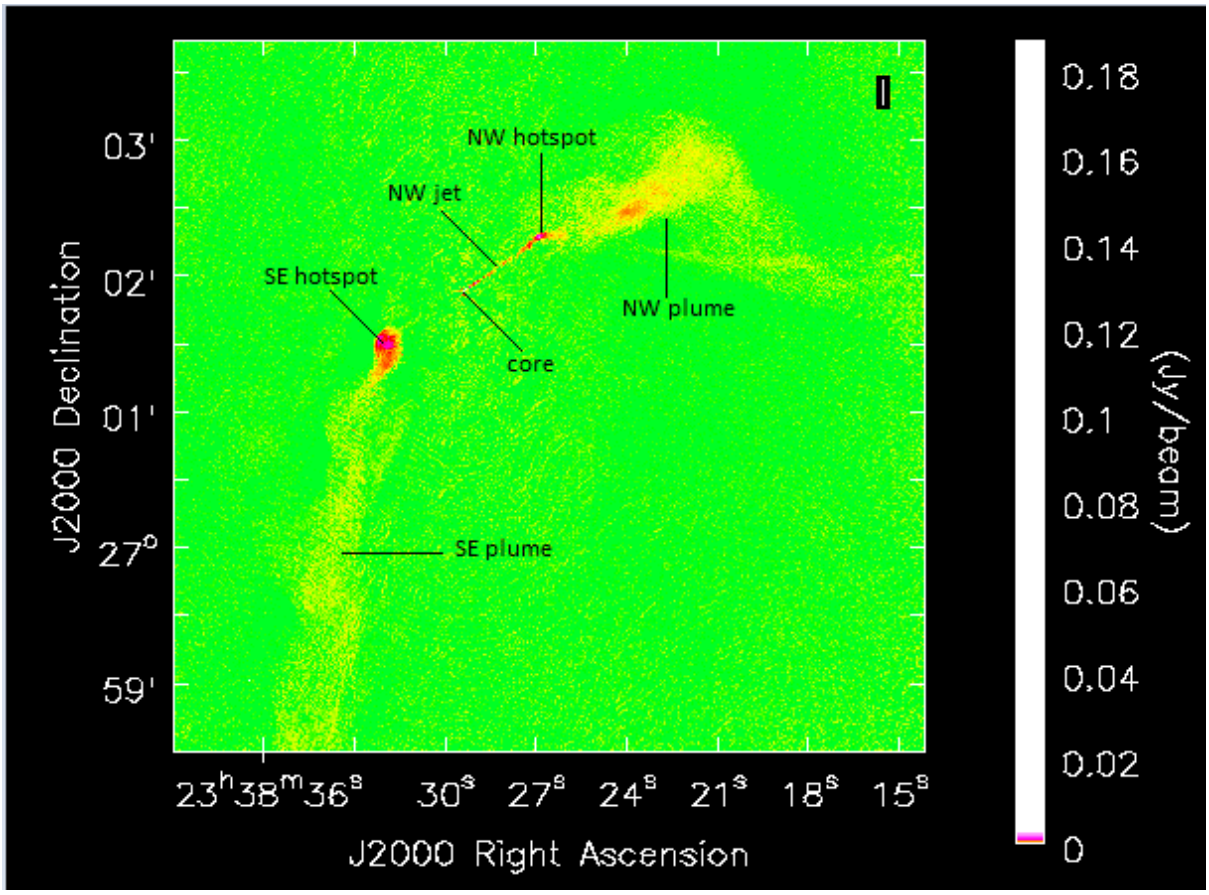

Figure 14: 1.5 GHz combined e-MERLIN plus VLA map at 0.39x0.37" resolution. Note the continued collimated outflow from the NW hotspot into the base of the NW plume.

3.3 The radio core

A few percent of mJy radio sources are known to exhibit variability on timescale of years (e.g., Oort & Windhorst, 1985). However, there was no observed variability of the radio core of 3C465 over the time-scales of the VLA observations at 1.5 or 8.5 GHz and/or e-MERLIN observations at 1.5 GHz, within the errors imposed by the uncertainty of absolute flux calibration at either the VLA or e-MERLIN array. Its flux density measured from the two interferometers and at the two frequencies (and in the case of the VLA, the two configurations deployed in our observations) is reported in Table 6 below. The best position for the core is RA 23:38:29:39, Dec 27:01:53:25.

3.4 Jets, knots, hotspots and plumes

Our low-resolution maps (Fig. 11) show the peaked central emission and the elongation of the overall radio structure in the NW-SE direction, consistent with the characteristic U or C-shaped morphology exhibited by these class of radio sources due to ram pressure arising from bulk motion of the host galaxy relative to the cluster. The total angular extent of 3C465 estimated from our 1.37x1.13" resolution 1.5 GHz VLA map is 7.60 arcmin. This corresponds to a projected angular size of 456 arcsec (~ 275 kpc) – about a factor 1.3 lower than that measured by Leahy et al. (1996) at similar frequency but different configurations (A & C) of the VLA. Sensitivity to extended structures at C-configuration of the VLA is comparatively higher than B-configuration at similar frequencies and this accounts for the difference in our observed angular size of the radio source. Our radio image shows two very narrow, well collimated jets (denoted NW and SE) emanating from the core of the galaxy, with the jet moving in our line of sight (NW jet) exhibiting considerably higher surface brightness over almost its full length compared with the counterjet (SE jet). Our e-MERLIN only image (Fig. 12) represents the highest resolution map of 3C465 to date, and with the short baseline contribution from the VLA in our combined e-MERLIN/VLA map (Fig. 14) we further construct the highest resolution and sensitivity map of the source. In our high resolution map (Fig. 12), the counterjet is not visible and is seen as a one-sided jet – a feature which 3C465 shares in common with classical double (FR II) radio sources.

The NW jet is well resolved and has a cross-sectional width of ~0.32 arcsec. At high resolution, there is clear evidence of a knotty structure at the base of the NW jet of 3C465 – a feature observed earlier by Hardcastle & Sakelliou (2004). However at e-MERLIN resolution (see Fig. 13) our good image fidelity allows us to infer multiple bright knotty structures – two of which are visible at the very edge of the core, the very point where the jet is first seen emanating from the central engine, and a third knot which lies between the two knots denoted NJ1 by Hardcastle

& Sakelliou (2004). Beyond 4.4 kpc from the inner jet, there is no clear evidence of such knotty structures of intense radio emission until the main site of energy dissipation in the bright compact region (hotspot) denoted NW hotspot near the base of the NW plume (Fig. 14). This termination point is ~23.4 kpc from the core and corresponds to the termination point of the NW jet. The SE hotspot exhibits a relatively broad bright structure compared with the NW hotspot. Since both jets must carry power of equal magnitude (for momentum conservation), it is difficult to assign a physical interpretation to this striking asymmetry between the two hotspot regions – which rather appears characteristic for archetypes of this class of radio galaxies [see Hardcastle & Sakelliou, (2004) for similar asymmetry in a sample of 7 WAT sources including 3C465]. A plausible explanation however could be the degree of jet-environment interactions at the two sites – with what appears to be a "mini" overpressured cocoon at the SE hotspot region resulting from a relatively higher density environment in pressure equilibrium with the ICM.

From the termination point of the NW jet (~29.8 kpc), the NW plume is observed to extend in the jet direction (northwestwards). However, after a distance of ~39.1 kpc from its base, the rapid change in direction is particularly obvious. There are two pronounced bends, at almost 90^{o} – first, southwestwards and then westwards, and the jet appears to bend once more in the northwest direction at ~90^{o} towards the tail end of the NW plume to form a bell shape. Within the limitations of sensitivity to large-scale structures in our observations, we argue that this bending trajectory (northwest – southwest – northwest) implied by the NW plume could be episodic, stretching over several tens – hundreds of kpc into the IGM. The rather striking feature here is the apparent asymmetry in morphology of the two plumes. Unlike the NW plume, the SE plume shows no prominent bends except for a wiggled pattern downstream. Since the plumes in WAT sources are generally thought to be analogous to smoke from factory chimneys (i.e., light slow-moving structures strongly affected by bulk motions in their

environments), these wiggles are likely the result of strong interaction between the large-scale flow within the plume (which must be light compared with the external medium) and features of the external environment due to either thermal or ram pressure. We attribute the observed asymmetry in physical size and structure of these two large scale components to 2-D projection effects such that the SE plume if projected in a different direction could exhibit similar prominent bends as the NW plume. The radio source fades into the noise on these images and, as noted above, the source is likely to be more extended than the estimated angular size quoted in our present analysis.

Table 7: Properties of radio maps presented

Map	Restoring beam			Core flux density (Jy)	Off-source noise (μJy)	RA (J2000)	DEC (J2000)	Figure Number
	Major axis (arcsec)	Minor axis (arcsec)	Pos. angle (°)					
$VLA^{L,A}$	1.41	1.13	68.54	0.20	30.39	23 38 29.39	+27 01 53.53	11
$VLA^{L,B}$	4.06	3.76	34.93	0.22	34.66	23 38 29.39	+27 01 53.53	11
$VLA^{L,AB}$	1.37	1.13	71.02	0.21	34.64	23 38 29.39	+27 01 53.53	11
$VLA^{L,AB}$	1.50	1.50	0.00	0.21	34.92	23 38 29.39	+27 01 53.53	15
$VLA^{X,ABCD}$	0.50	0.50	0.00	0.21	22.75	23 38 29.39	+27 01 53.53	15
$VLA^{X,ABCD}$	1.50	1.50	0.00	0.21	20.22	23 38 29.39	+27 01 53.53	15
$e\text{-}MERLIN^{L}$	0.27	0.15	19.26	0.21	31.05	23 38 29.39	+27 01 53.25	12
$e\text{-}MERLIN^{L}+VLA^{L,AB}$	0.39	0.37	108.24	0.17	33.66	23 38 29.39	+27 01 53.53	14
$e\text{-}MERLIN^{L}+VLA^{L,AB}$	0.50	0.50	0.00	0.19	31.43	23 38 29.39	+27 01 53.53	15

Notes: The superscripts L and X respectively denote ~1.5 GHz and ~8.5 GHz observing frequency deployed in our present study; A,B,C & D represent the array configuration of the VLA observations.

3.5 Jet speed and sidedness ratio

The good image fidelity of our maps allows us to estimate the jet/counterjet ratio in our sample and place constraints on the jet speed and angle to the line of sight in 3C465. Following the procedure defined by Hardcastle et al. (1998), and using our 1.5 GHz VLA map at 1.5" resolution, we measure only the straight part of the jet and counterjet, over equivalent angular extent – to avoid any discrepancy in the angle it makes with the line of sight over the integration region. We measure flux densities of 60.16 ± 0.66 mJy and 4.05 ± 0.14 mJy for the jet and

counterjet respectively, and obtain a sidedness ratio of 14.85 ± 0.80. Our estimated sidedness ratio is approximately a factor 3 higher than that obtained by Hardcastle and Sakelliou (2004) for this WAT jet at 8.5 GHz. Our obtained value is probably a better estimate of the sidedness ratio of the radio jet in 3C465 due to the improved bandwidth capabilities of the new EVLA deployed in our observations. We again assume that the jets are intrinsically symmetrical and that the observed jet flux asymmetries are due to relativistic beaming effects. This allow us to constrain the characteristic beaming speed, β_j and angle it makes with our line of sight, θ by defining the ratio of the jet and counterjet flux densities, $J_v = S_j / S_{cj}$, as;

$$J_v = \left(\frac{1+\beta_j \cos\theta}{1-\beta_j \cos\theta} \right)^{\delta} \qquad (11)$$

Where, $\beta_j c$ is the speed of the jet, which is inclined at an angle, $\theta \in [0, \pi/2]$ to our line of sight, and δ = m + α; the constant m = 2 for a continuous jet (see Scheuer & Readhead, 1979 for review). α is the spectral index, which is taken to be 0.6. By inverting equation (11) above, $\beta_j \cos\theta$ can be expressed in terms of J_v such that;

$$\beta_j \cos\theta = \left(\frac{J^{1/\delta} - 1}{J^{1/\delta} + 1} \right) \qquad (12)$$

Since $0 < \beta_j < 1$ and $0 < \cos\theta < 1$, this gives lower limits on both β_j and $\cos\theta$:

$$\beta_j > \left(\frac{J^{1/\delta} - 1}{J^{1/\delta} + 1} \right) \qquad (13)$$

$$\cos\theta > \left(\frac{J^{1/\delta} - 1}{J^{1/\delta} + 1} \right) \qquad (14)$$

The observed jet/counterjet asymmetry hints at a plausible beaming effect and thus favours relativistic speeds in the jet – at least in the regions close to the inner core. From our analysis,

we find that $\beta_j \cos\theta = 0.48$. Since a lower limit on $\cos\theta$ corresponds to an upper limit on θ, we have $\theta < \cos^{-1}(0.48)$. This yields lower and upper limit values of 0.5 and 61° for β_j and θ respectively. We find our estimated jet speed, v_j = 0.5*c* to be consistent with the range of values (0.3 – 0.7)*c* obtained by Jetha et al. (2006) in their study of jet speeds in a sample of 30 WAT radio galaxies including 3C465.

3.6 Spectral mapping, analysis and results

3.6.1 Resolution Matching

Our combined e-MERLIN/VLA map (hereinafter referred to as 1.5 GHz map) has a higher resolution ~0.39x0.31" and can further be deconvolved to a beam size approximately equal to the e-MERLIN only beam size. However, it is impossible to obtain good image fidelity of the 8.5 GHz map at such high spatial resolutions. For accurate determination of spectral indices across the two frequencies, we needed to convolve the 1.5 and 8.5 GHz maps to equivalent resolutions. This was necessary to ensure that any recovered flux at both frequencies included emission extended on scales up to those consistent with the 8.5 GHz restoring beam. This allowed us to effectively measure flux densities from the same spatial region from each map. At higher resolutions we are less sensitive to extended emission of the source and vice versa, and this has been accounted for in our estimates of the spectral indices – with the 0.5" resolution map deployed for the jet and hotspot regions while the 1.5" resolution map has been used for the plumes. For consistency, spectral indices at the two resolutions were independently examined at the hotspot region, and this yielded values of -0.73 ± 0.01 and -0.75 ± 0.01 for the 0.5"(1.5") resolution respectively, showing that the two sets of maps are consistent. We have performed primary beam correction on the 8.5 GHz map. This allows us to measure precise flux densities and corresponding errors since the shortest baselines sampled by the two maps

are similar – so that we are sensitivity to the same extended structure (plumes) across the two frequencies.

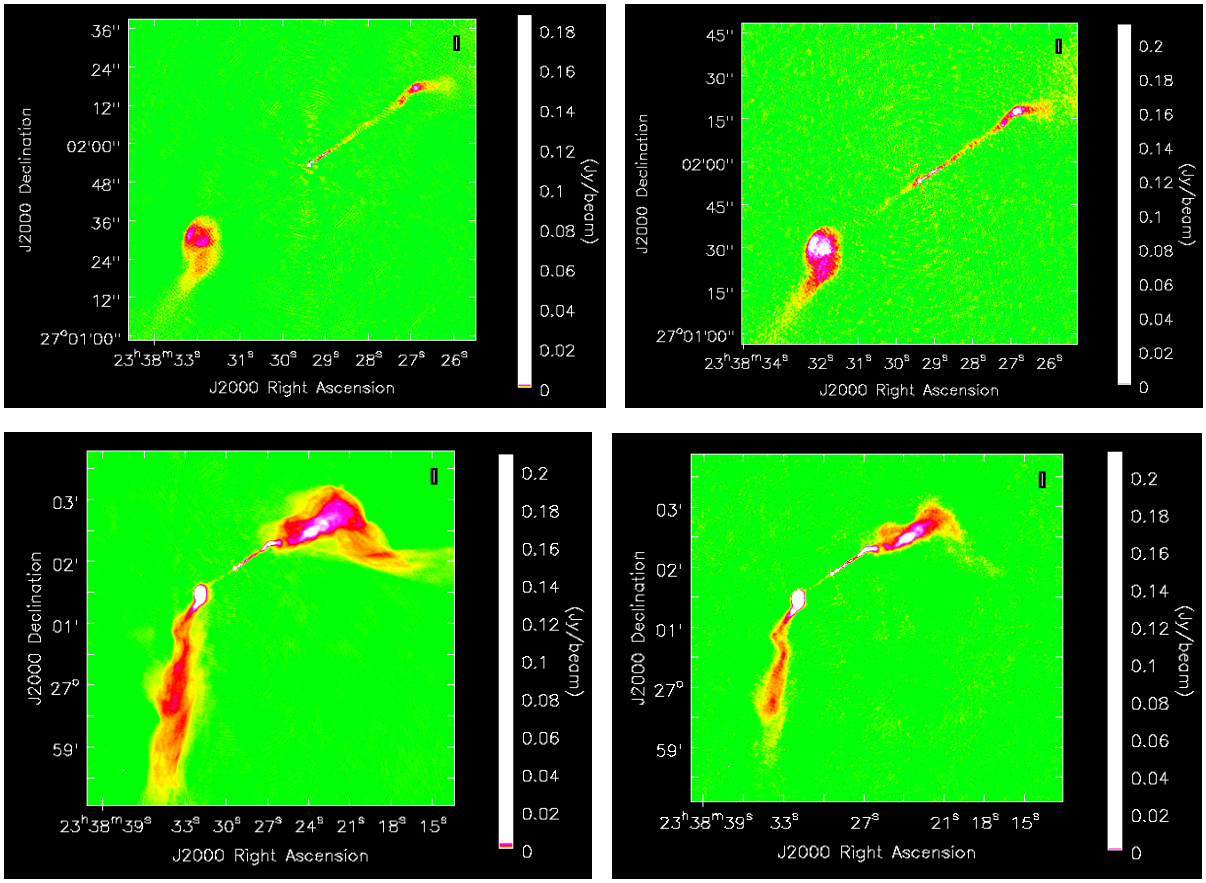

Figure 15: Matched resolutions across two frequencies for spectral studies in the WAT source 3C465. Top: 0.5" resolution maps used for flux density integration in the jet and hotspot regions. Left hand side – 1.5 GHz combined e-MERLIN plus VLA map; Right hand side – 8.5 GHz VLA map. Bottom: 1.5" resolution maps for flux density integration in the plumes. Left hand side – 1.5 GHz VLA map; Right hand side – 8.5 GHz VLA map (note the flux density break).

3.6.2 Spectral-index estimates and mapping

Since our data cover only two frequencies, we have directly calculated the spectral indices as: $\alpha_{v1}^{v2} = \ln\left[S(v1)/S(v2)\right]/\ln(v1/v2)$, by constructing polygonal regions for flux density measurements within the convolved equivalent maps. Where necessary we used polygons slightly wider than regions of *real* emission to reduce sensitivity to any residual misalignments between the maps. Background was taken from the rms errors in total intensity *I* from circle of

radius 10.96 arcsec fixed in position. Since the rms error just depends on the ratio $\nu 1/\nu 2$, by standard error propagation we can estimate fractional errors in α across the two frequencies as:

$$\sigma_{\alpha} = \frac{\sigma_I / R}{\ln(\nu 1/\nu 2)} \qquad (15)$$

Where σ_I is the fractional error on the ratio of the two flux densities and R is the ratio of the two flux densities itself – the error of which depends on the error (noise levels) on the maps, and $\nu 1$ and $\nu 2$ are frequencies corresponding to the L-Band (~1.5 GHz) and X-Band (~8.5 GHz) respectively used in our present analysis.

We understand this is a relatively crude model in estimating the error on individual flux density values across the two frequencies. However if we adopt a similar noise level over different regions of flux density integration in our maps and assume that errors in I have a Gaussian distribution with zero mean and rms σ_I in the image plane and that they are independent on scales larger than the primary beam, then our errors should be robust. In constructing our spectral-index map we took background to be the off-source noise level σ_{off} in I and created the map at 3σ cut-off at this rms value over the two frequencies. Finally, due to the complex structure of our source, we have carefully estimated our distances taking into consideration the trajectory of the radio jet to account for the bending of the tail of the radio source through the IGM. All flux profile axes in our plots are logarithmic scales and except where explicitly stated, all distances are with respect to the central unresolved feature, coincident with the nucleus (core) of the host galaxy.

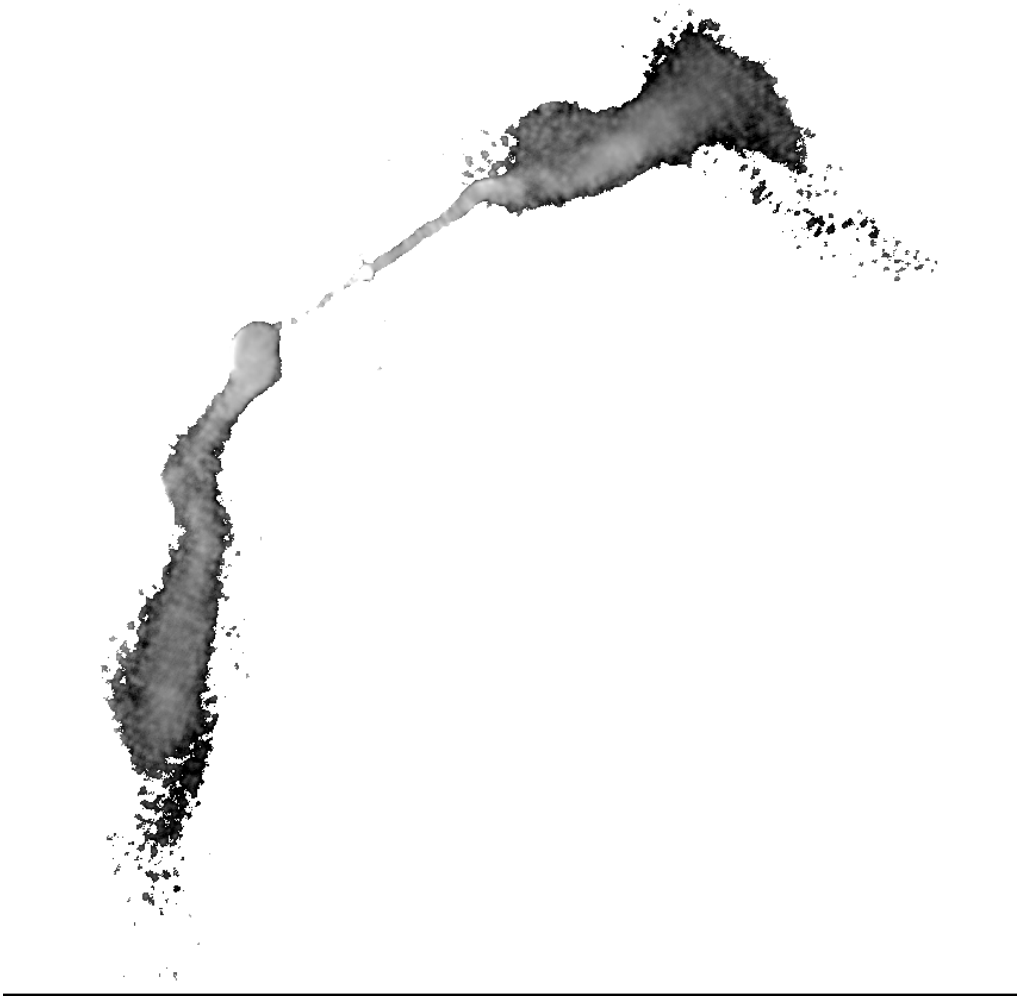

Figure 16: Map of spectral index, α, of the WAT radio source 3C465 constructed from maps made at two frequencies (~1.5 and ~8.5 GHz) at 1.5-arcsec resolution. α is in the range -0.5 to -0.8 and -1.1 to -2.3 over the jet and plume regions respectively and is plotted at 3σ rms noise cut-off in total intensity.

3.6.3 Flux density and spectral index distribution and properties

We observed *strong* correlation in the flux density distributions measured over the two frequencies along the jet, hotspots and plumes of our radio sample (see Fig. 17, 19 & 20). Figure 16 above shows a grey-scale image of the spectral index over the range $-0.3 \leq \alpha \leq -2.3$ for 3C465. With the exception of the unresolved core, which is partially optically thick with $\alpha \sim -0.4$, the emission typically has $-0.5 \leq \alpha \leq -0.8$ over the jet region and $-1.1 \leq \alpha \leq -2.3$ in the plumes. It is noteworthy that close to the edges of the jet, small errors in deconvolution can

cause significant changes in α (i.e., high or low spectral index values), and this is also true for regions where signal-to-noise ratio is low. The mean spectral index of the jet and counterjet (estimated from our spectral index map) is -0.70 ± 0.04 and as discussed in section 4.6.4 shows a fairly constant spectrum. However, the overall spectral index profile of the source is observed to steepen rapidly with distance from the AGN. This spectral behaviour is as expected in the standard model in which the radio tails flow slowly away from the host galaxy and eventually become dominated by the presence of old electron population (radiative ageing) resulting in steeper spectra away from the core – compare the spectral index map of the WAT source 3C130 by Hardcastle (1998). Distributions of flux densities and corresponding spectral indices in the entire sample are plotted and discussed further in the sections to follow.

A distinctive feature of our spectral index map (see Fig. 16) is the stretch of a long filament which leaves the NW hotspot and extends in the jet direction (northwest) into the base of the NW plume, possibly suggesting some continued collimated outflow of plasma into the large-scale structures and is observed to eventually terminate in a broad bright region in the NW plume. Although appealing, per Leahy (1993) definition, this site of intense emission does not meet the criteria to be described as a hotspot. A similar observation has been made earlier in the WAT source 3C130 by Hardcastle (1998), and more recently by Hardcastle & Sakelliou (2004) in their study of selected WAT samples in the Abell clusters of galaxies, and with such additional evidence we cautiously argue that this feature could well be a defining characteristic of these class of radio sources.

3.6.4 Spectral Profiles

3.6.4.1 The Jet and Knots

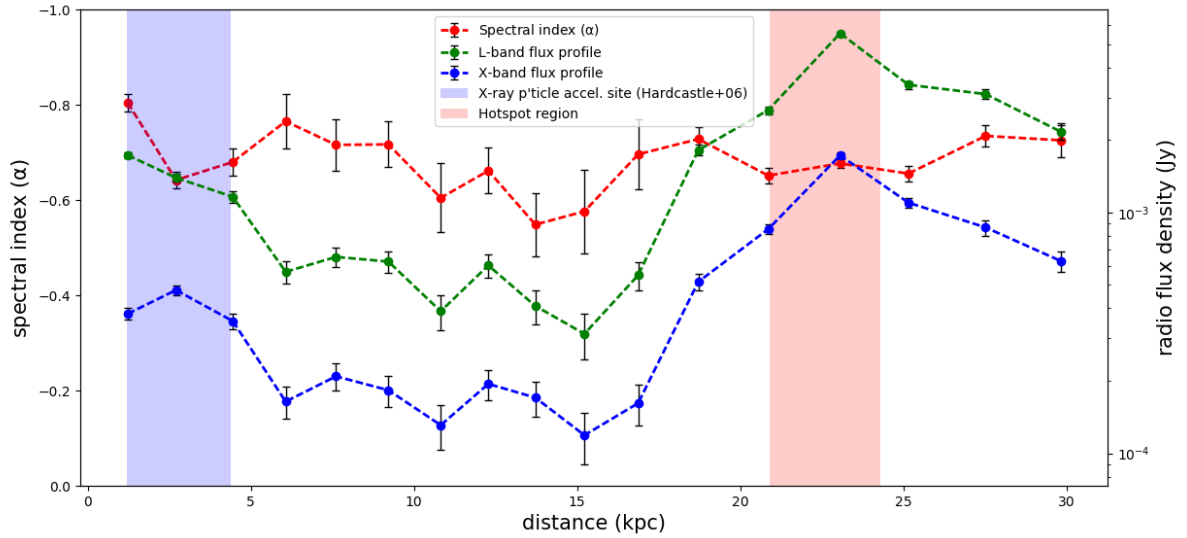

Figure 17: Profile of spectral index, α, along the NW jet axis as a function of distance from the galaxy central region. Also shown are the respective flux density distributions measured at 1.5 and 8.5 GHz. The error bars correspond to random errors σ_r from the rms errors in *I* only. Shown on the plot are also regions of interest (ROI) indicating site of X-ray particle acceleration as observed by Hardcastle et al. (2006) in a *Chandra* and *XXM-Newton* study of 3C465 – colour coded in blue tone; and the NW hotspot region – colour coded in red tone.

At 0.5" resolution, the counterjet in our map is not bright enough to be imaged well and so our analysis here is limited to the NW jet of the source. Individual integrated spectral indices at locations chosen throughout the jet are plotted in Figure 17. These show a fairly constant spectral profile over almost the entire jet length although there is some fractional steepening and flattening at a few discrete regions along the jet axis. Our estimate of ~29.8 kpc for the jet length is approximately a factor 2 higher than the termination length of the jet in 3C465 reported by Hardcastle & Sakelliou (2004). This arises from our inclusion of the trajectory in measuring distances along the jet to account for the bends in the radio source. There are considerably high error bars on the spectra from ~6–17 kpc; and noticeably so between ~10–17 kpc inclusive. This stretch corresponds to regions of considerable low surface brightness of

the radio jet as seen in our total intensity (0.5") resolution map and therefore the errors are large.

The comparatively constant distribution of the spectral profile of the jet spans over, $-0.5 \leq \alpha_{jet} \leq -0.8$ with an average value of, $\langle\alpha_{jet}\rangle = -0.70 \pm 0.04$, as expected from radio synchrotron which is the predominant emission mechanism in this WAT source. As shown in Figure 17, within the first 4.45 kpc of radius from the core, the 3 point region of interest (ROI) spectral indices are observed to flatten from -0.80 ± 0.02 to -0.64 ± 0.02 ($\Delta\alpha = -0.16$) and thereafter increase marginally to -0.68 ± 0.03 ($\Delta\alpha = -0.04$). The spectral flattening over this geometric area indicates the presence of high energetic (young) electron population; and provides evidence of ongoing particle acceleration at the jet base. This is consistent with the fact that X-ray evidence for particle acceleration is found at the base of the radio jet (within the knotty structures) (Hardcastle et al. 2006). The rather interesting observation here is that the region of flattest spectral index ($\alpha = -0.55 \pm 0.07$) at a distance of ~13.7 kpc does not correspond to either of the bright knots at the jet base or the compact region of intense radio emission (hotspot). Beyond 13.7 kpc, there is systematic steepening of the spectra from -0.55 ± 0.07 to -0.73 ± 0.04 until the bright compact region (hotspot). The spectrum over this 3 point region of intense radio emission is almost constant, with lower and upper limits of -0.65 ± 0.02 (-0.68 ± 0.01) respectively, and $\langle\alpha\rangle = -0.66 \pm 0.01$. We discuss spectra of the hotspots further in the next section.

3.6.4.2 The hotspots

Integrated spectral profiles over the two hotspot (NW and SE) regions separately and for the two combined are plotted in Figure 19. For reliability and purposes of direct comparison, we constructed a circle of diameter 16.05 arcsec centred on the two components and estimated the hotspot spectra over this area. Due to the relatively smooth transition of the NW jet into the

base of the NW plume, our estimate over this angular extent for the NW hotspot region may be overestimated by a factor of a few in our present analysis and the opposite is true for the SE hotspot region which features a comparatively broad bright structure. The spectral indices over the integration regions in the hotspots show very little dispersion between the two components with mean values of $<\alpha_{NWh}>$ = -0.69 ± 0.01 and $<\alpha_{SEh}>$ = -0.65 ± 0.01 ($<\Delta\alpha>$ = -0.04). This plausibly indicates that an electron population of the same age is injected at these sites – consistent with the two components being at equal termination distances (~23.4 kpc) on either side of the host galaxy.

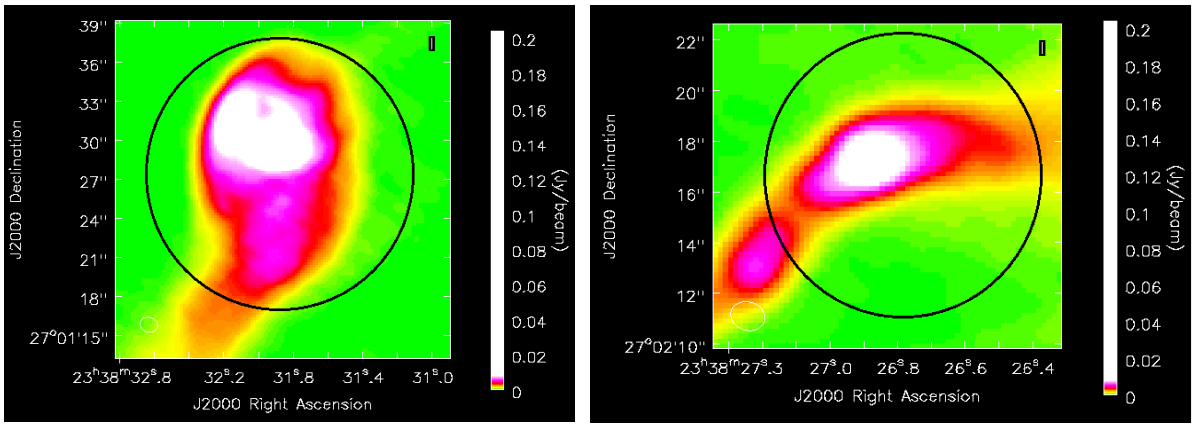

Figure 18: 1.5 GHz VLA maps (A+B-configuration) at 1.4x1.1" resolution showing the hotspots in the WAT source 3C465. Left: SE hotspot. Right: NW hotspot.

The NW hotspot spectrum (Fig. 19(a)) exhibits considerable flattening within the first 2 kpc radius from the edge of the hotspot integration region. This show the gradual decrease of α from -0.73 ± 0.01 to -0.61 ± 0.01 (Δα = -0.1). Beyond this span, the spectrum steepens to -0.77 ± 0.01 and thereafter falls gradually to -0.62 ± 0.01 at ~24.5 kpc, before experiencing a further upturn towards the end of the integration region. A slight but significant tendency for the spectral index to flatten over almost the entire SE hotspot geometric area is apparent from Figure 19(b), except for the final 3 points of integration at the tail end of the spectrum. The effect is subtle ($\Delta\alpha \leq -0.05$) nonetheless consistent; with a steady decline in α from -0.76 ± 0.01 to -0.57 ± 0.01 (Δα = -0.2), plausibly indicating acceleration of high energy cosmic rays as

would be expected in the case of typical classical double (FR II) radio galaxies. Unlike the SE, there is no clear trend in NW hotspot spectra and except for the first integration point, the spectra for the NW hotspot is slightly broader than the SE at all our fiducial locations; this is expected from the larger random errors in the NW hotspot due to its comparatively narrower distribution. Indeed from the standard model, if the spectrum is not a pure power-law and the jets are relativistic, then systematic variation between the observed spectra of the jet and counterjet are expected. Overall, the SE hotspot has a spectral index flatter than the NW hotspot, and we find no significant correlation between the spectral profiles of the two components over our geometric area of integrated flux density in the present analysis. Since these compact regions of intense radio emission, at least in FR IIs, are sites of AGN jet termination with consequent interaction with the lobe material (or plume material in the case of FR Is) forming strong shocks – to yield physical conditions required for particle acceleration (e.g., Massaglia, 2007); it is quite enticing to associate spectral flattening in the hotspots of our sample (which falls at the FR I/FR II break) with such sites of high energy particle acceleration – particularly at the SE hotspot which shows pronounced spectral flattening over almost the entire integration region in the present analysis.

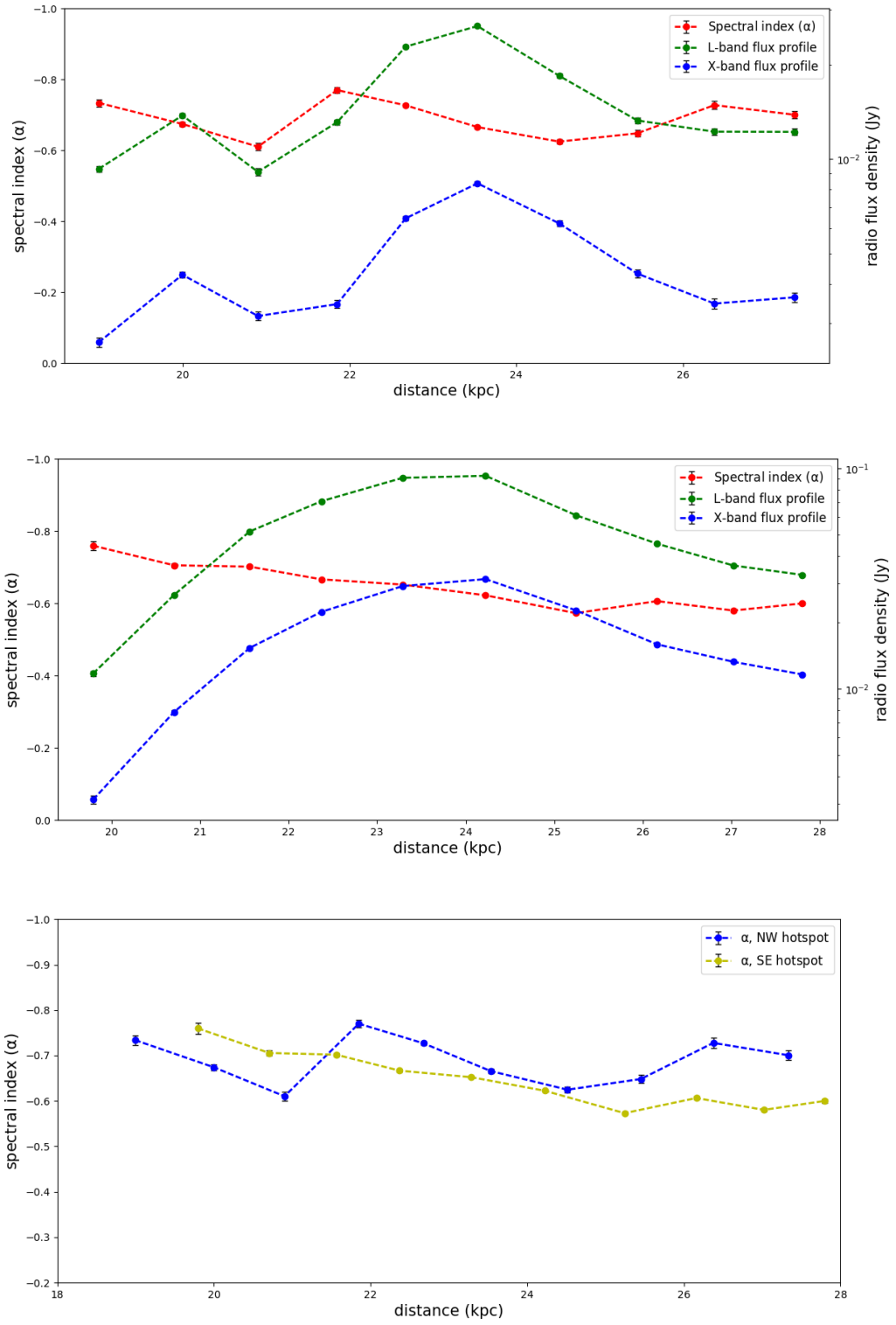

Figure 19: Distribution of spectral indices, $\alpha_{1.5}^{8.5}$ for the two hotspot regions plotted as a function of distance from the nucleus. Also shown are the respective flux density distributions. Top: NW hotspot. Middle: SE hotspot. Bottom: Composite plot of the two components. The spectral indices were calculated from total intensity integrated over a circle of diameter 16.05 arcsec centred on the two components; and error bars as in Figure 17.

3.6.4.3 The Plumes

We used 20 polygon slices each along the plumes for estimating the spectral indices in the large-scale components. The respective profiles are plotted in Figure 20 with their corresponding flux densities and errors. These show a systematic steepening of α in the NW plume compared with the practically constant distribution of α for the SE over the majority of the integration region. However, towards the tail end in both plumes there is an upturn in the spectral index from -1.60 ± 0.01 to -2.26 ± 0.05 ($\Delta\alpha$ = -0.66), and -1.37 ± 0.01 to -1.99 ± 0.03 ($\Delta\alpha$ = -0.62) for the NW and SE plumes respectively. The overall steepening of the spectra with increasing distance from the sites of particle injection in both plumes is consistent with synchrotron theory; and except for the final 3 locations at the tail end of each spectrum, there is no significant dispersion ($<\delta\alpha>$ = ± 0.01) between the SE and NW plumes. The mean difference between the NW and SE plume is $<\alpha_{NWp} - \alpha_{SEp}>$ = -0.05 ± 0.02. By this measure, the spectral steepening between the two large-scale components is not very significant; consistent with a constant spectral index change for both plumes. For reasons discussed in section 4.4 above, we have examined the spectral gradients of the NE plume in more detail. We have plotted profiles of spectral index in the plumes in two representations: as unaveraged slices across – (i) the whole plume, and (ii) inner region (which span an angular extent of ~61.5 arcsec) to show the level of variation on large and small scales respectively; and to compare α in the dip in this region with respect to the overall plume. The profile is as shown in Figure 20 (top pane). The clear tendency for the spectra to flatten slightly within the inner regions of the NW plume is confirmed; with the brightest spot in the region coinciding with comparatively the flattest spectra (α = -0.938 ± 0.002) – indicating the injection of young electron population into the base of the NW plume, and possible acceleration of particles at this site.

In general the spectrum of the NW plume is steeper $<\alpha_{NWp}>$ = -1.43 ± 0.01 compared with the SE $<\alpha_{SEp}>$ = -1.38 ± 0.01, and this is likely the consequence of variations in mass injection and

propagation in external pressure and density gradients in the two regions. Conventionally, as the radio jet breaks through the dense ICM and transitions into plumes the spectra will steepen further away from the AGN due to radiative ageing; and this is consistent with our observed spectral behaviour in the two components. It is interesting to note that Figure 20 shows a systematic pattern in the spectral distribution measured in both plumes. The two possibilities to this occurrence are; (1) the correlations result from residual calibration errors, or (2) there exist a similar trend in the spectral index evolution of the two plumes. Given our good image fidelity and robust estimate of the errors in *I*, we rule out option 1, and argue that both plumes probably have comparable spectral indices over the integration regions in our present analysis. This inference is again consistent with the conclusion that similar flow dynamics is at play in the two components with the observed asymmetry in total intensity a direct consequence of projection effects. Additional evidence for this conclusion can be drawn from the seemingly good agreement between the integrated spectral indices measured at the initial 8 locations of the SE plume and the spectral profile of the inner regions of the NW plume. Both show a bell-shaped spectrum within the first few kpc from the edge of the integration region marking the transition from jet to plumes, despite the absence of a distinct continued collimated outflow in the SE plume.

Overall our spectral profiles suggest that the plumes are approximately homologous structure, in the sense that there is a clear trend in their spectral distributions despite evidence of considerable local variations in physical size and structure. While the uncertainties are large near the tail end of the spectrum, there is evidence for a mild trend toward a steeper spectral indices with decreasing flux density in both plumes. We note that the spectral index limits in the respective components originate from the limiting flux density of the least-sensitive frequency (~8.5 GHz) in our two-point spectral index calculation.

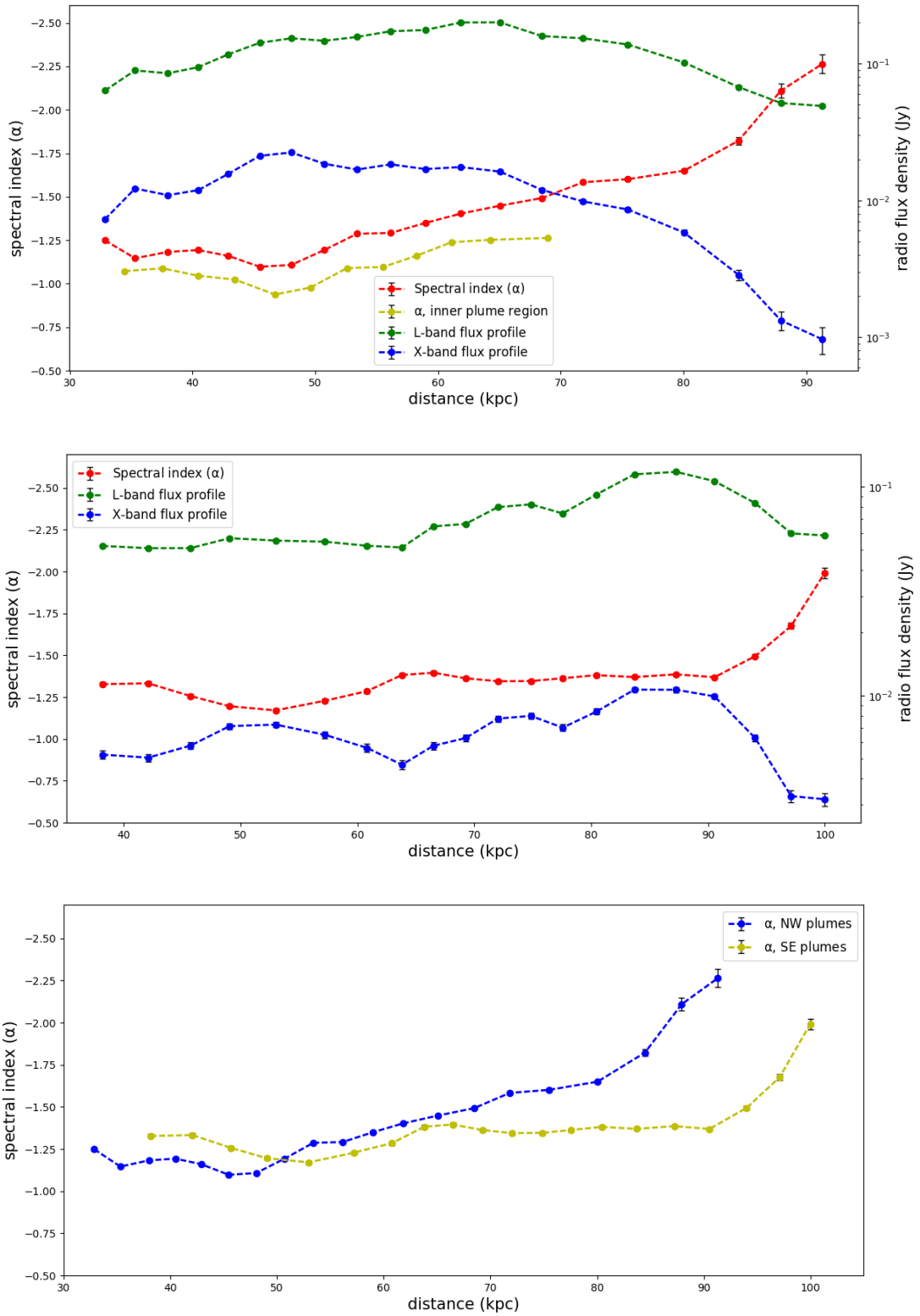

Figure 20: Variation in spectral indices $\alpha_{1.5}^{8.5}$ with fiducial distance in the extended structures of 3C465. Top: NW plume; also shown here is a profile of the continued collimated outflow at the base of the NW plume as seen in total intensity (Fig. 14). Middle: SE plume. Bottom: composite plot of the two components. Estimate of α and corresponding errors are as quoted in Fig. 17.

3.6.5 Constraints on particle acceleration in 3C465

It is well established that the evolution of radio jets is governed by the balance of particle acceleration and energy-loss processes (e.g., Laing et al. 2013). These energy losses affect the overall particle energy distribution in an ensemble of particles, and consequently the resulting synchrotron spectrum. For a power law distribution – i.e., an ensemble of homogeneous and isotropic population of electrons, $N(E,0)dE = N_0 E^{-\delta} dE$; there exist a corresponding power law synchrotron spectrum, $S(\nu) \propto V^{\alpha}$, the logarithmic slope of which relates the Mach number of the accelerating shock. For a detailed account on the subject, see Hardcastle (2013) and references therein. The case of astrophysical interest from standard model in which relativistic electrons suffer radiative and adiabatic losses as the radio jet propagate, is consistent with the spectral steepening we observe, away from the AGN. We note that relatively high frequency (~8.5 GHz) emission observed at large distances from the hotspots implies plausible in situ acceleration of relativistic particles in *at least* some parts of the extended structures. This again agrees with the observed spectral flattening at a few discrete locations in both plumes as seen in our spectral profile plots.

A good assessment of possible jet particle acceleration mechanisms is as discussed in section 1.4.3.1 above. Fermi acceleration is the most popular scheme; with first-order Fermi acceleration thought to be the main particle acceleration mechanism at collisionless MHD shocks (e.g., Laing et al 2013). Other acceleration mechanisms, the so called "second order" processes are generally thought to be less efficient, but as pointed out by Ostrowski & Schlickeiser (1993), the gradient of the relativistic particles in all cases approaches a power law at lower frequencies that reflects the acceleration physics. In the present study, we posit that acceleration is more likely distributed throughout the plumes of 3C465, rather than restricted to a few localised sites containing peak brightness, and that the observed variation in spectral profiles results from the combined effects of synchrotron and adiabatic (energy

transferred to surrounding medium only as work) losses, in addition to the underlying acceleration mechanism, as per discussions below.

i. Non-relativistic shocks

Contrary to earlier work (e.g., Bell, 1978) in test particle diffusive shock acceleration (test particle approximation), recent work (e.g., Laing et al. 2013) have established that steeper spectra can in principle be produced in weaker, non-relativistic shocks. Since our velocity estimate implies that the jet in 3C465 is mildly relativistic at the base, it is appropriate to assume non-relativistic flows/speeds in the extended structures due to deceleration resulting from entrainment by ambient material. Thus, the observed spectral steepening in the plumes is more likely the result of weak, non-relativistic shocks in the plume material.

ii. Mildly relativistic shocks

Previous studies (e.g., Summerlin & Baring, 2012) have shown that, depending on the nature of scattering, shock speed and field obliquity, mildly relativistic shocks can generate a wide range of power law slopes for the energy spectrum. Our observations indicate mildly relativistic speeds in the jet (at least in the inner regions close to the core) and thus require energy indices that depends on mean flow speed. Mildly relativistic speed upstream of the shock front seems the most likely scheme which meets this requirement. Thus, we argue that the observed synchrotron spectra in the jet of 3C465, and more so the spectral flattening in the inner regions close to the core (where the bright knots form), results from mildly relativistic shocks. We find our result to be consistent with earlier work by Laing et al. (2013) in which they suggested that mildly relativistic shocks are responsible for the range of physical conditions in FR I jet bases.

iii. Ultra-relativistic shocks

For outflows containing considerable amounts of non-relativistic protons entrained by ambient material, Laing & Bridle (2002b) suggests that the sound speed, β_s may be significantly lower

than the lower limit of 0.58 in the jet for an ultra-relativistic plasma, and may vary systematically with position in the jet. From our inferred mean value, $<\alpha_{jet}> = -0.70 \pm 0.04$, it is plausible that the jet composition in our sample is dominated by ultra-relativistic particles and magnetic field, and may be considerably higher or lower than this asymptotic value wherever the average flow speed is even slightly supersonic or transonic respectively.

Numerical (e.g., Ellison & Double, 2004) and analytical (e.g., Kirk et al. 2000) results have also shown that ultra-relativistic shocks in principle can produce a power law energy spectrum with $\delta = 2.23$ ($\alpha = 0.62$). Comparison with our observed mean α values of -0.69 ± 0.01 (-0.65 ± 0.01) for the NW and SE hotspots respectively suggests that both components have marginally but significantly steeper spectral indices than predictions from theory. Given this discrepancy and our constraints on the jet speed ($\beta_j \geq 0.5$), it seems rather unlikely that ultra-relativistic shocks are relevant to the physical conditions of these compact regions of intense radio emission. However, in the absence of independent statistical evidence, it is plausible that the flow at the hotspots is supersonic everywhere, suggesting strong *"relativistic"* shocks in this flow regime that can be modified by back-pressure of the accelerated cosmic rays. This in principle have the tendency to alter the shape of the synchrotron spectrum as seen in our respective hotspots spectral profiles.

3.6.5.1 Acceleration mechanisms

Our analysis shows that first-order Fermi process at mildly relativistic shocks are the most probable acceleration mechanism at play in 3C465 – evident in the observed synchrotron spectrum along the jet axis. Although we can favour this as the only mechanism, Laing et al. (2013) suggest a likely complication may exist, in the sense that, X-ray particle acceleration requires a distributed system of shocks covering a significant distance along the jet axis rather than restricted to a few localized shock sites. In the present study, such shock systems can be

associated with the multiple bright knotty structures at the jet base (Fig. 13), as well as the complex, non-axisymmetric brightness structure of the two hotspot regions (Fig. 18).

Since we infer mildly relativistic flow in our radio sample, we argue that two distinct acceleration mechanisms exists at the base of the radio jet.

1. The first mechanism is governed by flow speeds, $\beta_j \geq 0.5$, and seems the likely dominant acceleration process in the jet base – inferred from our lower limit of 0.5 for β_j. Since knots and hotspots are approximately homologous structures, it is plausible, particularly in the high-emissivity regimes (hotspots) for strong relativistic shocks to occur. These shocks have the tendency to accelerate electrons to high Lorentz factors, allowing X-ray synchrotron emission in the hotspot regions comparable to that observed by Hardcastle et al. (2006) in the bright knots at the jet base.
2. The second mechanism dominates wherever the flow speed, β_j falls below ≈ 0.5. In this regime, there is deceleration by entrainment such that the flow is transonic and dominated by weaker shocks. As pointed out by Rieger & Duffy (2004), steady shear acceleration bracket this condition, and implies that transverse velocity gradients must exist in these regions. In addition to the jet base, we favour this scheme as the likely dominant process at play in the extended structures (radio plumes) of our sample, particularly as β_j approaches a limiting value ($\ll 0.5$) – implying non-relativistic flows/shocks in this regime.

We infer evidence for particle acceleration in the plumes based on the observed continued collimated outflow of plasma from the site of particle injection (hotspots) into the plume materials. This compare with predictions from twin-beam model for radio sources (e.g., Blandford & Rees, 1974), and as noted by Blandford & Eichler (1987), these high energy electron population, which are responsible for emission at such large distances must have been

accelerated *in situ*, most likely via weaker/non-relativistic shock acceleration as seen in the present study.

Overall, we infer two different acceleration mechanisms at the base of the radio jet in our sample, consistent with previous high resolution multi-waveband (radio to X-ray) studies of FRI jet bases (e.g., Hardcastle et al. 2003; Perlman et al. 2011). These two mechanisms similarly account for the acceleration process in the hotspots and plumes, although in the case of the hotspots, there is a slight tendency that the required speed will be significantly higher than our asymptotic value of 0.5 in the present analysis. The systematic difference in the observed spectral profiles for the three regions (jet, hotspots and plumes) relates these distinct mechanisms. We note that by this conclusion, we are by no means neglecting the likelihood of second-order Fermi acceleration as possible alternative mechanism.

CHAPTER 4

The NAT source 3C83.1B

4.0 3C83.1B

The present chapter is an extension to our previous work in resolving the physics driving the observed jet structure in powerful radio galaxies, as part of the extragalactic jet legacy project with e-MERLIN. As the e-MERLIN data have not yet been reduced, only the EVLA data for this source are presented here.

4.1 The radio source

The NAT source 3C83.1B is associated with the elliptical galaxy NGC1265 in the Perseus cluster of galaxies. It is the archetype of this class of radio sources and has twin bent-double radio jets characteristic of FR I radio galaxies. The tails of 3C83.1B and NAT sources in general are thought to be bent by the ram pressure exerted by the external gas due to motion of the host galaxy relative to the cluster, producing the characteristic U shape, and as noted by Stocke & Burns (1987), merge with the more extended tails after significant bending. Previous studies in the optical (e.g., O'Dea et al. 1986), radio (e.g., O'Dea & Owen, 1986; Xu et al. 1999), and X-ray (e.g., Sun et al. 2005) observations of the source have been made. However, unlike 3C465, there exist limited detailed literature on the dynamics and kinematics of its radio structures (jets, hotspots and plumes). Early studies by Bertola & Perola, (1973) based on deep photographs taken with the 48-in Palomar Schmidt telescope suggested that the host galaxy structure has an extended halo that can be traced out to a maximum distance of 100 arcsec from the galactic centre. In spite of the rich environments where these sources live, the comparatively high velocity (~2170 km/s) with which 3C83.1B moves through the IGM (e.g., Pfrommer & Jones, 2002) is not unreasonable, and Jaffe & Perola (1973) have used dynamical models to establish this.

4.2 Radio maps

Below are total intensity maps of the radio source 3C83.1B from deconvolution of our VLA observations. The radio maps here shows the characteristic bent-double radio tails arising from ram pressure due to motion of the host galaxy relative to the cluster. The overall angular extent of the radio source, estimated from our 1.4x1.3" resolution 1.5 GHz VLA map is 4.13x2.41 arcminutes. We note that the large scale structures of 3C83.1B extends much further into the IGM than is visible in our maps. Detailed imaging of our e-MERLIN observations, and description of the radio maps of 3C83.1B and corresponding analysis will be presented elsewhere (Bempong-Manful & Hardcastle, in progress).

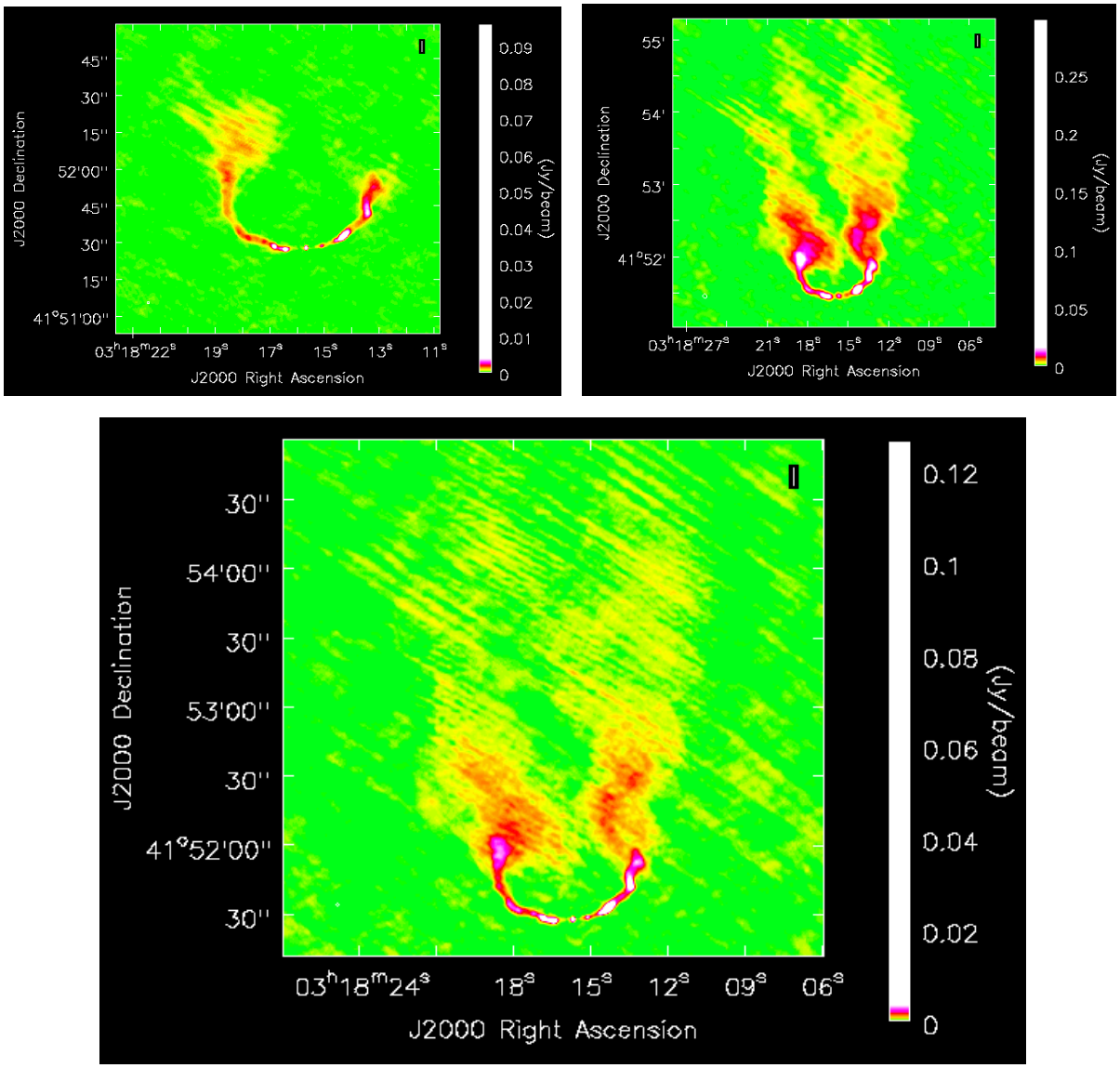

Figure 21: 1.5 GHz VLA maps of 3C83.1B. Top left: A-configuration at 1.1×1.0" resolution. Top right: B-configuration at 4.1×3.7" resolution. Bottom: AB-configuration at 1.4x1.3" resolution.

Table 8: Properties of radio maps presented

Map	Restoring beam			Core flux density (Jy)	Off-source noise (μJy)	RA (J2000)	DEC (J2000)	Figure Number
	Major axis (arcsec)	Minor axis (arcsec)	Pos. angle (°)					
$VLA^{L,A}$	1.09	0.99	-22.47	0.01	56.86	03 19 48.15	+41 30 41.13	21
$VLA^{L,B}$	4.09	3.66	34.05	0.01	60.44	03 19 48.15	+41 30 41.13	21
$VLA^{L,AB}$	1.43	1.32	-17.20	0.01	58.62	03 19 48.15	+41 30 41.13	21

Notes: The superscripts are as indicated in Table 7.

CHAPTER 5

Conclusion and Future Work

5.1 Conclusion

We have presented the highest resolution and sensitivity maps of the WAT source 3C465 jet, derived by combining radio data from e-MERLIN and VLA observations. Total intensity maps and spectral index maps of the whole source derived from two frequencies at 1.5 arcsec resolution is also presented. A comprehensive description of these maps and detailed spectral analysis to study the plausible underlying mechanisms of where and how particles are accelerated in the jet, knots, hotspots and plumes of the radio source have also been presented. Unlike the main jet, the counterjet is not bright enough to be imaged well and derive reliable α at the 0.5 arcsec resolution used in the present analysis. Radio images of the NAT source 3C83.1B from our VLA observations are also presented, and this show the characteristic U shape of these class of radio sources which results from ram pressure due to motion of the host galaxy relative to the cluster. A comprehensive discussion of the radio structure and spectral index distribution of this source will be given elsewhere (Bempong-Manful & Hardcastle, in progress).

5.2 Summary of results

a) We observed no variability of the radio core of 3C465 over the time-scales of the respective observations in the present study.

b) Our radio maps show the peaked central emission and the elongation of the overall radio structure of 3C465 in the NW-SE direction, consistent with the characteristic U or C-shaped morphology exhibited by these class of radio sources due to ram pressure arising from bulk motion of the host galaxy relative the cluster. The total angular extent of 3C465 estimated from our 1.37x1.13" resolution 1.5 GHz VLA map is 7.60 arcmin.

This corresponds to a projected angular size of 456 arcsec (~ 275 kpc) – a factor 1.3 lower than that measured by Leahy, Bridle & Strom at similar frequency but different configurations (A & C) of the VLA.

c) Our e-MERLIN only (Fig. 12) represents the best *deep transverse-resolved radio observations* of 3C465 to date, and with short baseline contribution from the VLA in our combined e-MERLIN/VLA map (Fig. 14) we further construct the highest resolution and sensitivity map of the source; although the jet in this map is seen as one-sided due to the small number of antennas in the e-MERLIN array.

d) Compared with observations by Hardcastle & Sakelliou (2004), our high resolution map shows clear evidence of multiple bright knotty structures at the base of the NW jet of 3C465. The termination length of the jet ~29.8 kpc from the core, is a factor ~2 higher than the termination length reported by Hardcastle & Sakelliou (2004). We propose variation in density environments in pressure equilibrium with the ICM to account for the observed asymmetry in the two hotspot regions, whereas the striking asymmetry in morphology of the two plumes is most likely the consequence of 2-D projection effects.

e) We follow the procedure described by Hardcastle et al. (1998) and calculate a sidedness ratio of 14.85. From our analysis, we estimate lower and upper limit values of 0.5*c* and 61^{o} for the jet speed, β_j and angle to the line of sight, θ respectively. These values are reasonable and consistent with previous works (e.g., Jetha et al. 2006).

f) Our spectral index map have a range of indices, $-0.3 \leq \alpha \leq -2.3$; and except for the unresolved core which is partially optically thick with $\alpha \sim -0.4$, the emission typically has $-0.5 \leq \alpha \leq -0.8$ over the jet region and $-1.1 \leq \alpha \leq -2.3$ in the plumes. The apparent continued collimated outflow of plasma into the large-scale structures inferred from the long filament extending from the NW hotspot into the base of the NW plume is rather

striking. However, a similar observation by Hardcastle (1998) in the WAT source 3C130, and more recently by Hardcastle & Sakelliou (2004) in a selected sample of WAT sources in the Abell clusters of galaxies, form the basis of our conclusion that this feature could well be a defining characteristic of these class of radio sources.

Our analysis of the distribution of flux densities, and corresponding spectral indices, is consistent with the radio source hosting an AGN as expected, and is equally clearly dominated by synchrotron radio emission. The jet and hotspots have spectral indices flatter than the material (plumes) into which they flow. This is as expected from the standard model in which the spectrum is observed to steepen at large distances away from the sites of particle injection (nuclei and hotspots) due to synchrotron ageing. The principal results from our detailed study of the spectral index distribution in the WAT source 3C465 are as follows:

i. The spectral profile is fairly constant over almost the entire jet length with a mean value of, $<\alpha_{jet}> = -0.7 \pm 0.04$, as expected from radio synchrotron emission.
ii. The spectral flattening within the first 4.42 kpc radius from the core coincides with the region hosting the bright knots, and is consistent with the site of X-ray particle acceleration at the base of the radio jet observed by Hardcastle et al. (2006).
iii. The spectral indices in the hotspot regions show very little dispersion between the two components with mean values of $<\alpha_{NWh}> = -0.69 \pm 0.01$ and $<\alpha_{SEh}> = -0.65 \pm 0.01$ ($<\Delta\alpha> = -0.04$), indicating plausibly electron population of the same age is injected at these sites.
iv. Our spectral profiles suggest that the plumes are approximately homologous structures, in the sense that there is a clear trend in their spectral distributions despite evidence of considerable local variations in physical size and structure. We associate this asymmetry in morphology to variations in mass injection and propagation in external pressure and density gradients in the two regions, and this accounts for the

comparatively steeper spectrum in the NW plume, $<\alpha_{NWp}>$ = -1.43 ± 0.01 compared with the SE plume, $<\alpha_{SEp}>$ = -1.38 ± 0.01. There is also a clear tendency for the spectra to flatten slightly within the inner regions of the NW plume – indicating the injection of young electron population into the base of the NW plume, and plausible acceleration of particles at this site.

v. Our analysis shows that first-order Fermi process at mildly relativistic shocks is the most probable acceleration mechanism at play in the radio source 3C465. Consistent with earlier work by Laing et al. (2013), we infer two acceleration mechanisms; (a) when bulk flow speeds, $\beta_j \geq 0.5$, and (b) when flow speeds, β_j are less than ≈ 0.5. The first case can accelerate electrons to high Lorentz factors, whereas the second scenario must occur at slower speeds and larger distances.

5.3 Future work

As next step, we aim to construct total intensity maps of our e-MERLIN observations for 3C83.1B, and similar to 3C465, combine the two datasets (e-MERLIN and VLA) to construct the highest resolution and sensitivity map of the source to date. Once imaged, these observations will allow us to investigate in similar detail the radio spectrum of 3C83.1B. These results will then provide a unique opportunity to statistically compare the synchrotron spectra in the two samples (3C83.1B and 3C465) and check for any discrepancy.

Although these two results will address the nature of jet particle acceleration in the present study, there still remain open problems in the physics of particle acceleration. Of astrophysical interest are the so called *deviations from power law spectra* which are indicators of synchrotron ageing and plausible diagnostics of the acceleration mechanism. This curvature in spectral studies can potentially be mitigated by observing over a broad range of frequencies. It will therefore be of interest to conduct a comprehensive study of the particle acceleration in our

present sample by obtaining further observations (EVLA and e-MERLIN) over a wide frequency range. Also, the ability of LOFAR to provide observations at low (~MHz) frequencies presents a unique opportunity to investigate the spectral profiles at a level of detail never before achieved. Thus, we aim to complement our observations with LOFAR observations to further increase our understanding of the synchrotron spectra in these sources, and place greater constraints on where and how particles are accelerated in the jets, hotspots and plumes of NAT and WAT radio galaxies. These broad range of frequency coverage will also allow us to perform spectral ageing analysis of the sample using BRATS (Harwood et al. 2013).

Also, key to fully addressing the research questions of the present study is knowledge of the magnetic field structures immediately surrounding these jets. Clearly, the observed *strong* synchrotron radio emission from our sample illustrate the presence of intergalactic magnetic field. Thus, as an extension of this work, we will construct polarization intensity maps of our sample to investigate the orientation and degree of ordering of magnetic field in the jet base of the radio sources. This will further reinforce our understanding of the underlying physics driving the evolution of the radio jets in these powerful FR I sources.

References

Ables, J.G. (1974). Maximum entropy spectral analysis. A&A, Vol. 15, pp.383-393.

Abraham, R.G., Nair, P., McCarthy, P.J., et al. (2007). Astrophys. J., 669, 184.

Alfvén, H. (1942). Existence of electromagnetic-hydrodynamic waves. Nature, Vol.150, 405-406. doi:10.1038/150405d0.

Antonucci, R.J. (1993). Unified models for active galactic nuclei and quasars. Annual review of A&A, Vol.31, pp.473-521.

Argo, M.K. (2015). The e-MERLIN Data Reduction Pipeline. Journal of Open Research Software, 3: e2, doi:10.5334/jors.bp

Athreya, R. (2009). Astrophys. J., Vol. 696, pp.885

Aversa, R., Lapi, A., de Zotti, G., Shankar, F. and Danese, L. (2015). Black hole and galaxy coevolution from continuity equation and abundance matching. Astrophys. J., Vol. 810, pp.74

Baade, W. and Minkowski, R. (1954). On the identification of radio sources. Astrophys. J., 119, 215.

Baan, W.A., Fridman, P.A. and Millenaar, R.P. (2004). Astophys., J., Vol. 128, pp.933

Bahcall, J.N., Basu, S. and Kumar. P. (1997). Localized Helioseismic Constraints on Solar Structures. Astrophys. J., 485: L91–L94.

Baldi, R.D., Capetti, A. and Giovannini, G. (2016). The new class of FR 0 radio galaxies. Astron. Nachr., 337: 114–119. doi:10.1002/asna.201512275.

Bassani, L., Dadina, M., Maiolino, R. et al. (1999). A Three-dimensional Diagnostic Diagram for Seyfert 2 Galaxies: Probing X-Ray Absorption and Compton Thickness. Astrophys. J., V.121, p.473

Baum, S.A., O'Dea, C.P., Murphy, D.W. and de Bruyn, A.G. (1990). A&A, Vol.232, pp.19.

Benson, A.J., Bower, R.G., Frenk, C.S., Lacey, C.G., Baugh, C.M. and Cole, S. (2003). What Shapes the Luminosity Function of Galaxies? Astrophys. J., Vol.599, pp.38-49

Bertola, F. and Perola, G.C. (1973). Peculiar morphology of the outer regions of NGC 1265 (3C 83.1 B) and NGC 7720 (3C 465). Astrophysical Letters, Vol. 14, pp. 7-10.

Best, P.N. and Heckman, T.M. (2012). MNRAS, Vol. 421, pp.1569

Bianchi, S., Maiolino, R. and Risaliti, G. (2012). AGN Obscuration and the Unified Model. Advances in Astronomy, Vol. 2012. doi:10.1155/2012/782030.

Bicknell, G.V. (1994). Astrophys. J., Vol. 422, pp.542

Bicknell, G.V. and Begelman M.C. (1996). Astrophys. J., 467, 597.

Bicknell, G.V. (2001). The Snake: A Reconnecting Coil in a Twisted Magnetic Flux Tube. Astrophys. J., 548:L69-L72

Biggs, A.D. and Ivison, R.J. (2008). High-resolution radio observations of submillimetre galaxies. MNRAS, 385, 893–904. doi:10.1111/j.1365-2966.2008.12869.x

Bird, J. and Martini, P. (2008). The Lifetime of FR II sources in groups and clusters: Implications for radio-mode feedback. Astrophys. J., Vol.676, pp.147–162.

Birk, G.T. and Lesch, H. (200). The X-Ray Emission of the Centaurus A Jet. Astrophys. J., Vol.530, pp.L77-L79

Birzan, L., McNamara, B.R., Nulsen, P.E.J., Carilli, C.L. and Wise, M.W. (2008). Astrophys. J., 686, 859.

Bisnovatyi-Kogan, G.S. (2005). Very long-wave electromagnetic radiation from jets. Mem. S.A.It. Vol. 76, 122.

Blandford, R.D. (2001). Black Holes and Relativistic Jets. Progress of Theoretical Physics Supplement, 143, 182–201. doi:10.1143/PTPS.143.182

Blandford, R.D. and Eichler, D. (1987). Particle acceleration at astrophysical shocks: A theory of cosmic ray origin. Elsevier, Vol. 154, pp.1-75.

Blandford, R.D. and Payne, D.G. (1982). Hydromagnetic flows from accretion discs and the production of radio jets. MNRAS, Vol. 199, 883-903.

Blanton, M., Cen, R., Ostriker, J.P. and Strauss, M.A. (2000). Time Evolution of Galaxy Formation and Bias in Cosmological Simulations. Astrophys. J., 531:1-16.

Bodo, G., Ferrari, A., Massaglia, S., Rosner, R. and Vaiana, G.S. (1985). Astrophys. J., Vol. 291, pp.798 805.

Bondi, H. (1952). On Spherically Symmetrical Accretion. MNRAS, 112, 195.
Bourdin, H., and Mazzotta, P. (2008). A&A, Vol. 479, pp.307
Bridle, A.H., Hough, D.H., Lonsdale, C.J., Burns, J.O. and Laing, R.A. (1994). Deep VLA imaging of twelve extended 3CR quasars. Astron. J., 108, 766–820. doi:10.1086/117112
Briggs F., Bell J.F. and Kesteven M.J. (2000). Astrophys. J., Vol. 120, pp.3351
Burns, J.O., Eilek, J.A. and Owen, F.N. (1982). What bends wide-angle tail radio sources? D.S. Heeschen & C.M. Wade (eds.), Extragalactic Radio Sources, Springer, 45-46.
Cackett, E.M. and Horne, K. (2006). Photoionized Hβ emission in NGC 5548: it breathes! MNRAS, Vol. 365, pp.1180-1190. doi:/10.1111/j.1365-2966.2005.09795.x
Camenzind, M. (2005). Relativistic Outflows from Active Galactic Nuclei. Mem. S.A.It. Vol. 76, p.98.
Capetti, A., Macchetto, F., Axon, D.J., Sparks, W.B. and Boksenberg, A. (1995). Hubble Space Telescope Imaging Polarimetry of the Inner Nuclear Region of NGC 1068. Astrophys. J., Vol. 452, pp.L87-L89.
Capetti, A., Axon, D.J., Macchetto, F.D., Marconi, A. and Winge, C. (1999). Astrophys. J., Vol.516, pp.187
Celotti, A. (2001). Blazar Physics and Demographics, ed. M.C. Urry, & P. Padovani, ASP, 227, 105
Clarke, D.A., Bridle, A.H. Burns, J.O., Perley, R.A. and Norman, M.L. (1992). Origin of the structures and polarization in the classical double 3C 219. Astrophys. J., Vol. 385, p. 173-187.
Clark, B.G. (1999). Coherence in Radio Astronomy. in: G.B. Taylor, C.L. Carilli, & R.A. Perley (eds.), ASP Conf. Ser. 180: Synthesis Imaging in Radio Astronomy II.
Clarke, D.A., Macdonald, N.R., Ramsey, J.P. and Richardson, M. (2008). Astrophysical Jets. La Physique au Canada, Vol. 64, No. 2.
Curtis, H.D. (1918). *Pub. Lick Obs.*, 13, 31.
Das, T.K. (1999). Modelling the Origin of Astrophysical Jets from Galactic and Extra-galactic Sources. arXiv:astro-ph/9906113
Dennett-Thorpe, J., Bridle, A.H., Laing, R.A. and Scheuer, P.A.G. (2008). Asymmetry of jets, lobe size and spectral index in radio galaxies and quasars. doi:/10.1046/j.1365-8711.1999.02234.x
Eichler, D. (1993). Magnetic Confinement of Jets. Astrophys. J., Vol.419, pp.111-116.
Erlund, M.C., Fabian, A.C., Blundell, K.M., Moss, C. and Ballantyne, D.R. (2007). MNRAS, Vol.379, pp.498
Fabian, A.C. (2012). Observational Evidence of AGN Feedback. Annual Review of Astronomy and Astrophysics. Vol. 50, pp.455-489. doi:10.1146/annurev-astro-081811-125521
Fabian A.C. and Rees M.J. (1995). MNRAS, Vol. 277, pp.L55-L58.
Falcke, H., Körding, E. and Markoff, S. (2004). A scheme to unify low-power accreting black holes-Jet dominated accretion flows and the radio/X-ray correlation. A&A, 414(3), 895-903.
Fanaroff, B.L. and Riley, J.M. (1974). The morphology of extragalactic radio sources of high and low luminosity. MNRAS, Vol. 167, p. 31P-36P.
Ferrarese, L. and Merritt, D. (2000). Astrophys. J., 539, L9
Fiore, F. et al. (2017). AGN wind scaling relations and the co-evolution of black holes and galaxies. Astronomy & Astrophysics manuscript no. evol˙20170126˙ref. ESO 2017.
Foster, J.M. (2010). Supersonic Jet and Shock Interactions in the Laboratory. Bulletin of the American Astronomical Society, Vol. 41, p. 849.
Ghisellini, G., Padovani, P., Celotti, A. and Maraschi, L. (1992). Relativistic bulk motion in active galactic nuclei. Astrophysical Journal, Vol. 407, No. 1, p. 65-82.
Godfrey, L.E.H., Lovell, J.E.J., Burke-Spolaor, S., et al. (2012). Periodic Structure in the Megaparsec Scale Jet of PKS 0637−752. Astrophys. J., 758:L27.
Goodger J.L., et al., (2010). Astrophys. J., 708, 675
Goodrich, R.W. (2001). Unification of AGN. In: Advanced Lectures on the Starburst-AGN Connection, Proc., Puebla, Mexico. (eds.) I. Aretxaga, D. Kunth, & R. Mujica, 69.
Grupe, D. (2004). Multiwavelength Studies of AGN. In: Quinn P.J., Górski K.M. (eds) Toward an International Virtual Observatory. ESO ASTROPHYSICS SYMPOSIA. Springer, Berlin, Heidelberg.

Gutcke, T.A., Fanidakis, N., Macciò, A.V. and Lacey, C. (2015). The Star Formation and AGN luminosity relation: Predictions from a semi-analytical model. MNRAS, Vol. 451, pp.3759-3767

Hardcastle, M.J. (1998). Jets, plumes and hot spots in the wide-angle tail source 3C 130. MNRAS, Vol. 298, No. 2, pp. 569-576.

Hardcastle, M.J. (2006). Testing the beamed inverse-Compton model for jet X-ray emission: velocity structure and deceleration. MNRAS, 366, 1465–1474. doi:10.1111/j.1365-2966.2005.09923.x

Hardcastle, M.J. (2008). Hotspots, Jets and Environments. Extragalactic Jets: Theory and Observation from Radio to Gamma Ray. T.A. Rector & D.S. De Young, (eds.), ASP Conference Series, Vol. 386.

Hardcastle, M.J., Kraft, R.P., Sivakoff, G.R., et al. (2007). Astrophys. J., doi:10.1086/524197.

Hardcastle, M.J. and Sakelliou, I. (2004). Jet termination in wide-angle tail radio sources. MNRAS, Vol. 349, No.2, p. 560-575.

Hardcastle, M.J., Sakelliou, I. and Worrall, D.M. (2005). A Chandra and XMM-Newton study of the wide-angle tail radio galaxy 3c 465. MNRAS, 359, 3, p. 1007-1021

Hardcastle, M.J., Kraft, R.P., Sivakoff, G.R., et al. (2007). Astrophys. J., Vol. 670, pp.L81-L84

Hardcastle, M.J., Worrall, D.M., Birkinshaw, M., Laing, R.A. and Bridle, A.H., (2002). MNRAS, 334, 182

Hayakawa, T., Iwamoto, N., Shizuma, T., Kajino, T. and Umeda, H. (2006). Astrophys. J., 648, L47

Heckman, T.M., O'Dea, C.P., Baum, S.A. and Laurikainen, E. (1994). Ap. J., 428, 65.

Hill, G.J. and Lilly, S.J. (1991). Astrophys. J., 367, 1.

Hillas, A.M. (1984). The Origin of Ultra-High-Energy Cosmic Rays. A&A, Vol. 22, pp.425-444

Ho, L.C., Filippenko, A.V. and Sargent, W.L.W. (1997). ApJS, 112, 315.

Högbom, J.A. (1974). Aperture Synthesis with a Non-Regular Distribution of Interferometer Baselines. A&A, Vol. 15, p.417

Holt, J., Tadhunter, C.N. and Morganti, R. (2008). Fast outflows in compact radio sources: evidence for AGN-induced feedback in the early stages of radio source evolution. MNRAS, 387, 639

Hopkins, P.F., Hernquist, L., Cox, T.J., Robertson, B. and Springel, V. (2006). Astrophys. J., Vol.163, pp.50

Jansky, K.G. (1933). Electrical disturbances apparently of extra-terrestrial origin. Proc. Inst. Radio Eng., 21, 1387-98.

Jetha, N.N., Sakelliou, I., Hardcastle, M.J., Ponman, T.J. and Stevens, I.R. (2005). Interactions of Radio Galaxies and the Intra-Cluster Medium in Abell 160 and Abell 2462. MNRAS, 358: 1394-1404.

Kadler, M., Kerp, J., Ros, E., Falcke, H., Pogge, R.W. and Zensus, J.A. (2004). Jet emission in NGC 1052 at radio, optical, and X-ray frequencies, Astro. & Astrophys. 420, 467-474.

Kaufman, M.J., Wolfire, M.G., Hollenbach, D.J. and Luhman, M.L. (1999). Far-Infrared and Submillimeter Emission from Galactic and Extragalactic Photodissociation Regions. Astrophys. J., Vol.527, pp.795-813

Kaviraj, S., Schawinski, K., Silk, J. and Shabala, S.S. (2011). A simple model for AGN feedback in nearby early-type galaxies. MNRAS, 415, 3798–3806. doi:10.1111/j.1365-2966.2011.19002.x

Kellermann, K.I., Sramek, R., Schmidt, M., Shaffer, D.B. and Green, R., (1989). ApJ, 1195.

Kembavi, A.J. and Narlikar, J.V. (1999). Quasars and Active Galactic Nuclei: An introduction. (Cambridge: Cambridge University Press)

Koide, S., Shibata, K., Kudoh, T. et al., (2002). Science, Vol. 295, pp.1688.

Kormendy, J. and Ho, L.C. (2013). Coevolution (Or Not) of Supermassive Black Holes and Host Galaxies. A&A, Vol. 51, pp.511-653

Kraemer, S.B. and Crenshaw, D.M. (2000). Resolved Spectroscopy of the Narrow-Line Region in NGC 1068. III. Physical Conditions in the Emission-Line Gas. Astrophys. J., Vol.544, pp.763-779

Kraft, R.P., et al., (2007). Astrophys. J., Vol. 665, pp.1129

Kukula, M.J., et al. (1996). MNRAS, Vol. 280, pp.1283

Kuligowska, E. (2017). A dynamical model for FR II type radio sources with terminated jet activity. A&A, 598, A93. dio:10.1051/0004-6361/201629033

Kundt, W. (2014). A Uniform Description of All the Astrophysical Jets. Frontier Research in Astrophysics. Proceedings of Science (http://pos.sissa.it/)

Laing, R.A., Riley, J.M. and Longair, M.S. (1983). MNRAS, 204, 151.

Laing, R.A. (1993), in Space telescope Sci. Inst. Symp. 6: Astrophysical Jets, eds. D. Burgarella, M. Livio, & C.P. O'Dea (Cambridge University Press, Cambridge), 95.

Laing, R.A. and Bridle, A.H. (2002b). MNRAS, Vol. 336, pp.1161

Laing, R.A., Canvin, J.R., Cotton, W.D., Bridle, A.H. (2006). MNRAS, Vol. 368, pp.48

Laing, R.A., Bridle, A.H., Parma, P., Feretti, L., Giovannini, G., Murgia, M. and Perley, R.A. (2008). Multifrequency VLA observations of the FR I radio galaxy 3C 31: morphology, spectrum and magnetic field. arXiv:0803.2597. dio:10.1111/j.1365-2966.2008.13091.x

Lannes, A., Anterrieu, E. And Bouyoucef, K. (1994). Fourier interpolation and reconstruction via Shannon-type techniques: I. Regularization principle. Journal of modern optics, 41(8), 1537 -1574.

Lawrence, A. (1987). Classification of active galaxies and the prospect of a unified phenomenology. PASP, 99, 309.

Laing, R.A., Parma, P., de Ruiter, H.R., and Fanti, R. (1999). MNRAS, Vol. 306, pp.513

Lawrence, A. (1999). The AGN/normal galaxy connection: Summary. Advances in Space Research, Elsevier. Vol. 23, pp. 1167-1176.

Leahy, J.P. (1984). 3C 465 - Dynamics of a wide-angle-tail radio source. MNRAS, Vol. 208, p. 323-345.

Leahy, J.P., Black, A.R.S., Dennett-Thorpe, J., Hardcastle, M.J., Komissarov, S., Perley, R.A., Riley J.M. and Scheuer, P.A.G. (1997). MNRAS, 291, 20.

Leahy, P. (1993), in Jets in Extragalactic Radio Sources, ed. H.-J. Roser & K. Meisenheimer (Berlin: Springer), 1.

Lin, Y.-T., Ostriker, J.P. and Miller, C.J. (2010). Astrophys. J., Vol.715, pp.1486.

Liu, R. and Pooley, G.G. (1991). MNRAS, 249, 343.

Lonsdale, C.L. and Barthel, P.D. (1998). The anatomy of a radio source hot spot: Very Large Baseline Array Imaging Of 3C 205. The Astronomical Journal, 115: 895-908.

Marscher, A.P. (2005). The Relationship between Radio and Higher-Frequency Emission in Active Galactic Nuclei. Memorie della Società Astronomica Italiana, Vol.76, p.13

Marquez, I. et al. (2004). A&A, 416, 475.

McCourt, M., Quataert, E., and Parrish, I.J. (2013). MNRAS, Vol. 432, pp.404

McCready, L.L., Pawsey, J.L. and Payne-Scott, R. (1947). Solar radiation at radio frequencies and its relation to sunspots. Proc R Soc (A), Math Phys Sci. 190:357.

Meisenheimer, K., Roser H.-J., Hiltner P.R., et al., (1989). A&A, Vol. 219, pp.63

Middelberg, E. and Bach, U. (2008). High resolution radio astronomy using very long baseline interferometry. RPPh, Vol. 71, 066901. doi:10.1088/0034-4885/71/6/066901.

Miller, J.S. and Antonucci, R.J. (1983). Evidence for a highly polarized continuum in the nucleus of NGC 1068. Astrophys. J., Vol. 271, pp.L7

Miller, J.A., Guessoum, N. and Ramaty, R. (1990). Stochastic Fermi acceleration in solar flares. Astrophys. J., 361, 701.

Morganti, R., Killeen, N.E.B. and Tadhunter, C.N. (1993). MNRAS, 263, 1023.

Morganti, R., Holt, J., Tadhunter, C. and Oosterloo, T. (2010). in IAU Symp. 267, Co-Evolution of Central Black Holes and Galaxies (Cambridge: Cambridge Univ. Press), 429.

Mortlock, D.J., Warren, S.J., Venemans, B.P. et al. (2011). A luminous quasar at a redshift of z = 7.085. Nature, Vol. 474, pp.616-619.

Murgia, M., Parma, P., Mack, K.-H., et al. (2011). Dying radio galaxies in clusters. A&A, 526, A148

Mushotzky, R.F. (1982). The X-ray spectrum and time variability of narrow emission line galaxies. Astrophysical Journal, Vol. 256, pp.92-102.

Muxlow, T.W.B., Richards, A.M.S., Garringtonet, S.T., et al. (2005). High-resolution studies of radio sources in the Hubble Deep and Flanking Fields. MNRAS, 358, 1159.

Nalewajko, K. and Sikora, M. (2008). Reconfinement shocks in relativistic AGN jets. AIP Conference Proceedings; Vol. 1085; Issue 1; doi:10.1063/1.3076713.

Narayan, R. and Yi, I. (1994). Advection-dominated accretion: A self-similar solution. Astrophys. J., Vol. 428, pp.L13-L16 (NY1).

Nelson, C.H., MacKenty, J.W., Simkin, S.M. et al. (1996). Seyfert Galaxies. IV. Nuclear Profiles of Markarian Seyfert Galaxies from Hubble Space Telescope Images. Astrophys. J., V.466, pp.713.

O'Dea, C.P. (2001). Evolution of extragalactic radio sources. EAS Publications Series, Vol. 1, pp.97-107

O'Donoghue, A.A., Eilek, J.A. and Owen, F.N. (1993). Astrophys. J., Vol. 408, pp.428

Offringa, A.R., de Bruyn, A.G., Biehl, M., Zaroubi, S., Bernardi, G. and Pandey, V.N. (2010). Post correlation radio frequency interference classification methods. MNRAS, Vol. 405, pp. 155 -167.

Owen, F.N. and Ledlow, M.J. (1997). A 20 Centimeter VLA Survey of Abell Clusters of Galaxies. VII. Detailed Radio Images. Astrophys. J., 108:41–98.

Panessa, F. and Bassani, L. (2002). A&A, 394, 435.

Parma, P., de Ruiter, H., Mack, K.H., van Breugel, W., Dey, A., Fanti, R., and Klein, U. (1996). A&A, 311, 49.

Parma, P., et al. (1992). in Astrophysical Jets, Poster Papers from the Space Telescope Science Institute Symposium, ed. D. Burgarella, M. Livio, & C. O'Dea (Baltimore, Space Telescope Science Institute), p. 30.

Peck, L.W. and Fenech, D.M. (2013). SERPent: Automated reduction and RFI-mitigation software for e-MERLIN. Elsevier, Astronomy & Computing, 2, 54–66.

Pedelty, J.A., Rudnick, L., McCarthy, P.J. and Spinrad, H. (1989). Astron. J., 97, 647.

Peng, E.W., Côté, P., Jordán, A. et al. (2006). Astrophys. J., Vol. 639, pp.838–857

Perley, R.A., Dreher, J.W., Cowan, J.J. (1984). Astrophs. J., 285, L35.

Perley, R.A., Chandler, C.J., Butler, B.J. and Wrobel, J.M. (2011). The Expanded Very Large Array: A new telescope for new science. Astrophys. J., Vol. 739, pp.L1.

Perez, E., Márquez, I., Marrero, I., et al. (2000). A&A, 353, 893.

Peterson, B.M. (2014). Measuring the Masses of Supermassive Black Holes. Space Sci. Rev. Vol.183, pp 253-275. doi:10.1007/s11214-013-9987-4.

Pinkney, J., Burns, J.O. and Hill, J.M. (1994). Astrophys. J., Vol. 108, pp.2031

Popovic, L.C. (2002). Connection between the X-ray, UV and optical emission line regions of AGNs. Mem. S.A.It. Vol., 1. arXiv:astro-ph/0411011

Pudritz, R., Ouyed, R., Fendt, C., and Brandenburg, A. (2007). in Protostars & Planets V, ed. B. Reipurth, D. Jewitt, & K. Keil (Tuscon: University of Arizona Press), 277.

Qian, S.J., Quirrenbach, A., Witzel, A., Krichbaum, T.P., Hummel, C.A. and Zensus, A. (1991). A&A, 241, 15.

Rees, M.J. (1978). The M87 jet: internal shocks in a plasma beam? MNRAS, Vol. 184, pp.61

Reid, R.I. (2006). Smear fitting: a new image-deconvolution method for interferometric data. MNRAS, Vol. 367, pp.1766-1780.

Rowan-Robinson, M. (1977). On the unity of activity in galaxies. Astrophys. J., Vol.213, pp.635

Saikia, D.J. and Jamrozy, M. (2009). Bulletin of the Astronomical Society of India, 37, 63

Sakelliou, I. and Merrifield, M.R. (1999). The distorted jets and gaseous environment of 3C 465. MNRAS, 305, pp. 417-424.

Sanders, R.H. (1983). The reconfinement of jets. Astrophys. J., Vol. 266, pp.73-81.

Sanders, D.B., Phinney, E.S., Neugebauer, G., Soifer, B.T. and Matthews, K. (1989). Continuum energy distribution of quasars - Shapes and origins. Astrophysical Journal, Vol. 347, p. 29-51.

Schawinski, K., Virani, S., Simmons, B., et al. (2009). Do moderate-luminosity active galactic nuclei suppress star formation? Astrophys. J., 692:L19–L23. doi:10.1088/0004-637X/692/1/L19

Schmidt, M. (1963). 3C 273: a star-like object with large red-shift. Nature, 197(4872), 1040-1040.

Schmidt, M. (1966). Astrophys. J., Vol. 146, pp.7

Schoenmakers, A.P., de Bruyn, A.G., Roettgering, H.J.A. and van der Laan, H. (2000). MNRAS, 315, 395.

Schoenmakers, A.P., de Bruyn, A.G., Rottgering H.J.A. and van der Laan, H. (2001). A&A, Vol.374, pp.861

Seyfert C. (1943). Astrophys. J., 97, 195.

Shibata, K. and Aoki, S. (2003). MHD Jets, Flares, and Gamma Ray Bursts. Astro-ph/0303253

Shklovskii, I.S. (1980). The Nature of the Emission Regions in M87. Sov. Astron. Lett. 6, 107-09.

Shlosman, I., Frank, J. and Begelman, M.C. (1989). Nature, 338, 45.

Shulevski, A., Morganti, R., Barthel, P.D., et al. (2015). The peculiar radio galaxy 4C 35.06: A case for recurrent AGN activity? Astron. & Astrophys., 579, No. A27.

Sikora, M., Begelman, M.C., Madejski, G.M. and Lasota, J.P. (2005). Astrophys. J., 625, 72.

Smith, E.P., Heckman, T.M., Bothun, G.D., Romanishin, W. and Balick, B. (1986). Astrophys. J., 306, 64.

Spruit, H.C. (1996). Evolutionary Processes in Binary Stars (Dordrecht: Kluwer) in NATO/ASI Ser. C 477.

Steenbrugge, K.C. and Blundell, K.M. (2007). Radio and X-ray study of cygnus A. Astrophys. & Space Sci. Vol. 311, p. 323-327.

Stawarz, L. (2004). On the Jet Activity in 3C 273. Astrophys. J., Vol. 613, pp.119-128.

Stone, J.M. (1997). Asymmetric Modes of the Kelvin-Helmholtz Instability in Protostellar Jets. IAU Symposium No. 182, eds. B. Reipurth & C. Bertout. Kluwer Academic Publishers, p. 323-333.

Sun, X., Hoeksema, J.T., Liu, Y., and Zhao, J. (2015). Astrophys. J., 798, 114

Tadhunter, C.N. (2006). The lifecycles of powerful radio galaxies: Triggering and feedback. Astron. Nachr./AN 327, No. 2/3, 180–186. doi:10.1002/asna.200510503.

Tadhunter, C.N. (2008). New Astronomy Reviews, Vol. 52, pp.227

Tadhunter, C.N., Ramos Almeida, C., Morganti, R., Holt, J., Rose, M., Dicken, D. and Inskip, K., (2012). MNRAS, 427, 1603

Taylor, A.R., Young, G., Peracaula, M., Kenney, H.T. and Gregory, P.C. (1996). A&A, 305, 817

Taylor, G.B., Carilli, C.L. and Perley, R.A. (1999). Synthesis Imaging in Radio Astronomy II. ASP Conference Series, Vol. 180.

Terlevich, R., Tenorio-Tagle, G., Franco, J., and Melnick, J. (1992). MNRAS, 255, 713

Thompson, A.R., Moran, J.M. and Swenson, G.W. (2017). Interferometry and Synthesis in Radio Astronomy, Third Edition. Springer, ISBN: 978-3-319-44429-1.

Trimble, V. (2014). Interferometry meets the third and fourth dimensions in galaxies. in IAU Symp. 309 "Galaxie in 3D across the Universe", B.L. Ziegler, F. Combes, H. Dannerbauer & M. Verdugo, Eds. (Cambridge: Cambridge Uni. Press). doi:10.1017/S1743921314009211

Urry, C.M. and Padovani, P. (1995). Unified Schemes for Radio-Loud Active Galactic Nuclei. PASP, Vol. 107, p. 803

Urry, C.M., Padovani, P. and Stickel, M.K. (1991). Astrophys. J., Vol. 382, pp.501

Venkatesan, T.C.A., Batuski, D.J., Hanisch, R.J. and Burns, J.O. (1994). Astrophys. J., V.436, pp.67.

Voit, G.M. and Donahue, M. (2015). Cooling Time, Freefall Time, and Precipitation in the Cores of ACCEPT Galaxy Clusters. Astrophys. J., Vol. 799, pp.L1

Walker R.C., Dhawan V., Romney J.D., Kellermann K.I. and Vermeulen R.C. (2000). Astrophys. J., 530, 233

Wardle, J.F.C., Homan, D.C., Ojha, R. and Roberts, D.H. (1998). Nature, 395, 457.

Weber, R., Faye, C., Biraud, F. and Dansou, J. (1997). Spectral detector for interference time blanking using quantized correlator. A&A, Vol. 126, pp.161

Wiaux, Y., Jacques, L., Puy, G., et al. (2009). Compressed sensing imaging techniques for radio interferometry. MNRAS, Vol. 395, pp.1733-1742.

Wiita, P.J. (2001). Cosmic Radio Jets. arXiv:astro-ph/0103020.

Worrall, D.M., Birkinshaw, M. and Cameron, R.A. (1995). Astrophys. J., Vol. 449, pp.93

Worrall, D.M., Birkinshaw, M. and Hardcastle, M.J. (2001). MNRAS, V. 326, pp.L7-L12

Worrall, D.M., Birkinshaw, M., Kraft, R.P. and Hardcastle, M.J. (2007). ApJL, 658, L79.

Worrall, D.M., Hardcastle, M.J., Pearson, T.J. and Readhead, A.C.S. (2004). MNRAS, Vol. 357, pp.632 644.

Xu, C., Sulentic, J.W., and TuÜs, R. (1999). ApJ, 512, 178.
Zernike, F. (1938). The concept of degree of coherence and its application to optical problems. Physica, Vol. 5, pp.785-795.
Zubovas, K. and King, A. (2016). MNRAS, Vol. 462, pp.4055-4066. doi:10.1093/mnras/stw1845.